

Understanding the development of a reacting fuel jet inside an automotive-size diesel engine using optical and laser-based diagnostics

Author:

Le, Minh Khoi

Publication Date:

2015

DOI:

<https://doi.org/10.26190/unsworks/18587>

License:

<https://creativecommons.org/licenses/by-nc-nd/3.0/au/>

Link to license to see what you are allowed to do with this resource.

Downloaded from <http://hdl.handle.net/1959.4/55272> in <https://unsworks.unsw.edu.au> on 2024-05-06

Understanding the development of a reacting fuel jet inside an automotive-size diesel engine using optical and laser- based diagnostics

Minh Khoi Le

A thesis in fulfilment of the requirements for the degree of

Doctor of Philosophy



UNSW
THE UNIVERSITY OF NEW SOUTH WALES

School of Mechanical and Manufacturing Engineering

The University of New South Wales

August 2015

PLEASE TYPE

THE UNIVERSITY OF NEW SOUTH WALES
Thesis/Dissertation Sheet

Surname or Family name: LE

First name: MINH

Other name/s: KHOI

Abbreviation for degree as given in the University calendar:
Ph.D

School: School of Mechanical and Manufacturing Engineering

Faculty: Faculty of Engineering

Title: Understanding the development of a reacting fuel jet inside an automotive-size diesel engine using optical and laser-based diagnostics

Abstract 350 words maximum: (PLEASE TYPE)

This study aims at improving the understanding of a light-duty, swirl-influenced, wall-interacting diesel flame by experimentally investigating the reacting jet development in a small-bore optical engine. The engine was operated under negative-dwell ignition condition with long injection duration to study jet-wall interactions under high-load conditions. Planar laser-induced fluorescence of hydroxyl (OH-PLIF), fuel-PLIF, and line-of-sight integrated chemiluminescence imaging were performed for various combustion stages as identified by the in-cylinder pressure data and apparent heat release rates. From fuel-PLIF results, swirl flow can be seen to influence the wall-jet penetration such that the penetration of the up-swirl wall-jet is shorter than the down-swirl wall-jet. Chemiluminescence and OH-PLIF images then indicates that both low and high-temperature reactions originate from the wall-jet head region where the initial turbulent ring-vortex is formed from jet-wall interactions, suggesting that locally enhanced mixing induces the ignitions. The swirl flow also impacts the mixing process and the strain rate of the wall-jet mixture, leading to earlier, faster and stronger high-temperature reaction on the down-swirl side. This is largely different to the flame base found in the free jet region in heavy-duty, large-bore engines. Investigation with variations in injection pressure confirms the original ignition-zone locations, with stronger reactions being observed at higher injection pressure. However, the impact of the swirl flow has begun to be negated by the high injection momentum such that the high temperature reaction in the down-swirl and up-swirl side are comparable. Flame luminosity and planar laser-induced incandescence of soot was also obtained with the use of surrogate fuel methyl-decanoate for improved diagnostic quality in an investigation of soot emission. Soot is shown to first form in the rich area near the wall impingement point and then flow along the bowl wall in both up-swirl and down-swirl directions. These soot pockets are surrounded by OH and disappear altogether at following crank angles, suggesting the oxidation of soot due to OH-attack. Later on, some soot pockets then flow to the bowl centre due to the downward movement of the piston and can persist if there are no active OH radicals.

Declaration relating to disposition of project thesis/dissertation

I hereby grant to the University of New South Wales or its agents the right to archive and to make available my thesis or dissertation in whole or in part in the University libraries in all forms of media, now or here after known, subject to the provisions of the Copyright Act 1968. I retain all property rights, such as patent rights. I also retain the right to use in future works (such as articles or books) all or part of this thesis or dissertation.

I also authorise University Microfilms to use the 350 word abstract of my thesis in Dissertation Abstracts International (this is applicable to doctoral theses only).

Signature

Witness

04/12/2015

Date

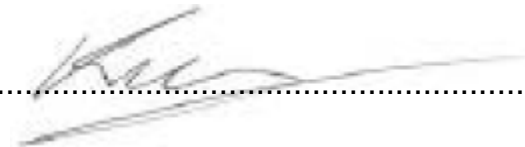
The University recognises that there may be exceptional circumstances requiring restrictions on copying or conditions on use. Requests for restriction for a period of up to 2 years must be made in writing. Requests for a longer period of restriction may be considered in exceptional circumstances and require the approval of the Dean of Graduate Research.

FOR OFFICE USE ONLY

Date of completion of requirements for Award:

COPYRIGHT STATEMENT

'I hereby grant the University of New South Wales or its agents the right to archive and to make available my thesis or dissertation in whole or part in the University libraries in all forms of media, now or here after known, subject to the provisions of the Copyright Act 1968. I retain all proprietary rights, such as patent rights. I also retain the right to use in future works (such as articles or books) all or part of this thesis or dissertation. I also authorise University Microfilms to use the 350 word abstract of my thesis in Dissertation Abstract International (this is applicable to doctoral theses only). I have either used no substantial portions of copyright material in my thesis or I have obtained permission to use copyright material; where permission has not been granted I have applied/will apply for a partial restriction of the digital copy of my thesis or dissertation.'

Signed..........

Date04/12/2015.....

AUTHENTICITY STATEMENT

'I certify that the Library deposit digital copy is a direct equivalent of the final officially approved version of my thesis. No emendation of content has occurred and if there are any minor variations in formatting, they are the result of the conversion to digital format.'

Signed..........

Date04/12/2015.....

ORIGINALITY STATEMENT

‘I hereby declare that this submission is my own work and to the best of my knowledge it contains no materials previously published or written by another person, or substantial proportions of material which have been accepted for the award of any other degree or diploma at UNSW or any other educational institution, except where due acknowledgement is made in the thesis. Any contribution made to the research by others, with whom I have worked at UNSW or elsewhere, is explicitly acknowledged in the thesis. I also declare that the intellectual content of this thesis is the product of my own work, except to the extent that assistance from others in the project's design and conception or in style, presentation and linguistic expression is acknowledged.’

Signed.....

Date04/12/2015.....

Acknowledgement

The completion of this thesis would not be possible without the support and inspirations from many individuals and organisations. To each and everyone of them, I would like to express my most sincere appreciation and gratitude. The journey toward finishing the Ph.D degree at the University of New South Wales has been tough, yet incredibly rewarding. Without a doubt, the skills and experiences that I have gained along the way will contribute greatly to my future career as well as my private life.

First of all, I would like to thank my parents, Dr. Van So Le and Phuc Hien Do, who were the ones that convinced me to pursue this degree. They have not only provided great emotional support, but also allowed me to eat, work and sleep in a great environment during my time as a PhD candidate. Thank you for supporting me and for feeding me with all the delicious food and helpful advices.

Second, I would like to give a very important mention to my supervisor and co-supervisor, Dr. Sanghoon Kook and Dr. Qing Nan Chan for their continuous support and invaluable professional guidance throughout this journey. In particular, with his extensive technical knowledge, his vast experience, strong beliefs and decision-making skills, Dr. Kook has helped me tremendously and inspired me to continue pushing myself to improve my capability and quality of work. He is a great role model for anyone who wants to be successful in their professional career. And for Dr. Chan, I would have made a lot more mistakes and destroyed more equipments if not for your expertise in laser diagnostics.

A special mention also goes out to my sisters and their families, whose strength, and determination in dealing with hardships have taught me the importance and power of resiliency. Especially to my sister who is overcoming the most dire of circumstances, you make me believe anything is possible.

To my beloved colleagues, Dr. Srinivas Padala, Dr. Alvin Rusly, Dr. Renlin Zhang, Bryan Changwan Woo, Shyam Pasunurthi, our time together, our thoughtful (and sometimes

immature) discussions, and the share of knowledge, ideas and experience have motivated and encouraged me greatly in keeping up with my work and progress. To our new research students and PhD candidates, Lewis Clark, Yilong Zhang, Monica Chi, I assured you had made the right choice if you were looking to pursue research with one of the best engine research group in the world; I wished you all the best with your work.

Last but not least, I would like to thank all the responsible organisations that have provided the fund for this project.

Table of Contents

| | |
|--|------------|
| ABSTRACT | i |
| LIST OF PUBLICATIONS..... | iv |
| LIST OF TABLES | vi |
| LIST OF FIGURES | vii |
| NOMENCLATURES..... | xiv |
| CHAPTER 1. INTRODUCTION..... | 1 |
| 1.1. AIMS AND OBJECTIVES | 2 |
| CHAPTER 2. LITERATURE REVIEW..... | 4 |
| 2.1. DIESEL COMBUSTION MODELS | 4 |
| 2.2. IMPACT OF JET-WALL INTERACTION AND SWIRL FLOW..... | 5 |
| 2.3. EFFECT OF INJECTION PRESSURE ON THE JET DEVELOPMENT..... | 7 |
| 2.4. SOOT PROCESSES INSIDE DIESEL ENGINES | 8 |
| 2.5. OPTICAL/LASER DIAGNOSTICS | 9 |
| 2.5.1. <i>Cool-flame chemiluminescence</i> | 9 |
| 2.5.2. <i>Excited hydroxyl (OH*) chemiluminescence</i> | 9 |
| 2.5.3. <i>Hydroxyl planar laser induced fluorescence (OH-PLIF)</i> | 10 |
| 2.5.4. <i>Fuel planar laser-induced fluorescence (Fuel-PLIF)</i> | 14 |
| 2.5.5. <i>Soot planar laser induced incandescence (Soot-PLII)</i> | 14 |
| CHAPTER 3. METHODOLOGY AND APPARATUS..... | 16 |
| 3.1. EXPERIMENTAL APPARATUS | 16 |
| 3.1.1. <i>Optical compression-ignition engine</i> | 17 |
| 3.1.2. <i>Piston designs</i> | 20 |
| 3.1.3. <i>Fuel injection control system</i> | 23 |

| | | |
|------------------------------|---|-----------|
| 3.1.4. | <i>Laser system</i> | 24 |
| 3.1.5. | <i>Sheet-making optics</i> | 26 |
| CHAPTER 4. | DATA CAPTURING AND PROCESSING | 30 |
| 4.1. | IN-CYLINDER PRESSURE AND APPARENT HEAT RELEASE RATE | 30 |
| 4.2. | IMAGING APPARATUS..... | 30 |
| 4.2.1. | <i>Intensified charged-coupled device camera (ICCD)</i> | 31 |
| 4.2.2. | <i>Optical filters</i> | 31 |
| 4.2.3. | <i>Capturing synchronisations</i> | 35 |
| 4.2.4. | <i>Capturing parameters</i> | 36 |
| 4.3. | IMAGE PROCESSING AND PRESENTATION | 36 |
| 4.4. | CYCLIC VARIATIONS | 38 |
| 4.4.1. | <i>Variations in in-cylinder pressure data</i> | 38 |
| 4.4.2. | <i>Cyclic variations in images</i> | 39 |
| CHAPTER 5. | DEVELOPMENT OF A WALL-INTERACTING DIESEL JET | 45 |
| 5.1. | EXPERIMENTAL APPROACH..... | 45 |
| 5.1.1. | <i>Laser planes for planar laser diagnostics and nozzle selection</i> | 46 |
| 5.1.2. | <i>Online vs. offline OH-PLIF presentation</i> | 47 |
| 5.2. | IN-CYLINDER PRESSURE AND APPARENT HEAT RELEASE RATE | 49 |
| 5.3. | COMBUSTION STAGE A: LIQUID/VAPOUR PENETRATION | 50 |
| 5.4. | COMBUSTION STAGE C: LOW-TEMPERATURE REACTION | 52 |
| 5.5. | COMBUSTION STAGE C: HIGH-TEMPERATURE REACTION | 55 |
| 5.6. | SUMMARY | 61 |
| CHAPTER 6. | THE EFFECT OF INJECTION PRESSURE ON THE WALL | |
| INTERACTING JET | | 62 |
| 6.1. | EXPERIMENTAL APPROACH..... | 62 |
| 6.2. | VARIATIONS IN IN-CYLINDER PRESSURE AND APPARENT HEAT RELEASE RATE | 63 |
| 6.3. | FUEL JET PENETRATION AT HIGHER INJECTION PRESSURES | 65 |
| 6.4. | LOW-TEMPERATURE REACTION FOR VARIOUS INJECTION PRESSURES | 67 |
| 6.5. | HIGH-TEMPERATURE REACTION AT VARIOUS INJECTION PRESSURES | 70 |

| | | |
|-------------------|---|------------|
| 6.6. | SUMMARY | 76 |
| CHAPTER 7. | SOOT PROCESSES | 78 |
| 7.1. | CURVED PISTON BOWL – PISTON B | 79 |
| 7.2. | METHYL DECANOATE – LOW SOOTING SURROGATE FUEL | 82 |
| 7.3. | COMBINED PLII AND OH-PLIF IMAGES | 87 |
| 7.4. | CYCLIC VARIATIONS OF PLII IMAGES | 88 |
| 7.5. | IN-CYLINDER PRESSURE AND APPARENT HEAT RELEASE RATE | 90 |
| 7.6. | IGNITION DELAY PERIOD | 92 |
| 7.7. | PREMIXED BURN PHASE | 94 |
| 7.8. | MIXING-CONTROLLED BURN PHASE..... | 96 |
| 7.9. | SUMMARY | 101 |
| CHAPTER 8. | CONCLUSION..... | 103 |
| | FUTURE WORK | 107 |
| | REFERENCES..... | 108 |

Abstract

The fuel penetration and reacting diesel jet development have been studied in a small-bore optical engine to improve the understanding of a swirl-influenced, wall-interacting diesel flame. The optical access to the engine combustion chamber was made possible via multiple quartz windows positioned in a cylindrical piston bowl and cylinder liner. Using the common-rail fuel injection system of the engine, the fuel injection was executed for long duration, creating negative ignition dwell conditions in which the start of combustion occurs before the end of injection. A single-hole nozzle was used to isolate the jet-wall interaction from jet-jet interactions while limiting the in-cylinder pressure below the burst-pressure of quartz windows. Planar laser-induced fluorescence imaging of hydroxyl (OH-PLIF), fuel-PLIF, and line-of-sight integrated chemiluminescence imaging were performed for various combustion stages identified by the in-cylinder pressure traces and apparent heat release rates. These include stages of vaporising fuel penetration, low-temperature reaction, and high-temperature reaction. The fuel-PLIF images show that the fuel penetration was strongly influenced by a swirl flow with the wall-jet penetration on the up-swirl side being shorter than that of the down-swirl jet. During the low-temperature reaction, cool flame chemiluminescence appears in the wall-jet head region. Interestingly, this region is where a turbulent ring-vortex is formed due to jet-wall interactions, suggesting that locally enhanced mixing induced the first-stage ignition. The OH-PLIF images show that the second-stage, high-temperature reaction starts to occur and then expand drastically in the same wall-jet head region. Since the reaction occurs in the wall-jet region, the swirl flow impacts the high-temperature reaction significantly, as evidenced by more intense OH signals in the down-swirl jet. This is due to the influence of the swirl flow on the mixing process, leading to relatively richer mixtures on the down-swirl side. Upon the end of fuel injection, the heat release rate declines and the OH-PLIF signals slowly diminish.

How the variation in injection pressure influences the combustion processes of a wall-interacting diesel jet has also been investigated. The cool-flame images together with the

apparent heat release rate suggest that the low-temperature reaction still emerges from the wall-interacting jet head region but it becomes stronger with increasing injection pressure due to the better air-fuel mixing at the enhanced turbulent ring-vortex. The influence of in-cylinder swirl flow on the OH* chemiluminescence signals was again observed such that the high-temperature reaction in the down-swirl side of the jet occurs earlier than that in the up-swirl side of the jet regardless of the injection pressure. Moreover, the second-stage ignition on the down-swirl side of the jet is also found to be stronger than the up-swirl side of the jet initially. However, as the injection pressure increases and the high temperature reaction matures, the spread and magnitude of the up-swirl OH* chemiluminescence signals become comparable to the down-swirl signals owing to the increased injection momentum overcoming the swirl flow. The OH-PLIF signals indicate that the high-temperature reaction zone continues to grow in the turbulent ring-vortex region where the cool-flame signals were detected at earlier timings. The expansion of wall-jet head OH signals shows an interestingly growing trend with increasing injection pressure, which can be explained by a stronger ring-vortex due to the increased injection momentum.

At selected operating conditions of 100 MPa common-rail pressure and long 2.04-ms injection duration, planar laser-induced incandescence (PLII) imaging has been performed to clarify soot processes within the wall-interacting jet. Once again, a single-hole nozzle was used to isolate the jet-wall interaction from jet-jet interactions and to apply long injection duration corresponding to high-load engine operating conditions in which soot formation is particularly problematic. Compared to the previous experiments, two major changes were made in fuel and piston design. As opposed to a conventional diesel fuel used in the previous experiments, the soot diagnostics were conducted using methyl decanoate, a surrogate fuel with low-sooting propensity, to reduce laser attenuation. In addition, the piston bowl design was modified to include a curved bowl wall to enhance the fuel jet penetration back towards the nozzle, which is closer to the conditions in most production engines. Laser-based images show that the fuel

impinges on the bowl wall soon after the start of injection and then bounces off along the wall forming a wall-interacting jet. The fuel jet continues to travel along the bowl wall as well as the bottom surface of the piston bowl. Although the latter motion was not significant in the previous experiments, with the new curved bowl-wall, the fuel penetration back towards the nozzle was clearly observed. During the premixed burn phase of diesel combustion, the high-temperature reaction starts to occur at the leading edge of the penetrating jet back towards the nozzle, initially near the jet axis and then spreads in the radial direction. During the mixing-controlled burn phase, the high-temperature reaction zone fills up the entire combustion chamber and the soot formation starts to occur in the rich area near the wall impingement point. The soot then flows along the bowl wall in both up-swirl and down-swirl directions. Throughout this phase, these soot pockets are surrounded by OH, which disappear altogether at subsequent crank angle locations suggesting the soot oxidation by OH radicals. However, some soot pockets are transported into the centre of bowl due to the downward movement of the piston and persist for long as there are no active OH radicals.

To conclude, these major findings made on the temporal and spatial evolution of a wall-interacting diesel jet, its variations with increasing injection pressure, and the soot concentration within the jet are summarised by illustrating regions of fuel, low- and high-temperature reaction, as well as soots for various crank angle locations during a firing cycle of the engine.

List of publications

Journals Publications

- Le, M. K., Kook, S., & Hawkes, E. R. (2015). The planar imaging of laser induced fluorescence of fuel and hydroxyl for a wall-interacting jet in a single-cylinder, automotive-size, optically accessible diesel engine. *Fuel*, 140, 143-155. doi:[10.1016/j.fuel.2014.09.089](https://doi.org/10.1016/j.fuel.2014.09.089) (**Chapter 5**)
- Le, M. K., & Kook, S. (2015). Injection Pressure Effects on the Flame Development in a Light-Duty Optical Diesel Engine. *SAE International Journal of Engines*, 8(2), 609-624. doi:[10.4271/2015-01-0791](https://doi.org/10.4271/2015-01-0791) (**Chapter 6**)
- Le, M.K., Zhang, R., Rao, L., Kook, S., & Hawkes, E.R. (2015) The development of hydroxyl and soot in a methyl decanoate-fuelled automotive-size optical diesel engine. *Submitted to Fuel 2015, Manuscript reference number: JFUE-D-15-01752* (**Chapter 7**)
- Rusly, A. M., Le, M. K., Kook, S., & Hawkes, E. R. (2014). The shortening of lift-off length associated with jet-wall and jet-jet interaction in a small-bore optical diesel engine. *Fuel*, 125, 1-14. doi:[10.1016/j.fuel.2014.02.004](https://doi.org/10.1016/j.fuel.2014.02.004)
- Rusly, A., Le, M. K., & Kook, S. (2013). Effect of Injection Pressure on Transient Behaviour of Wall-Interacting Jet Flame Base in an Automotive-Size Diesel Engine. *SAE International Journal of Fuels and Lubricants*, 6(3), 615-626. doi:[10.4271/2013-01-2536](https://doi.org/10.4271/2013-01-2536)

Conference proceedings

- Le, M. K., Kook, S., Chan, Q. N., & Hawkes, E. R. (2014). Comparison between OH* chemiluminescence and OH planar laser-induced fluorescence images in a light-duty optical diesel engine. In *19th Australasian Fluid Mechanics Conference* (pp. Paper No 434). Melbourne, Australia

- Le, M. K., Kook, S., & Hawkes, E. R. (2013). Measurement of Diesel Jet Tip Penetration in an Automotive-Size Optical Engine using Planar Laser-Induced Fluorescence of Fuel. In D. Zhang (Ed.), *Proceedings of the 2013 Australian Combustion Symposium* (pp. Paper no 19). Perth, Western Australia.

List of tables

| | |
|---|----|
| Table 2.1 Avantages and disadvantages of different OH-PLIF excitation schemes | 11 |
| Table 3.1 Engine specifications and operating conditions..... | 19 |
| Table 3.2 Fuel injection conditions..... | 24 |
| Table 3.3 Laser wavelengths and corresponding power level of the laser-based diagnostic techniques | 26 |
| Table 3.4 Lens combinations for the laser-sheet making optics | 28 |
| Table 4.1 ICCD camera capturing parameters used for each optical diagnostic techniques | 36 |
| Table 4.2 Pseudo-colouring for the images from each optical diagnostics..... | 38 |
| Table 7.1 Alternative fuels used in diesel combustion researches..... | 84 |
| Table 7.2 Properties of Methyl-decanoate and conventional diesel | 85 |

List of figures

| | |
|--|----|
| Figure 2.1 Dec’s conceptual model for conventional diesel combustion during quasi-steady period in the jet development. (Reprinted from Ref. [4]) | 5 |
| Figure 2.2 Wall-interating jet in a combustion chamber. (Reprinted from Ref. [20]) | 6 |
| Figure 2.3 OH-PLIF emissions from 284 nm excitation – simulated by LIFBASE | 12 |
| Figure 2.4 Reproduced from Ref [85]: Emission spectra of LII signals from an ethylene/air burner with 1064 nm excitation, 50 ns detection gate for 67 MW/cm ² (a) and 10 ns detection gate for 153 MW/cm ² laser-pulse power (b). | 15 |
| Figure 3.1 Exploded view of the light-duty optical engine..... | 17 |
| Figure 3.2 Illustrated schematics of the optical diesel engine and the image capturing setup.... | 18 |
| Figure 3.3 Piston A design..... | 21 |
| Figure 3.4 Piston B design | 22 |
| Figure 3.5 Plano-concave and plano-convex illustration. (reproduced from Ref [92]) | 26 |
| Figure 3.6 Mock-up test and result for the laser sheet coverage of the combustion chamber (top) and the schematics for the sheet making optics setup and optical path for planar laser-based diagnostic (bottom) In this study, the lenses used are: 500 mm EFL plano-convex, -12.7 mm EFL plano-concave, 150 mm EFL plano-convex and -25.4 mm EFL plano-concave, in order of position with respect to beam path. | 27 |
| Figure 4.1 Transmittance data for the WG305 glass filter from Schott filter (top) and 300 nm band pass filter from Semrock filter (bottom)..... | 33 |
| Figure 4.2 Transmittance data for the 430 nm band-pass filter from Andover Corporation (top), and 450 nm short-pass filter from Edmund Optics (bottom) | 34 |
| Figure 4.3 Timing diagram for the synchronisation of the engine, laser system and camera for laser-based diagnostics. Laser timing can be disregarded for chemiluminescence imaging | 35 |

| | |
|--|----|
| Figure 4.4 An example image from fuel-PLIF taken at TDC with Piston A at fixed operating condition and 130 MPa injection pressure..... | 37 |
| Figure 4.5 In-cylinder pressure traces of 20 instantaneous cycles (black lines) and their ensemble average (red line) at the 130-MPa injection pressure condition. Their corresponding apparent heat release rates are also shown at the bottom..... | 39 |
| Figure 4.6 Individual “online” OH-PLIF images of all engine cycles captured at 10°CA aTDC at the 130-MPa injection pressure. The averaged image and selected individual image are shown at the top right..... | 40 |
| Figure 4.7 The correlation factors (top) and the area coverage of PLIF signal (middle) for all individual images captured at 13.5°CA aTDC and 70 MPa injection pressure. Both online and offline images taken at 7 mm from the cylinder head are analysed. Shown at the bottom are a selected individual image for the highest correlation factor and the average of 20 images..... | 42 |
| Figure 4.8. a) Individual OH* chemiluminescence images of 19 selected cycles captured at 10°CA aTDC at the 130-MPa injection pressure condition. Shown at the top right are the ensemble averaged image and the selected image. b)Individual cool-flame chemiluminescence images of 19 selected engine cycles captured at 5°CA aTDC at the 130-MPa injection pressure condition. The ensemble averaged image and the selected image are shown at the top right. | 44 |
| Figure 5.1 The laser beam path and area coverage (top), the field of view of PLIF imaging in r- θ plane (bottom-left), and illustration of the laser sheets for various distances from the cylinder head as well as the nominal spray axis and piston-bowl geometry in r-z plane (bottom-right)..... | 46 |
| Figure 5.2 Post-processing of an offline OH-PLIF image for boundary detection (left) and the offline boundaries overlaid on the online OH-PLIF image (right) taken at the same 13.5°CA aTDC..... | 47 |

Figure 5.3 Average in-cylinder pressure trace for motoring (black dot line) and firing (brown solid line) cycles shown at the top and the apparent heat release rate (aHRR) trace at the bottom. Also shown is the measured fuel injection rate (blue solid line). To illustrate, symbols are provided on the pressure and aHRR traces for each image time for three combustion stages of this study, including liquid/vapour penetration (A: circles), low-temperature reaction (B: squares), high-temperature reaction I (C: triangles and diamonds). 48

Figure 5.4 PLIF images of fuel fluorescence during combustion stage A: liquid/vapour penetration. Only online images are shown for the plane at 7 mm below the cylinder head due to non-reacting conditions (left). Shown on the top-right corner illustrates the estimation of the wall-jet tip penetration length. The results are shown in the bottom-right for both up-swirl and down-swirl sides of the diesel jet. 50

Figure 5.5 Cool flame chemiluminescence images (left), offline OH-PLIF images (middle) and online OH-PLIF images (right) during combustion stage B: low-temperature reaction. The PLIF images were taken at 7 mm below the cylinder head. The boundaries of offline images are overlaid on the online images for comparison purposes. 54

Figure 5.6 OH* chemiluminescence images (left), offline OH-PLIF images (middle) and online OH-PLIF images (right) during combustion stage C: high-temperature reaction between 9.5 and 13.5°CA aTDC when the apparent heat release rate increases. The PLIF images were taken at 7 mm below the cylinder head. The boundaries of offline images are overlaid on the online images for comparison purposes. The red arrows shown on the online images at 12.5 and 13.5°CA are to annotate the expansion of OH signals behind the jet head. EoI denotes the end of injection..... 57

Figure 5.7 Online OH-PLIF images during combustion stage C: high-temperature reaction between 9.5 and 13.5°CA aTDC when the apparent heat release rate increases. The planar images are presented at various distances from the cylinder head. Shown at

the bottom are line-of-sight integrated OH* chemiluminescence images (from Fig. 10). The red arrows point out the expansion of OH signals in the jet head region... 59

Figure 5.8 Online OH-PLIF images during combustion stage C: high-temperature reaction between 14 and 19 °CA aTDC when the apparatne heat release rate decreases. The planar images are shown at 7 and 10 mm below the cylinder head. 60

Figure 6.1 Laser attenuation issue at higher injection pressure 63

Figure 6.2 Average in-cylinder pressure traces (top) and apparent heat release rates (bottom) for various injection pressures. Also shown at the bottom is the injection rate profiles measured using a Bosch-tube-type injection rate meter. 64

Figure 6.3 Example fuel-PLIF images at 7mm below the cylinder head for the 130-MPa injection pressure condition and the illustration of the penetration length measurement (top). Shown at the bottom are the jet tip penetration lengths on the up-swirl side (left) and down-swirl side (right) of the jet for various injection pressures. 66

Figure 6.4 Natural “cool-flame” chemiluminescence images during the low-temperature reaction period for various injection pressures. A jet axis is drawn in each figure to denote the continuing fuel injection..... 67

Figure 6.5 Offline OH-PLIF boundaries overlaid on online OH-PLIF images during the low-temperature reaction period for various injection pressures. The planar images were obtained at 7 mm below the cylinder head. Similar to Figure 10, a jet axis is drawn on each image to denote the continuing fuel injection..... 69

Figure 6.6 OH* chemiluminescence images during the high-temperature reaction period for various injection pressures. A jet axis is drawn jet in some images to denote the continuing fuel injection. The swirl flow rotates in the clock-wise direction as illustrated at the top images. The red arrows point out the expansion of OH* zones occurring in the wall-jet head region. As annotated, the images corresponding to the

| | |
|---|----|
| peak apparent heat release rate are 13, 11, and 10°CA aTDC for 70, 100, and 130 MPa injection pressure conditions, respectively..... | 72 |
| Figure 6.7 Offline OH-PLIF boundaries overlaid on online OH-PLIF images during the high-temperature reaction period as of Figure 12 for various injection pressures. The planar images were obtained at 7 mm below the cylinder head. The red arrows indicate the expansion of OH-PLIF signals occurring in the wall-jet head region. As annotated, the images corresponding to the peak apparent heat release rate are 13, 11, and 10°CA aTDC for 70, 100, and 130 MPa injection pressure conditions, respectively. | 73 |
| Figure 6.8 The OH-PLIF images taken at 5, 7 and 10 mm below the cylinder head at around the peak aHRR timing for various injection pressures. The 7-mm images are repeated from Figure 13 for comparison purposes..... | 75 |
| Figure 7.1 Still images from high-speed movies of natural diesel combustion luminosity for a selected cycle of piston type A (top) and piston type B (bottom)..... | 79 |
| Figure 7.2 Illustration of the laser sheet with respect to the piston bowl and fuel jet in the bottom view (top) and side view (bottom-left). Also shown on the bottom-right corner is an example image of laser-induced fuel fluorescence obtained at 7 mm below the cylinder head..... | 81 |
| Figure 7.3 . Line-of-sight integrated soot luminosity (top row) and soot planar laser-induced incandescence (PLII) images at 7, 9 and 11 mm (bottom) from conventional diesel during the sooting period at 13°, 15° and 17.5°CA aTDC. Yellow arrows highlight the area where signal were lost due to attenuation..... | 82 |
| Figure 7.4 Line-of-sight integrated soot luminosity (top row) and soot planar laser-induced incandescence (PLII) images at 7, 9 and 11 mm (bottom) from Methyl-decanoate (MD) during the sooting period at 13°, 15° and 17.5°CA aTDC..... | 84 |
| Figure 7.5 Still images from high-speed movies of hot soot luminosity for a selected cycle of diesel (top) and methyl decanoate fuel (bottom)..... | 86 |

Figure 7.6 (a) Offline OH-PLIF (top-left) and online OH-PLIF signals (top-right) pseudo-coloured in yellow and blue, respectively, and their combined image (bottom) and (b) Soot-PLII (top-left) and OH-PLIF signals (top-right) pseudo-coloured in red and blue, respectively, and their combined image (bottom). On the combined images, the corresponding imaging times are denoted in crank angle degrees after top dead centre ($^{\circ}$ aTDC) and after the start of fuel injection ($^{\circ}$ aSOI). All images were obtained 7 mm below the cylinder head. 87

Figure 7.7 In-cylinder pressure traces of 20 instantaneous cycles and their ensemble average (top). Shown at the bottom are the corresponding traces of apparent heat release rate. 88

Figure 7.8 Individual soot-PLII images of 20 engine cycles at 12° CA aTDC. The representative PLII image of the 20-image set is shown at the top-right. All images were taken at 7 mm below the cylinder head. 89

Figure 7.9 Averaged in-cylinder pressure (top) and the apparent heat release rate (aHRR) traces (bottom) for the selected engine operating conditions. The traces for conventional diesel are orange coloured and MD's blue. Also shown in the aHRR plot is the measured injection rate profile for both fuels. The laser-based imaging times are illustrated on both in-cylinder pressure and aHRR traces using (A) circles/squares for the ignition delay phase, (B) triangles for the premixed combustion phase, and (C) diamonds for the mixing-controlled combustion phase. 90

Figure 7.10 Planar laser induced fluorescence (PLIF) signals and cool-flame chemiluminescence signals during the ignition delay period. Shown on the first two rows is the development of a non-reacting fuel jet during jet-wall interaction. Also shown on the bottom row are the cool-flame signals corresponding to the images on the middle row. Illustrations at the right show the used laser sheet position (7 mm below the cylinder head) with respect to the piston position at a given crank angle location and the postulated fuel jet development. 92

| | |
|---|-----|
| Figure 7.11 OH* chemiluminescence images (top) and corresponding planar laser induced fluorescence (PLIF) signals of OH (online/offline combined) at 7 mm (middle) and 9 mm (bottom) below the cylinder head during the premixed burn phase. The vertical dashed-dot line indicates the fuel jet trajectory. Illustration to the right shows the used laser sheet position with respect to the piston position at a given crank angle and the postulated fuel jet development..... | 95 |
| Figure 7.12 Planar laser induced fluorescence (PLIF) signals of OH (online/offline combined, top), planar laser-induced incandescence (PLII, middle) of soot, and the combined image (bottom) during the mixing-controlled burn phase. The vertical dashed-dot line indicates the fuel jet trajectory. Illustration at the right shows the used laser sheet position (7 mm below the cylinder head) with respect to the piston position at a given crank angle location and the postulated fuel jet development | 97 |
| Figure 7.13 The combined images of OH-PLIF signals (online/offline combined) and PLII signals during the mixing-controlled combustion phase. The images were taken at 7, 9, and 11 mm below the cylinder head. Illustration on the right shows the used laser sheet positions with respect to the piston position at a given crank angle location and the postulated fuel jet development. | 99 |
| Figure 8.1 Illustration of the influence of injection pressure on the development of a wall-interacting diesel jet in a small-bore diesel engine. The images are arranged in an increasing temporal order from left to right..... | 104 |
| Figure 8.2 Illustration of the development of fuel, low-temperature and high-temperature reactions, and soot of a single fuel jet in a small-bore diesel engine | 105 |

Nomenclature

aHRR – apparent heat release rate

aEOI – after end of injection

aSOI – after start of injection

aTDC – after top dead centre

bTDC – before top dead centre

FWHM – full width half modulus

HMN – hepta methyl nonane

ICCD – intensified charge-coupled device

KHP - ketohydroperoxide

LTC – Low temperature combustion

MD – methyl decanoate

PCCI – premixed charge compression ignition

PLIF – planar laser-induced fluorescence

PLII – planar laser-induced incandescence

TDC – top dead centre

TEOP – tetra-eth-oxy-propane

UV – Ultra violet

Chapter 1.

Introduction

The internal combustion engine has been the main driving force in propelling society into its current modern state. Its impact is widespread, from applications in large-scale industries such as mining, energy or manufacturing to smaller machines and equipments for the consumers market. In particular, the internal combustion engine has truly revolutionised the way we travel and transport goods. Never has it been this easy, affordable, and convenient to travel across cities, countries and continents. Since the introduction of the first automobile concept equipped with internal combustion engine in 1886, constant effort has been made in research and development to create more powerful and robust engines. In more recent times, shortage in fossil fuels together with the negative impact of undesirable emission gases on human health have shifted the focus of engine research and development toward the reduction of pollutants and improvement in efficiency and fuel economy.

Compression-ignition engine (diesel engine) has been widely used in both on-road and off-road vehicles and machineries, especially for heavy-duty applications. This is mainly due to its higher specific torque output and efficiency comparing to the spark ignition engine. Light-duty diesel engine has also been utilised extensively: it is the dominant powertrain in commercial vehicles evidenced by 97% market share in Europe while diesel-powered passenger vehicles are

also becoming popular, dominating the European and Indian market with more than 50% share as well as showing a rapid growth in Australia and Korea as of 2013 [1, 2]. With the lower green-house gases and fuel economy limit to be implemented in 2020 in major markets such as the US and Europe, the higher efficiency of light-duty diesel engines will continue to give them the advantage over gasoline spark-ignition engines in meeting these regulations [3]. Due to the growth in the use of passenger diesel vehicles and their important role in meeting future regulations, there is a clear demand for an improved understanding of combustion processes inside a light-duty diesel engine.

The engine size (or displacement volume) which is normally determined based on the brake power needed for a given vehicle weight, has a significant impact on the formation of air-fuel mixture and the flowfield inside the cylinder. With smaller and more compact combustion chamber geometry, the jet-wall interaction can become more significant as the fuel jet impinges on the wall at earlier timing relative to its combustion phasing. Moreover, smaller engines are typically designed for high-speed operations and thus higher swirl ratio design is implemented, further complicating the in-cylinder processes. While great efforts have been made on studying combustion processes inside the cylinder of large-bore, heavy-duty diesel engines, the aforementioned differences in combustion processes caused by a smaller combustion chamber present a necessity to further investigations focusing on small-bore, light-duty diesel engines, which is the motive for doing this study.

1.1. *Aims and Objectives*

This study aims to provide an improved understanding of the development of a reacting diesel jet inside a small-bore light-duty diesel engine. The focus is on visualising the evolution of a swirl-influenced, wall-interaction diesel jet during the main combustion event. Variations in the injection pressure were explored to clarify the wall jet development at various injection momentum conditions. Furthermore, the visualisation of soot, a strictly regulated emission, was

also performed to provide an improved understanding of how soot formation and oxidation occurs during diesel combustion in a small-bore engine. To this end, laser-based imaging diagnostics including planar laser-induced fluorescence of hydroxyls (OH-PLIF), fuel-PLIF, and planar laser-induced incandescence of soot (Soot-PLII) were executed in an optically accessible common-rail diesel engine. Line-of-sight integrated imaging such as OH* and cool flame chemiluminescence as well as natural flame luminosity were also performed to provide complementary information to the laser-based images. The ultimate goal is to re-develop a conceptual model that is directly relevant to small-bore diesel engine combustion involving significant jet-wall interactions and swirl flow.

Chapter 2.

Literature review

2.1. Diesel combustion models

Over the last two decades, the ability to visualise the in-cylinder processes brought upon by the application of optical/laser-based imaging diagnostics has drastically improved the understanding of diesel combustion. Having combined multiple diagnostics such as luminosity imaging, chemiluminescence imaging, and laser-induced diagnostics, Dec proposed a conceptual model for diesel combustion inside a heavy-duty engine in 1997 [4]. This widely accepted model suggests that liquid fuel vaporises shortly after being injected due to hot air entrainment and mixing, leading to the onset of premixed combustion which ignites at a certain distance away from the injector nozzle. Fuel and air then continue to mix and react while releasing heat energy, leading to the formation of high-temperature diffusion flame layer at the jet periphery. Most of the harmful emissions such as soot and nitrogen monoxide are produced during this mixing-controlled combustion period. The illustration of this conceptual model is shown in Fig. 2.1.

Since then, there have been many important and informative follow-up studies based on Dec model. For example, the lift-off length, defined by distance from the nozzle to the closest reaction zone was found to correlate well with the nozzle diameter, injection pressure, and

ambient air entrainment, as well as to impact downstream soot formation [5-11]. When new diesel combustion regimes such as highly diluted low temperature combustion (LTC) were implemented, it was found that the extended ignition delay period induces two-stage ignition processes that comprise of (1) first-stage, low-temperature reaction in which the major reactions involve the decomposition of fuel and (2) second-stage, high-temperature reaction in which the high heat release occurs due to exothermic reactions and hence, produces a large quantity of hydroxyl radicals [12-14]. Interestingly, the new combustion regime also impacts the flame structures such that the high-temperature reaction zone highlighted by OH-PLIF signal appears as a cloud-like structure, unlike the thin periphery zones observed under conventional heavy-duty combustion regime [13].

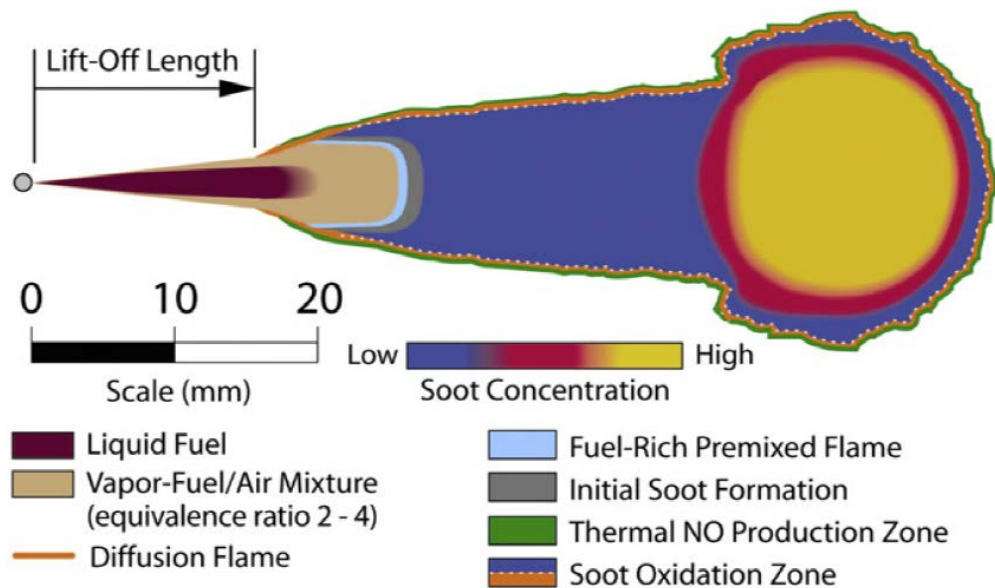


Figure 2.1 Dec's conceptual model for conventional diesel combustion during quasi-steady period in the jet development. (Reprinted from Ref. [4])

2.2. Impact of jet-wall interaction and swirl flow

The diesel combustion model requires a significant revision if jet-wall interaction and in-cylinder swirl flow are to be considered. When an injected jet interacts with the piston-bowl or

cylinder walls, in-cylinder flow field, mixture and temperature distributions along with pollutants formation can be altered [15-19]. Indeed, previous studies found that the jet-wall interactions can restrict the mixing near the impingement point but will improve the local mixing in the jet head region due to the formation of a turbulent ring-vortex, where foregoing fuel droplets decelerate and become stagnated due to the incoming fuel droplets [15, 18-20]. The schematics for these vortices formations can be found in Fig. 2.2. Furthermore, jet-wall interactions also impact the combustion efficiency associated with wall wetting and heat transfer through the wall [21, 22]. For instance, the cooling effect of the wall is also believed to help reduce the soot formation [20] whereas wall wetting can lead to increase in soot emissions [23]. In other studies where soot formation and jet-wall interaction were investigated, it was reported that hot combustion products at the periphery of fuel-air mixture can be redirected back towards the centre of the combustion chamber during long-injection, high-load conditions, and possibly be entrained back into the incoming diesel jet [24-26]. This entrainment of hot combustion products (i.e. re-entrainment) could decrease the lift-off length, thereby increase the soot formation [27-29].

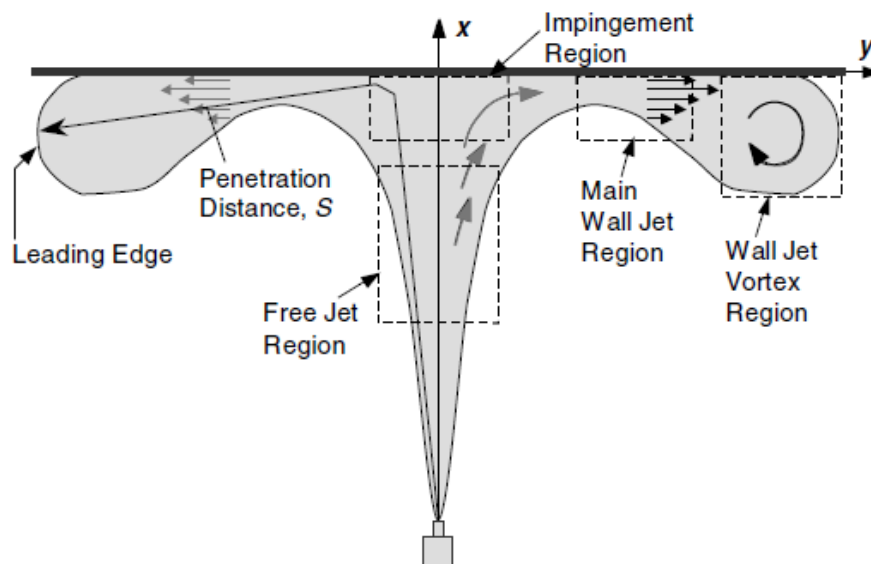


Figure 2.2 Wall-interating jet in a combustion chamber. (Reprinted from Ref. [20])

The in-cylinder swirl flow is known to have huge impact on diesel combustion [30-32]. Higher swirl ratios and therefore higher swirl flow velocity can improve the pre-combustion fuel-air mixing while causing jet asymmetry such that the lift-off length is longer on the up-swirl side of the jet (the side that is penetrating against the in-cylinder swirl flow) than on the down-swirl side (penetrating with the in-cylinder swirl flow) [30, 31, 33]. Some studies suggested that swirl flow also has a strong effect on the late-cycle oxidation process in which higher swirl ratio promotes the soot oxidation and burnout of unburnt hydrocarbons [30, 34].

The severity in the impact of jet-wall interactions and swirl-flow is higher in light-duty diesel engines than heavy-duty ones because the piston bowl and combustion chamber wall is much closer to the injector nozzle [14, 22, 30, 35-43]. The effect of swirl flow is also more significant due to the higher swirl required to compensate for the limited mixing time at high-speed conditions [30, 44]. As a result, the fuel jet has no time to achieve a quasi-steady state or to establish a flame base as in the conventional diesel combustion model but develops in a transient manner instead.

2.3. Effect of injection pressure on the jet development

It is well-known that high-pressure injection of up to 200 MPa [45] can improve fuel-air mixing and thus the engine efficiency significantly because high injection momentum leads to longer vapour penetration [46, 47] and enhances ambient gas entrainment [48-50]. High injection pressure also induces longer lift-off length and lower equivalence ratio at the flame base, causing reduced soot formation [50-52]. Moreover, it was also reported that the increased injection pressure leads to decreased emissions of unburned hydrocarbons (uHCs) and carbon monoxide (CO) [53-55]. As far as jet-wall interaction is considered, the increased injection momentum will enhance the head vortex, then increases the overall mixing and suppresses soot formation [56]. However, the higher injection momentum will also intensify jet-wall impingement [18, 20, 27, 28, 57, 58] and therefore the soot formation might increase in the

region instead. The increased possibility for re-entrainment [17] due to the increased injection momentum could also lead to the shorter lift-off length and thereby increase the downstream soot formation.

2.4. Soot processes inside diesel engines

For diesel engines, soot is one of the most distinctive and problematic emissions due to its complex formation and oxidation processes together with its adverse impact on human health. While after-exhaust treatment systems such as diesel particulate filter are becoming increasingly popular, the in-cylinder soot control continues to play a key role in reducing engine-out particulate emissions. For instance, high and near-constant injection pressure achieved using a common-rail system, together with small nozzle holes, have been widely used to increase fuel-air mixing and thereby reducing the soot formation [45, 49, 51, 59, 60]. As the soot reduction technology advances, our scientific understanding of in-cylinder soot processes has also been significantly improved thanks to non-intrusive optical and laser diagnostics [61]. For instance, studies conducted in heavy-duty diesel engines running at medium-to-high load conditions reported that the first soot formation occurs right downstream of the flame base during the premixed burn phase of diesel combustion then during the mixing-controlled burn phase, soot develops towards the downstream region and across the whole cross-section of the jet; a high soot concentration zone is formed at the jet head [4, 5, 9, 10]. At low-load conditions, the charge dilution can be used to extend the pre-combustion mixing time and limit the flame temperature below the soot formation threshold [13]. In this regime, high-temperature reaction occurs mostly after the end of injection and the soot only forms far downstream in the jet head region [14].

In order to find methods of reducing soot emissions, soot oxidation is also extensively investigated. For instance, it has been known that reduced ambient oxygen concentration and lower flame temperature lead to a lower oxidation rate [11, 14, 62]. The soot oxidation due to

hydroxyl radical (OH) is also a major player, especially at a high flame temperature range above 2000 K [61, 63, 64]. One study reported that soot oxidation by OH is even stronger than the CO oxidation by OH [32]. As a result, many studies have been carried out about the imaging of both soot and OH to analyse soot oxidation processes in diesel engine environments [11, 13-15, 35, 62-66]. As expected, they have all reported the active soot oxidation by OH, evidenced by the disappearance of soot pockets where OH radicals co-exist.

2.5. Optical/laser diagnostics

In the present study, planar imaging of laser-induced OH fluorescence (OH-PLIF) and fuel fluorescence (fuel-PLIF) as well as planar laser-induced imaging of soot incandescence (PLII) were performed in an automotive-size, optical diesel engine. These images were supported by line-of-sight integrated images of cool-flame chemiluminescence and naturally excited OH (OH*) chemiluminescence. The theoretical background of these diagnostics will be presented in this section.

2.5.1. Cool-flame chemiluminescence

During the first-stage, low-temperature ignition phase of diesel combustion, weak chemiluminescence signals are emitted in the 360 – 560 nm range from formaldehyde (HCHO) and other products through the breakdown of ketohydroperoxide (KHP) species [12, 14, 58, 66, 67, 68]. Typically, because of their extremely weak signals, this cool flame chemiluminescence is captured using an intensified charge-coupled device (ICCD) camera together with a UV-enhanced lens without any optical filters. The images can then be used to qualitatively describe the first-stage ignition.

2.5.2. Excited hydroxyl (OH*) chemiluminescence

Electronically-excited hydroxyl (OH*) radicals are formed from high-temperature exothermic reactions of hydrocarbons at near stoichiometric condition (e.g. $\text{CH} + \text{O}_2 \rightarrow \text{CO} + \text{OH}^*$) [69]. As the excited OH* radical return to ground state (OH), the emitted

chemiluminescence signal dominates in the 306–310 nm range and hence, could be isolated and recorded [26, 68, 69]. Therefore, the OH* chemiluminescence images capturing these signals are useful for identifying high-temperature reaction zones within the flame [26, 28, 47, 66, 68], where a high heat release occurs.

It was noted that OH* chemiluminescence can be interfered by the broadband emissions from other sources, most notably from soot incandescence. Since the strongest emissions from soot luminosity are in the visible and infra-red ranges, a band-pass filter centred in the OH* chemiluminescence emission range is needed to blocking strong signals at and above 350 nm. However, as the intensity of the soot luminosity becomes very strong, it is impossible to block the signals completely using optical filters. Therefore, OH* images at later crank angle locations can include some soot signals. It was however found in previous studies that the line-of-sight integrated soot luminosity signals are well within the OH* chemiluminescence regions, i.e. the soot signals are surrounded by OH* signals [26]. Being within the OH* boundary, soot particles and their precursors could not attenuate OH* signal at the flame boundary. Nevertheless, OH* chemiluminescence should not be discussed when the soot luminosity signals are overwhelmingly strong later in the combustion cycle. Futhermore, being line-of-sight integrated image, OH* chemiluminescence lacks clarity in the information it carries. One would not be able to determine which particular part of the jet the OH zones are from. It would be ideal if the primary role of OH* chemiluminescence images was to support the interpretation of OH-PLIF images.

2.5.3. Hydroxyl planar laser induced fluorescence (OH-PLIF)

Background theory

When the diesel combustion enters its mixing-controlled burn phase, most naturally-excited hydroxyl (OH*) radicals have returned to their ground state and only the ground-state OH is further produced [68, 71, 72]. During this period, planar laser-induced fluorescence of hydroxyl

(OH-PLIF) imaging is widely used to study the diesel flame development due to its ability to selectively detect radicals spectrally and temporally at even sub ppm levels [5, 40, 72]. The OH-PLIF detects the fluorescence signals emitted when OH radicals excited selectively to an upper energy level by a high energy laser beam returned to their ground [73]. It should be noted that given its nature, OH-PLIF can also work well during premixed combustion phase.

However, the laser-induced fluorescence process of OH is not straightforward in engine environments. For example, collisional quenching of OH radicals can decrease the yield of fluorescence signal during the molecule deactivation process through collisions with other reaction species and combustion products, mainly H₂O, CO₂ and O₂ [74, 75]. To avoid this quenching issue, a fluorescence excitation scheme should be carefully selected to ensure that the lifetime of OH in the excited state is relatively short. Many different excitation wavelengths and fluorescence schemes have been employed to achieve this goal as summarised in Table 2.1.

Table 2.1 Advantages and disadvantages of different OH-PLIF excitation schemes

| Fluorescence excitation schemes | Excitation wavelengths | Advantages | Disadvantages |
|---------------------------------|------------------------|---|--|
| $A^2\Sigma^+ - X^2\Pi (0,0)$ | Around 308 nm | Good fluorescence yield Readily available high power source. | Vulnerable to changes in temperature and pressure. Dependent on gas composition |
| $A^2\Sigma^+ - X^2\Pi (3,0)$ | Around 248 nm | Quenching can be negligible at low pressure (below 1 MPa) [75] | Weak yield |
| $A^2\Sigma^+ - X^2\Pi (1,0)$ | Around 283 nm | Strong fluorescence yield from two fluorescence transition Quite resilient to temperature and pressures. | Require high excitation power |

Engine-specific implementation

Due to its resiliency with temperature and pressure effects, the excitation laser wavelength most commonly used for the OH-PLIF imaging in the engine environments is 284 nm or 283 nm (vacuum wavelength) for the fluorescence scheme of $A^2\Sigma^+ - X^2\Pi (1,0)$ [13, 39, 72]. The 284-nm wavelength corresponds to the overlapping rotational-vibrational $Q_1(9)$ and $Q_2(8)$ lines [11, 13, 72] while the 283 nm corresponds to the $Q_1(6)$ line of this scheme [38, 39, 42]. Both would work well for OH-PLIF diagnostics in a diesel engine with 284 nm potentially yielding more signals. The resulting fluorescence emissions are mostly found in the 308~320 nm range as was reported in Ref. [74, 77] as well as from LIFBASE simulation of OH-PLIF emissions shown in Fig. 2.3. The present study follows this fluorescence scheme and it can also be referred to as online OH-PLIF.

For the practical imaging of OH-PLIF, it is important to use optical filters to isolate the emitted signals from other emissions sources. For instance, bandpass filters have been widely

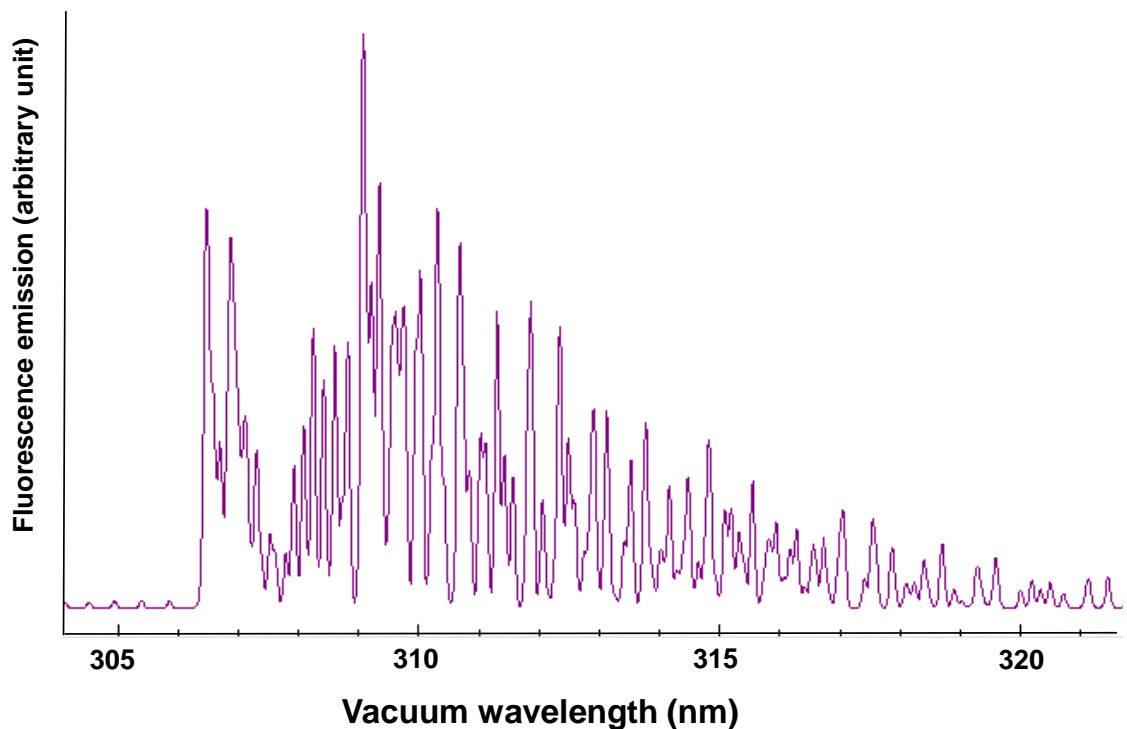


Figure 2.3 OH-PLIF emissions from 284 nm excitation – simulated by LIFBASE

adopted for OH-PLIF, especially the ones centred in the OH emission range such as 312 nm (16 nm FWHM) [13, 32, 39, 71], 310 nm or UG5 band pass filters [38, 42]. In some cases, shortwave filters such as 358 nm short-pass [13, 39, 71] or long-pass glass filters such as WG 305 [42, 58, 72, 78] were also added to further reduce background noise (e.g. excitation laser scattering) and interferences.

Challenges and mitigation strategies

Offline OH-PLIF

While the optical isolating filters are extremely useful, interference signals from the fluorescence under UV excitation of other combustion products such as polycyclic aromatic hydrocarbons (PAH) and natural signal from soot luminosity can still be quite problematic [13, 40, 71, 78]. As some of these interferences are broadband signals, they are unavoidable even with the use of a series of optical filters. However, one good and proven method to address this issue is a comparison between online and offline OH-PLIF images. It is well known that OH fluorescence absorption and emission change drastically with an insignificant difference in the excitation wavelength [71, 77]. By comparing images taken under the laser wavelength tuned on and off the OH excitation fluorescence line, the location and intensity of the interferences can be identified [40, 58], which help interpret the online OH-PLIF images for the high-temperature reaction zones within the diesel flame. For example, the offline images can be taken with the laser wavelength around 283.9 nm (i.e. 0.1 nm off to the OH excitation wavelength of 284 nm).

Line broadening

One outstanding issue concerning the excitation wavelength selections is that high temperature and pressure environments of diesel engines can cause alteration to the fluorescence physics through phenomena known as collisional broadening and collisional shifts. Collisional broadening (widening of absorption line width) and shifts (changing of the absorption frequency) are both proportional to pressures as well as to their respective coefficients. These coefficients, calculated by Davidson *et al.* [79], show a high temperature dependency:

$$\text{Collisional broadening coefficient: } 2 \cdot \gamma_{OH-Ar} = 0.140 \cdot \left(\frac{300}{T}\right)^{0.75} \quad (3.1)$$

$$\text{Collisional shift coefficient: } \delta_{OH-Ar} = -0.0305 \cdot \left(\frac{300}{T}\right)^{0.45} \quad (3.2)$$

Therefore, it can be difficult to have an accurate measurement of the impact of these phenomena. One way to tackle this issue is to scan across the wavelength range of choice (around 284 nm) at a particular timing during the combustion period at which OH-PLIF interferences (e.g. fuel-PLIF) are fully consumed and that the OH population is very high to determine the settings that can provide the best signal-to-noise results.

2.5.4. Fuel planar laser-induced fluorescence (Fuel-PLIF)

Conventional diesel fuel contains many aromatic hydrocarbons and additives (e.g. naphthalene and alkyl benzenes) known to produce strong fluorescence signals due to UV excitation [17, 80]. However, the fluorescence spectrum of aromatics does not display the fine-scale structure of OH-PLIF, resulting in broadband emissions from a wide band of excitation wavelengths and thus fuel-PLIF signals can overlap the OH-PLIF emission range when under UV excitation [13, 58]. Even when single component fuels are used, fuel fluorescence signals still exist [13]. Therefore, the fuel-PLIF is a major interference signal in OH-PLIF imaging. However, it can provide useful information about the vapourising diesel jet development prior to the start of combustion as long as the measured in-cylinder pressure, calculated heat release rate traces and OH* chemiluminescence imaging can confirm no high-temperature reactions take place. Due to these characteristics, signal from offline OH-PLIF can be considered as fuel-PLIF during the non-reacting period.

2.5.5. Soot planar laser induced incandescence (Soot-PLII)

A powerful laser beam can be used to heat up soot particles so that strong incandescence signals are released for the planar imaging of soot distributions within the flame [81] – i.e. PLII. In selecting the laser wavelength, shorter wavelengths (e.g. 355 and 532 nm) has the potential to produce high incandescence energy at lower power level; however, longer wavelength (e.g.

1064 nm) is more widely used to avoid interferences with polycyclic aromatic hydrocarbons (PAHs), which can be significant when shorter wavelengths are used [82-85]. For qualitative diagnostics, to combat the lower heating potential of longer laser wavelength, laser output energy higher than the fluence limit for the vaporisation of soot particles should be used ($> 0.2 \text{ J/cm}^2$ for 1064 nm). The high power laser beam can also mitigate the shot-to-shot fluctuations. Due to the high temperature that the soot particles reach, the emissions from laser-induced incandescence are predominant in the visible and UV range (below 500 nm) [85, 86]. However, the strong laser fluence can also cause fluorescence signals from C_2 at around 500 nm, as seen in Fig. 2.4 [85], which requires the use of optical filters. This study will employ PLII only for qualitative purposes

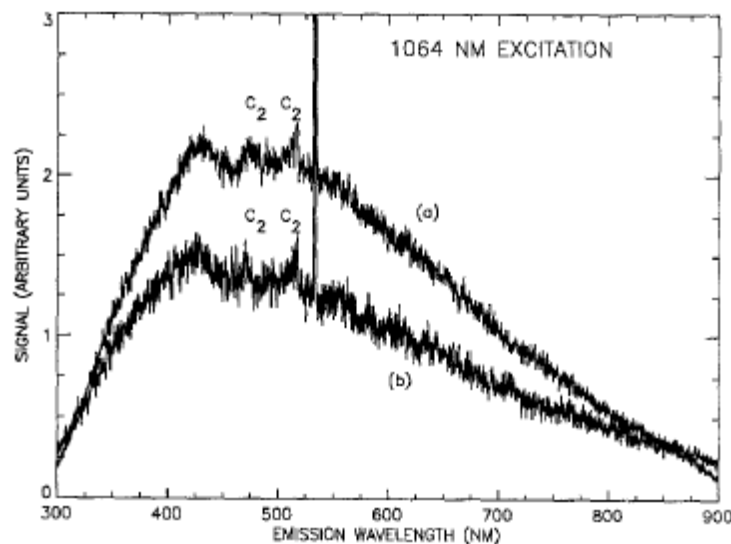


Figure 2.4 Reproduced from Ref [85]: Emission spectra of LII signals from an ethylene/air burner with 1064 nm excitation, 50 ns detection gate for 67 MW/cm^2 (a) and 10 ns detection gate for 153 MW/cm^2 laser-pulse power (b).

Chapter 3.

Methodology and apparatus

Besides all optical diagnostics reviewed in the previous chapters: OH-PLIF, fuel-PLIF, soot-PLIF and chemiluminescence imaging, in-cylinder pressure measurement was also conducted to identify the combustion phases of corresponding images and to assist their physical interpretations for the construction of the combustion model. Their experimental setup details together with the apparatus used, including the optical engine and laser systems are presented in this chapter. Notably, throughout the PhD study, two different piston designs were tested; initially a simple cylindrical bowl design was used and then it was updated to include a curved bowl wall for better reproduction of practical engine conditions. The two different piston bowl shapes used in this study and the piston modifications required for optical/laser diagnostics were discussed in detail.

3.1. Experimental apparatus

All apparatus are located in the Engine Research Laboratory of the University of New South Wales. The engine and its supporting system were fixed to the laboratory floor using a combination of dampers, steel and aluminium frames. Laser systems and diagnostics equipment were positioned on optical tables and mounting frames surrounding the engine system. The lab environment was controlled to ensure consistent operating conditions for all equipments.

3.1.1. Optical compression-ignition engine

The optical engine is an amazing tool for engine research, enabling the applications of optical diagnostics for real-time capturing of complex in-cylinder behaviours. However, certain differences do exist in the heat transfer characteristics of a single-cylinder optical engine and a full metal, multi-cylinder engine. Therefore, the operation of optical engines require careful working strategies including the use of heated coolant recirculation, skip-cycle fuel injections and intake air temperature control as found in Ref. [11, 36, 87, 88] to ensure satisfying results.

The optical compression-ignition engine used in this study is a single-cylinder optical engine which was modified from a 2.0-litre, 4-cylinder production engine. Figure 3.1 displayed the exploded view of the whole engine assembly, including the engine head, cylinder-liner assembly, piston assembly, crank case and other operating parts. Compared to the production version, alterations were mainly done to the cylinder liner body and the engine head remains

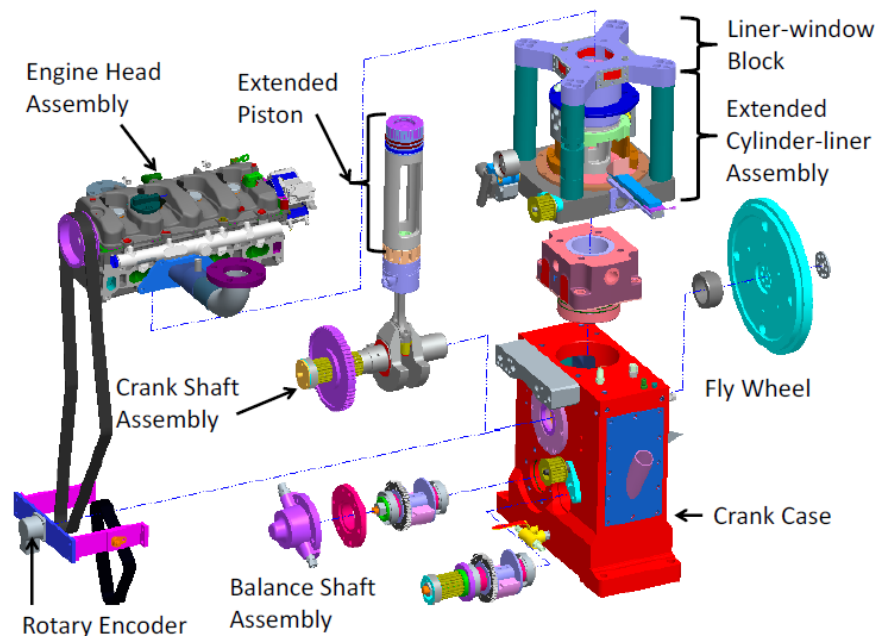


Figure 3.1 Exploded view of the light-duty optical engine

unchanged except the fact that only one cylinder was used. An added liner-window block containing quartz window provides the optical access from the sides of the combustion chamber while the extended liner body allows the use of a drop-down-type liner for ease of access during very frequent windows cleaning procedures. Copper washers, seals and gaskets were carefully applied between all the connecting parts to ensure the integrity of the engine during operation.

Table 3.1 summarises the engine specifications and the operating conditions that were used throughout this study. Figure 3.2. also shows a simplified illustration for the cross-section view of the optical engine and image capturing setup. Other operating parameters corresponding to specific investigations will be described later in this thesis where appropriate. The engine has 83 mm bore and 92 mm stroke for a displacement volume of 497.5 cm³. The combustion chamber is bounded by a cylinder liner, the piston top, and a flat cylinder head (fire-deck) where a

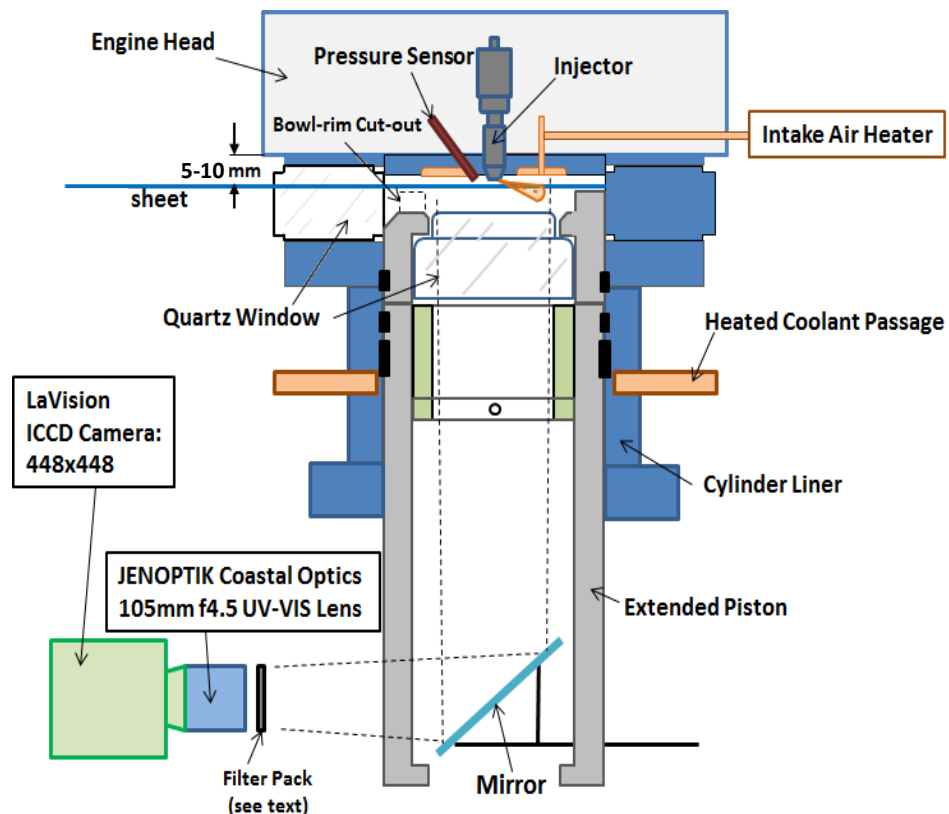


Figure 3.2 Illustrated schematics of the optical diesel engine and the image capturing setup

centrally mounted injector nozzle, two intake valves and two exhaust valves were placed. The locations of these valves induce a clock-wise in-cylinder swirl-flow when bottom-view of the combustion chamber was imaged through the piston window. The engine is naturally aspirated and has a swirl ratio of 1.4. The optical access for image capturing was made possible through the quartz window in the piston top and a 45° mirror placed in the hollow space of the extended piston body, as well as the quartz cylinder liner windows mentioned earlier (as seen in Fig. 3.2). With its original piston, the compression ratio was 17.7. The wall temperature was held constant at 363 K using heated water circulated through the cylinder head, liner and engine block to simulate warmed-up operating conditions. The intake air temperature was held at 303 K throughout the experiments. Bulk gas temperature and density at the beginning of combustion at this operating condition was estimated to be 858 K and 11.16 kg/m³.

Table 3.1 Engine specifications and operating conditions

| | |
|---|---|
| Displacement (single-cylinder) | 497.5 cm ³ |
| Bore | 83 mm |
| Stroke | 92 mm |
| Swirl ratio | 1.4 |
| Compression ratio (geometric – original) | 17.7 |
| Wall (coolant) temperature | 363 K |
| Intake air temperature | 303 K |
| Injector type | 2 nd -generation Bosch common-rail |
| Number of holes | 1 |
| Nozzle type | Hydro-grounded, K1.5/0.86 |
| Nozzle diameter | 134 μm |
| Included angle | 150° |
| Engine speed | 1200 rpm |

A second-generation Bosch common-rail system, including low and high pressure pump and a solenoid injector, was used for the injection of fuel. The original injector had seven 134- μm (nominal diameter) holes with 150° included angle. In the present study, only one hole was left open for fuel injection using a laser-welding technique to block the other 6 holes. The single jet approach was to accommodate long injection duration, simulating high-load conditions per hole basis while keeping the peak in-cylinder pressure within the burst pressure limit of optical windows and to ensure that the single jet development was isolated from complex jet-jet interactions (this was left for future investigations). This injection condition will result in a long wall-interacting period, needed for the detailed study of jet-wall interaction phenomena. The injected fuel mass was held constant at 10 mg per injection per hole, which indeed corresponds to high-load conditions in production engines. The engine was operated at a 10 skip-firing mode with the injection occurring every 10^{th} cycle (i.e. 9 motoring cycles and 1 firing cycle), the reason for which was to reduce thermal loading on the quartz windows for safety measures as well as to minimise residual gases from previous firing cycles for reduced cyclic dispersions. The engine was driven by a 37 kW AC motor at a fixed speed of 1200 revolutions per minute (rpm) throughout the study.

3.1.2. Piston designs

It is well understood that the impact of piston bowl geometry on diesel flame development is very significant [27, 78] and thus its clear definition important. Two different piston designs were used in this study, both containing the same extended hollow piston body with the same height and diameter. The main difference between the two designs lies in the piston top.

Piston A

Figure 3.3 shows the design of Piston A. The top of this piston contains a cylindrical piston-bowl with 55 mm in diameter and 10.5 mm in depth. The straight bowl wall of this piston was designed for the study of jet-wall interaction phenomena at simplified wall conditions. The piston top contains a flat surface (i.e. no dome or pip in the bowl) quartz window for ease of

optical access. The window was positioned concentrically with the piston bowl and the field-of-view given by this piston window was 43 mm in diameter. The thickness (or height) of the quartz window was determined using a burst pressure equation as shown in Ref [89]:

$$P_{allow} = \frac{(3.48 \times t^2 \times M)}{A \times SF} \quad (3.1)$$

where the allowable pressure P_{allow} is a function of the thickness of quartz, t , the modulus of rupture of quartz, M , the unsupported area, A , and the safety factor, SF .

Further modifications to the piston top were made to allow access to the bowl region for the laser sheet of planar laser-based diagnostics even when the piston was at top dead centre (TDC). A 33-mm wide, 10.5-mm deep portion of the piston-bowl rim was removed in line with the liner quartz window. It is noted that the full-cycle engine modelling of this piston design confirmed that this bowl-rim cut-out does not affect the in-cylinder swirl flow direction (which is clockwise with the current engine design) [90] and its effect on the jet development can be negated

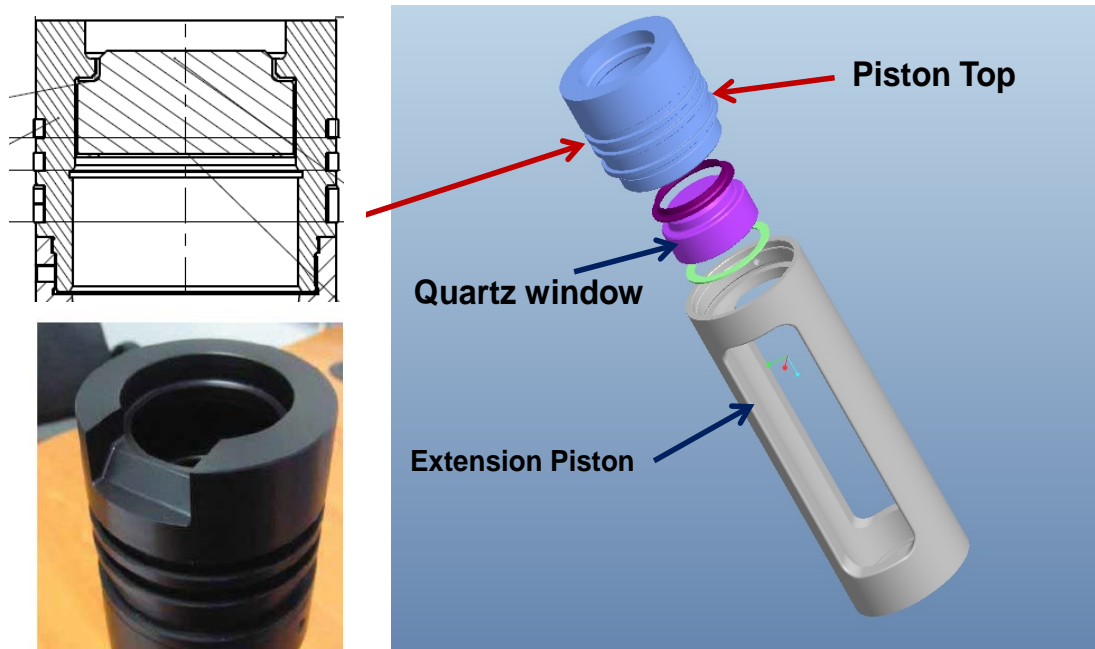


Figure 3.3 Piston A design

by appropriate choice of the orientation of the selected single injector hole. The resultant compression ratio from the piston design A was 15.2.

Piston B

After significant progress having been made using Piston A, it was suggested that the piston should be further modified for two primary reasons. The first was to extend the field-of-view so that it could match the full bowl diameter (Piston A shows only 43 mm in diameter, smaller than 55 mm bowl diameter). The second was that the fundamental understanding obtained using the cylindrical straight-wall design suggested a significant impact of the bowl wall geometry and therefore a need arose for experimenting with a more practical bowl shape which includes a curved wall. The new piston (Piston B) was illustrated in Fig. 3.4. The curved bowl wall was expected to cause more practical jet-wall interaction so that the fuel jet would be guided back towards the nozzle upon the impingement on the wall through a tumbling motion.

It is noted, however, a full quartz piston with realistic bowl shape (e.g. Refs. [14, 22, 30, 35]) was not used for consistency with Piston A and for ease of visualisation. Therefore, Piston

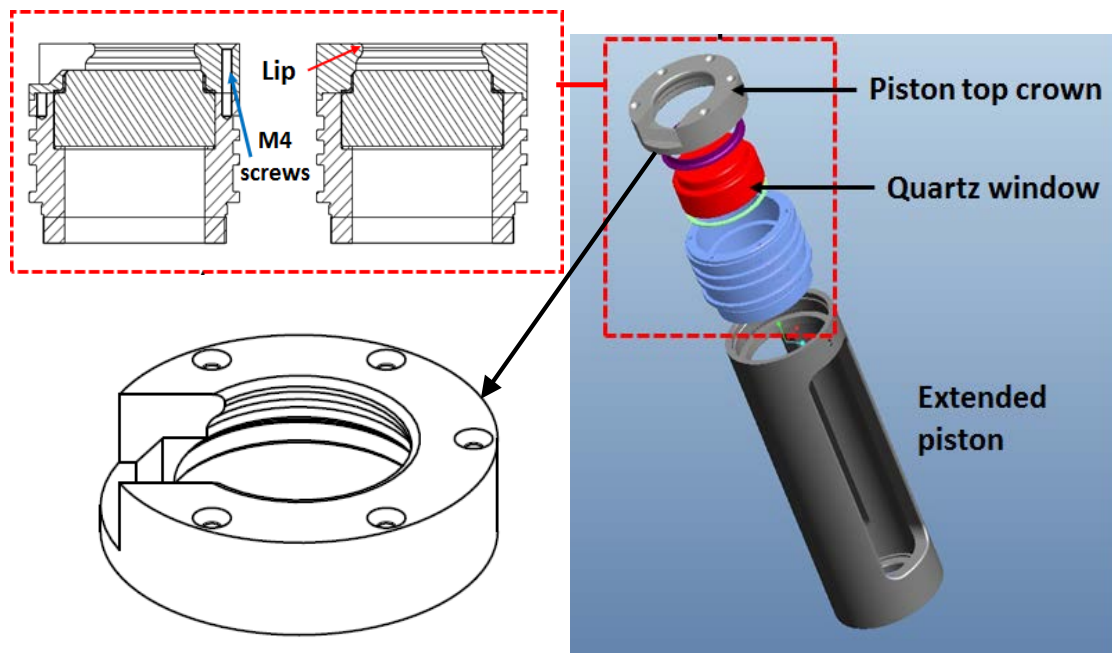


Figure 3.4 Piston B design

B does not include a dome pit within the bowl but maintains the flat bottom, similar to Piston A. The removal of the dome pit (or pip in the bowl) could mitigate the fuel penetration into the squish region [14] and thus the mixture distributions could be different from the production engine, which should be taken into account when interpreting the results. With the new estimated maximum working pressure and the same thickness and safety factor, the new field-of-view matched the bowl diameter of 52 mm with the the bowl depth of 10 mm. The bowl-rim cut-out modification process and its location is also similar to that of Piston A; however, to compensate for the wider laser coverage required for a wider field-of-view, the cut-out is expanded to a width of 35 mm. The compression ratio when Piston B was installed was slightly higher at 15.5, compared to 15.2 of Piston A.

In addition, to assist with the experimental setup and to allow for more upgrades and modifications in future work, the assembly process of the piston was also improved. An exploded view of the updated piston assembly is shown on the right of Fig. 3.4. The piston crown is removable from the extended piston and quartz window holder using six M4 screws. The removable crown and the extended piston top act as a clamp after all the screws are tightened to keep the quartz window in place. A combination of copper washer and high temperature silicon gasket were used to ensure that the assembly stay air-tight during engine operation. This design also allows for possibilities of switching and modifying the piston crown without disassembling the piston from the engine block.

3.1.3. Fuel injection control system

The common-rail injection system and the injection parameters including injection timing, injection pressure and injection duration were controlled by a universal engine control unit (Zenobalti 9013P) together with an injection driver unit (Zenobalti 5100). A rotary encoder placed at the engine crankshaft sent a the signal to the universal control unit as a master signal to control the injection timing. The injection timing and duration signal were sent to the driver which was then sent to the solenoid injector. The common-rail pressure applied in this study

ranged between 70 and 130 MPa. The fuel injection timing was fixed at 7 crank angle degrees before TDC ($^{\circ}\text{CA bTDC}$) for all performed experiments so that the ambient condition at the start of injection could be kept constant. The injection duration was varied to keep the injected mass constant at 10 mg per hole. Table 3.2 lists all the injection conditions used in the present study.

Table 3.2 Fuel injection conditions

| | | | |
|---------------------------|------------------------------|---------|---------|
| Rail pressure | 70 MPa | 100 MPa | 130 MPa |
| Injected fuel mass | 10 mg | | |
| Injection timing | 7.7 $^{\circ}\text{CA bTDC}$ | | |
| Injection duration | 2.36 ms | 2.24 ms | 2.02 ms |

Appropriate signals were also sent from the universal controller to allow for 10-skip firing. The fuel injection profiles from these conditions, measured using a Bosch-tube-type injection rate meter, will be used as complementary information in the following chapters.

3.1.4. Laser system

The laser system used in this study consists of two lasers which were selectively used to produce a desired wavelength for each planar laser-based imaging diagnostic.

Nd:YAG Laser

A QuantaRay PRO-230 Nd:YAG laser was employed in this study. This laser utilises trivalent Neodymium ions (Nd^{3+}) inside the yttrium aluminium garnet (YAG) rod; the Nd ions absorb the source radiation (flashlamps or diode lasers) and radiate light. This particular laser model is a water-cooled class IV 10-Hz pulsed laser, capable of producing up to 13 W (1.3 J per pulse) at the fundamental wavelength of 1064 nm and up to 6.3 W (630 mJ per pulse) for the frequency doubled output (532 nm). The laser was controlled externally using a controller/timing unit (LaVision PTU) and LaVision Davis 7.2 software. The laser power was

measured for maintenance and calibration purposes with a power meter (Newport Power Meter 1918-R). For the diagnostics of the present study, the fundamental frequency 1064 nm was used for PLII and the frequency doubled 532 nm laser beams were used as a pumping laser beam for OH-PLIF (both online and offline).

Dye Laser

Although the Nd:YAG laser can produce very high power, its output frequency is limited to the factors of its fundamental frequency (e.g. 1064, 532, 354.6 nm). To produce the desired output wavelength for OH-PLIF, a dye laser (Sirah CobraStretch) was used. This laser beam was also equipped with a beta-barium-borate (BBO) crystal and fine frequency tuning software (Sirah-provided) to further increase the flexibility of the output wavelength. For highly accurate calibration, a wavelength meter (HighFinesse/Ångstrom WS6) was also used at the start of each diagnostics execution.

Laser diagnostics applications

Online and offline OH-PLIF

As described in section 2.5.3, the UV wavelength of 284 nm was selected for online OH-PLIF. To output this wavelength, Rhodamine 6G fluorescence dye was used in the dye laser due to its advantages in having a long life cycle and a good conversion efficiency of more than 25%. When being pumped by frequency-doubled Nd:YAG laser of 532 nm, Rhodamine 6G produces a wavelength in the range of 559-576 nm [91]. This laser beam was subsequently frequency-doubled using a beta-barium-borate (BBO) crystal and fine tuned to obtain an output wavelength at around 284 nm. For the offline OH-PLIF imaging mentioned previously, a wavelength near 283.9 nm was produced using the same method. To deal with the broadening issue, multiple laser wavelengths were scanned around these excitation wavelengths to find the exact best-performing wavelengths for both online and offline OH-PLIF. Table 3.3 lists the laser wavelength and pulse energy for the online and offline OH-PLIF of this study.

Soot PLII

To apply soot PLII in this study, the fundamental frequency of the Nd:YAG laser (1064 nm) was introduced into the combustion chamber. The power of the laser was set to be at the value that correspond to the fluence limit of incandescence intensity to negate the effect of fluctuating laser power. Table 3.3 also lists the selected laser wavelength and pulse energy for soot PLII

Table 3.3 Laser wavelengths and corresponding power level of the laser-based diagnostic techniques

| Diagnostic technique | Wavelength | Pulse energy |
|---------------------------------|------------|--------------|
| Soot-PLII | 1064 nm | 250 mJ/pulse |
| Online OH-PLIF (also fuel-PLIF) | 284.007 nm | >35 mJ/pulse |
| Offline OH-PLIF | 283.875 nm | >35 mJ/pulse |

3.1.5. Sheet-making optics

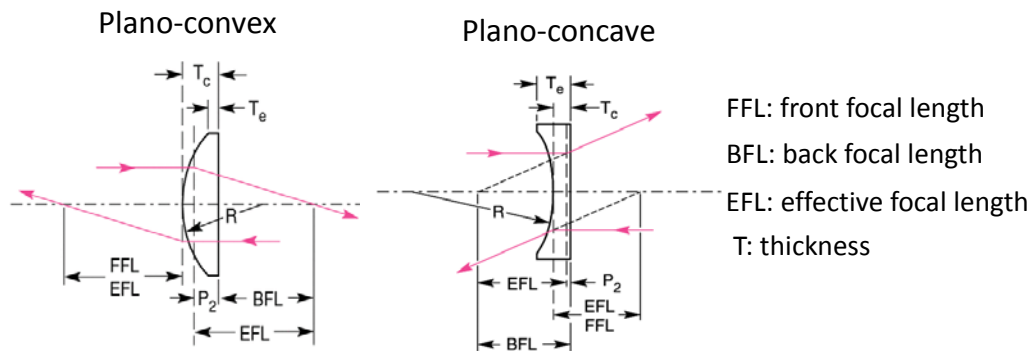


Figure 3.5 Plano-concave and plano-convex illustration. (reproduced from Ref [92])

The PLIF and PLII imaging requires planar laser beam in the form of a thin laser sheet. To transform a collimated and homogeneous beam into a thin laser sheet, three main steps were applied as follows:

- 1) Size reduction of the beam to obtain desired width of the laser sheet
- 2) Stretching of the beam in one direction to obtain desired thickness of the laser sheet
- 3) Collimation of the beam to maintain the thickness

To perform the beam manipulation in only one direction (i.e. a laser sheet), a good mix of cylindrical lenses was required (Fig. 3.5 reproduced from Ref. [92]). A few different possible sheet-making optics setups were identified (as listed in Table 3.4).

Laser coverage of combustion chamber (piston top view)

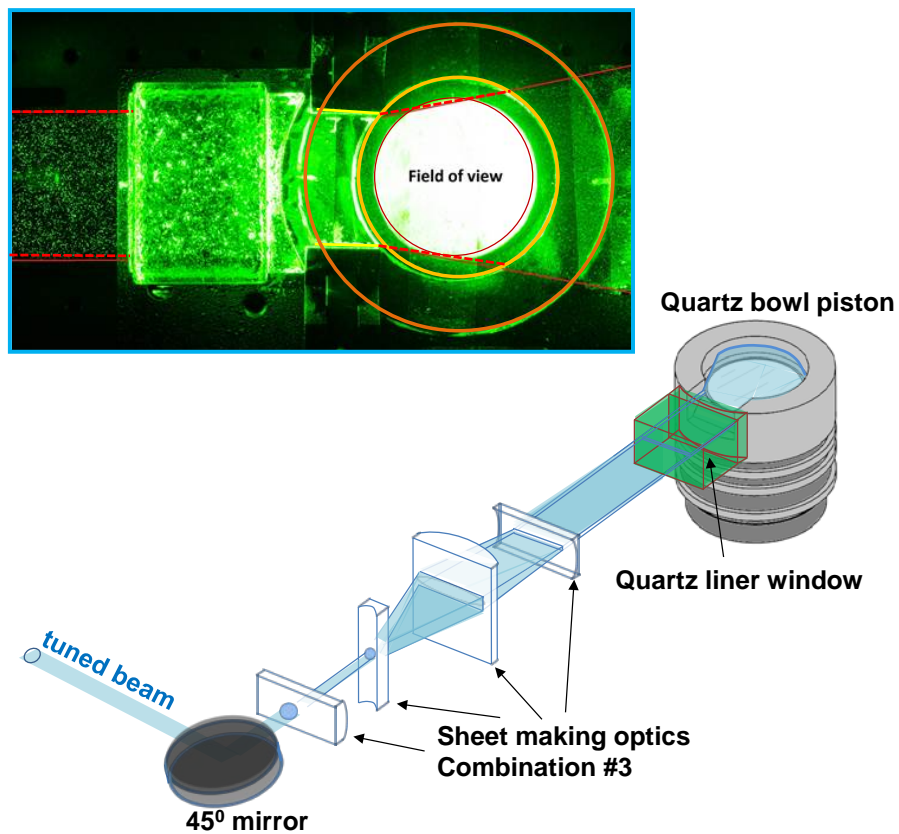


Figure 3.6 Mock-up test and result for the laser sheet coverage of the combustion chamber (top) and the schematics for the sheet making optics setup and optical path for planar laser-based diagnostic (bottom) In this study, the lenses used are: 500 mm EFL plano-convex, -12.7 mm EFL plano-concave, 150 mm EFL plano-convex and -25.4 mm EFL plano-concave, in order of position with respect to beam path.

Table 3.4 Lens combinations for the laser-sheet making optics

| Setup | Lenses | Combination | Pros | Cons |
|----------|--------|---|--|---|
| A | 3 | Plano-convex cylinder lens + plano-concave cylinder lens + plano-convex cylinder lens | <ul style="list-style-type: none"> At the point of interest the sheet will be very thin. The expansion ratio doesn't need to be large | <ul style="list-style-type: none"> The sheet will not propagate homogeneously The focal length required from the focusing plano-convex lens is quite large |
| B | 4 | Plano-convex spherical lens + plano-concave spherical lens + plano-concave cylinder lens + plano-convex cylinder lens | <ul style="list-style-type: none"> The sheet will propagate homogeneously | <ul style="list-style-type: none"> Might be thicker than in combination #1 due to the restriction in the reduction ratio of the spherical pair. Require a bigger expansion ratio in the cylindrical set due to the smaller size of the beam in both directions. Spherical lens alignment |
| C | 4 | Plano-convex cylinder lens + plano-concave cylinder lens + plano-concave cylinder lens + plano-convex cylinder lens | <ul style="list-style-type: none"> The end result is a collimating sheet of light. The expansion ratio in the horizontal direction does not need to be as large as with the combination in setup B | <ul style="list-style-type: none"> The thickness of sheet won't be as small as setup A |
| D | 2 | Plano-concave cylinder lens + convex spherical lens | <ul style="list-style-type: none"> Does not require many lenses. Got a thin sheet at point of interest | <ul style="list-style-type: none"> The focal length of the spherical lens needs to satisfy the distance to the point of interest and the distance between it and the cylindrical lens. Alignment of spherical lens |

In the present study, setup C was selected for its advantages summarised in the table. Also, the alignment was easier than the other setups. Specifically, the original laser beam was converted into a 300 μm thick and 35 mm wide sheet using the sheet making optics as it entered into the combustion chamber via the liner window, as shown in Fig. 3.6. The first plano-convex lens was used to reduce the vertical thickness of the laser beam, followed by a plano-concave lens positioned in such a way as to expand the laser beam horizontally. This horizontal expansion was then stopped by using a second plano-convex lens. That is, the convergence effect cancels out the divergence effect of the plano-concave lens, keeping a constant width for the downstream sheet. The last lens in the series was a plano-concave lens that help cancel out the beam convergence in the vertical direction of the first lens, in order to fix the thickness of the laser sheet entering into the combustion chamber.

One issue of the planar laser setup is that the current cylinder liner window will act as a plano-concave lens, leading to horizontal divergence of the laser sheet. To evaluate this, a mock-up test was conducted in a test bench prior to the engine experiments. Shown at the top of Fig. 3.8, a frequency doubled Nd:YAG laser beam (532 nm), a spare cylinder-liner quartz, a picture of the piston bowl, and two beam dump blocks mimicking the bowl-rim cut-out were used to visualise the beam pass and area coverage for piston type A. The image demonstrates that the diverging laser sheet boundaries denoted by red dashed lines covered the entire field of view provided by the piston bowl quartz window, which is quite beneficial for qualitative imaging.

Chapter 4.

Data capturing and processing

4.1. In-cylinder pressure and apparent heat release rate

A piezoelectric pressure transducer (Kistler 6056A) was installed on the cylinder head in place of the traditional glow-plug to measure the in-cylinder pressure. The data from the transducer were converted to a voltage output using a charge amplifier (Kistler 5015) and recorded in a computer using a data acquisition system (MCC USB-1616HS-BNC). The injection and encoder signals were also recorded using the same system. Furthermore, the pressure data was used to derive the apparent heat release rate (aHRR), Q_{app} , based on a simple one-dimensional energy equation [93]:

$$\frac{dQ_{app}}{d\theta} = \left(\frac{\gamma}{\gamma - 1}\right)p \frac{dV}{d\theta} + \left(\frac{1}{\gamma - 1}\right)V \frac{dp}{d\theta} \quad (4.1)$$

where θ is the crank angle degree, γ is the specific heat ratio, p is the measured in-cylinder pressure at a given θ , and V is the volume of combustion chamber at a given angle θ . The apparent heat release rate was plotted to evaluate the in-cylinder conditions and to help identify the combustion stage at the imaging time.

4.2. Imaging apparatus

Figure 3.2 in Chapter 3 showed a schematic of the imaging and engine setup. An intensified charged-coupled device camera (ICCD) was positioned in-line with the 45° reflecting mirror that was placed inside the hollow extended piston body. Both the camera and the mirror would remain stationary for all experiments while the piston was moving. Only bottom-view image was captured from the optical diagnostics of the present study.

4.2.1. Intensified charged-coupled device camera (ICCD)

A charged-coupled device camera converted the exposure to photon into electric charge based on photoelectric effect. These electric charges can then be recorded and reconstructed to display the image. An ICCD camera is a CCD camera that is coupled with an image intensifier (made up of a photocathode, a micro channel plate and phosphor). It boasts the advantages over a CCD camera of having extremely high sensitivity for its extended UV spectral range and extremely short shutter interval of a few ns, all of which is vital for good diagnostic, especially in engine applications. This study utilised a LaVision Nanostar ICCD camera, capable of having a short shutter interval of 5 ns and a spectral range of 280 – 1000 nm. The camera was equipped with a 105-mm/f4.5 UV-enhanced optical lens, achieving over 85% transmission at 250 - 650 nm range. The same camera was used for various imaging diagnostics of the present study including OH-PLIF, fuel-PLIF and soot-PLII and similarly for chemiluminescence imaging of OH* and cool flame products. For all these diagnostics, at each crank angle location, a total of 20 images were taken from 20 firing cycles. The ICCD camera was controlled by the LaVision Davis 7.2 software and was synchronised with the engine as well as the Nd:YAG laser during capturing events.

4.2.2. Optical filters

Hydroxyls optical and laser diagnostics

As mentioned in the previous chapters, OH-PLIF, OH* chemiluminescence and soot-PLII diagnostics performed in this study require a specific set of filters to isolate the target signals

from interferences. For instance, using an excitation wavelength of 284 nm for the $A^2\Sigma^+ - X^2\Pi$ (1,0) scheme, the OH-PLIF imaging needs to capture signals in the 308-320 nm range to isolate OH signals while rejecting the scattering signals from the excitation laser. The combination of optical filters for OH-PLIF therefore included a 300 nm band-pass filter (40 nm FWHM with around 70% maximum transmission in the range) and a WG-305 glass filter. Figure 4.1 shows the optical transmission curves for these filters. The result signal from OH* chemiluminescence also stays within this range and hence, the same set of filters were used. On the other hand, due to very weak signals, cool-flame chemiluminescence imaging was performed without optical filters.

Soot PLII imaging

For PLII imaging, a longer wavelength of 1064 nm helped eliminate interferences from PAH fluorescence; however, filters were still required to block fluorescence from C_2 and strong natural soot luminosity [84, 85]. One beneficial consideration is that as the soot particles are heated by the energy of a powerful laser beam, the incandescence will be very intense and its emissions will be mainly among the shorter wavelengths below 500 nm and in the UV range. Therefore, in this study, a 430 nm band-pass filter (10 nm FWHM) and a 450 nm short-pass filter were used. Their transmission curve is shown in Fig 4.2.

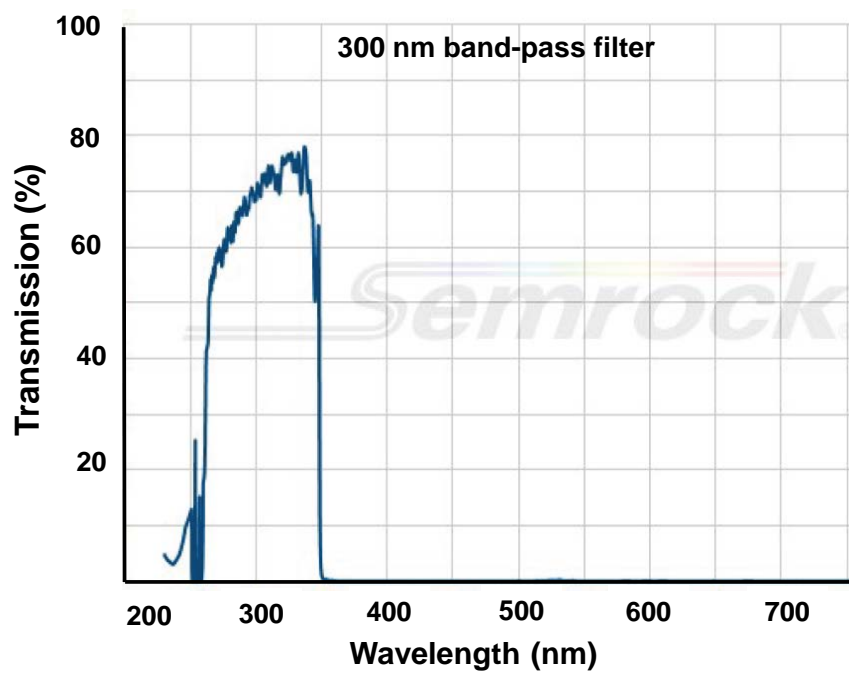
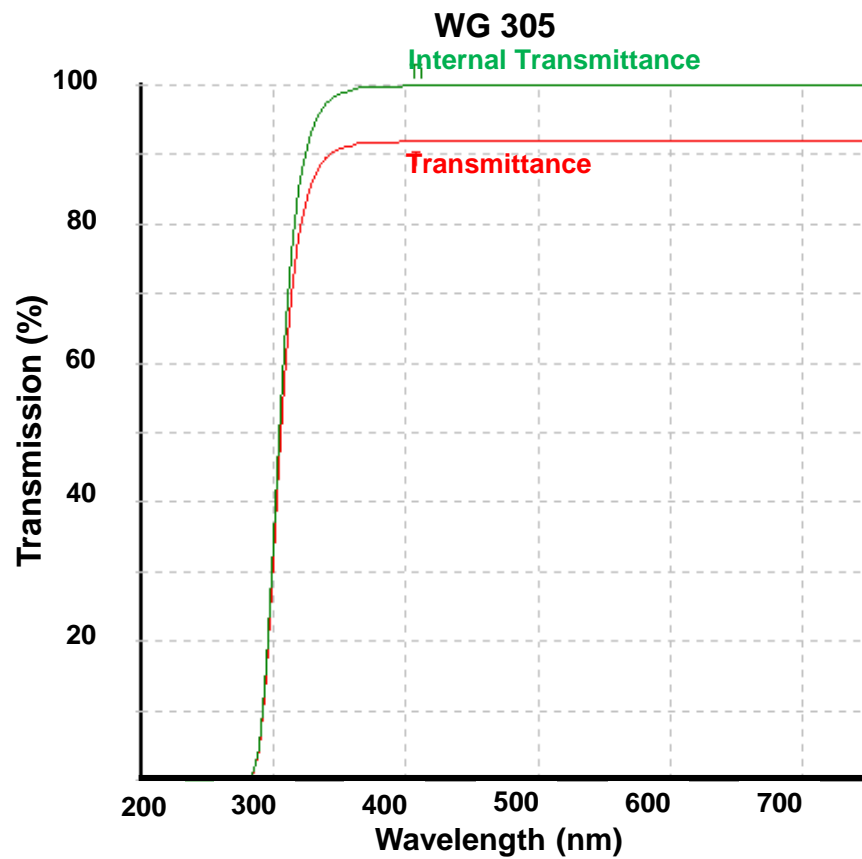


Figure 4.1 Transmittance data for the WG305 glass filter from Schott filter (top) and 300 nm band pass filter from Semrock filter (bottom)

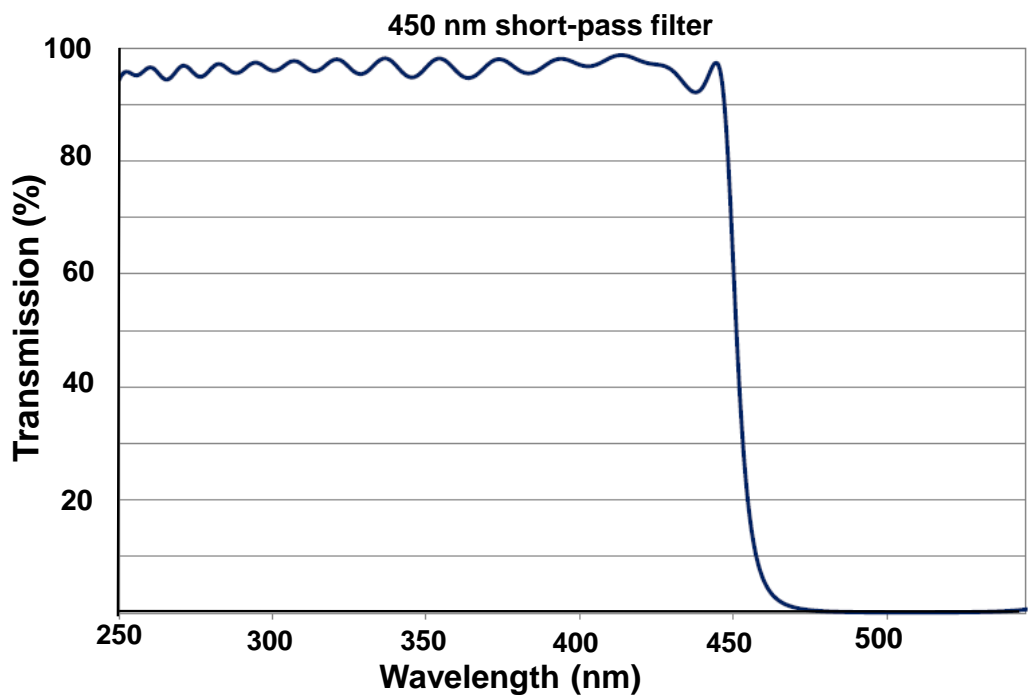
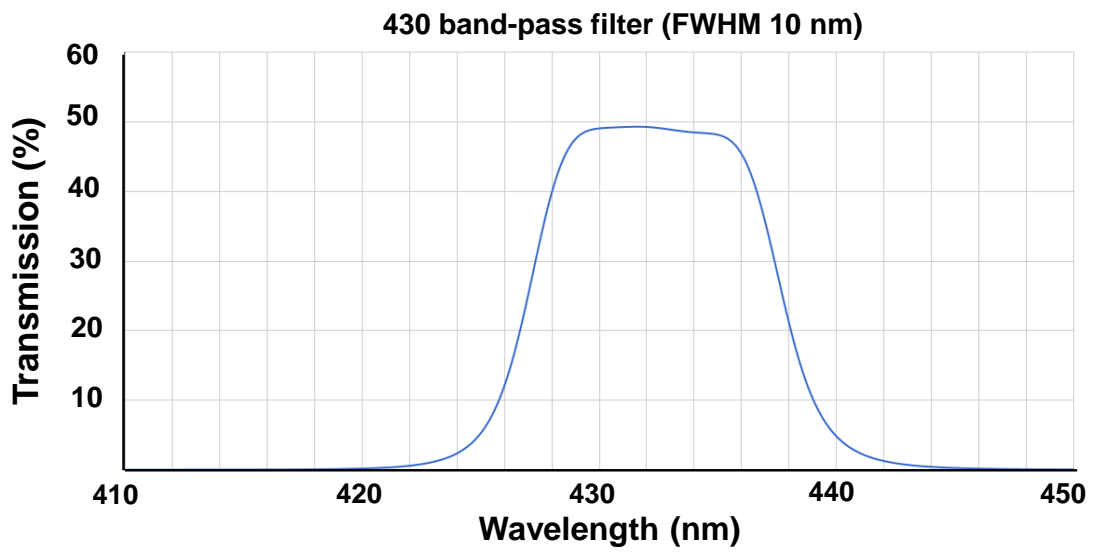


Figure 4.2 Transmittance data for the 430 nm band-pass filter from Andover Corporation (top), and 450 nm short-pass filter from Edmund Optics (bottom)

4.2.3. Capturing synchronisations

To successfully capture the correct information when applying optical diagnostics, especially laser-based diagnostics, accurate synchronisation of all the participating system is absolutely vital. Figure 4.3 shows the timing schematics for the capturing of a typical OH-PLIF image, which is also applicable for other laser based diagnostics. The engine encoder signal is the master signal, and is used to trigger fuel injection as well as to control the timing of camera capturing and the repeating laser emission. The injection occurs every 10 running cycles with engine speed fixed at 1200 rpm, matching the laser pulsing frequency of 10 Hz, which means that the laser beam emission will occur at the same timing for every engine cycle. The shutter-open signal (start capturing) for the ICCD and the lasing signal were triggered from the fuel injection signal and their delay timing was offset from the encoder signal (T); this offset time T is specified by the crank angle locations where the image capturing was determined to occur. For PLIF and PLII, it is desirable to have the laser emission fall in the middle of camera

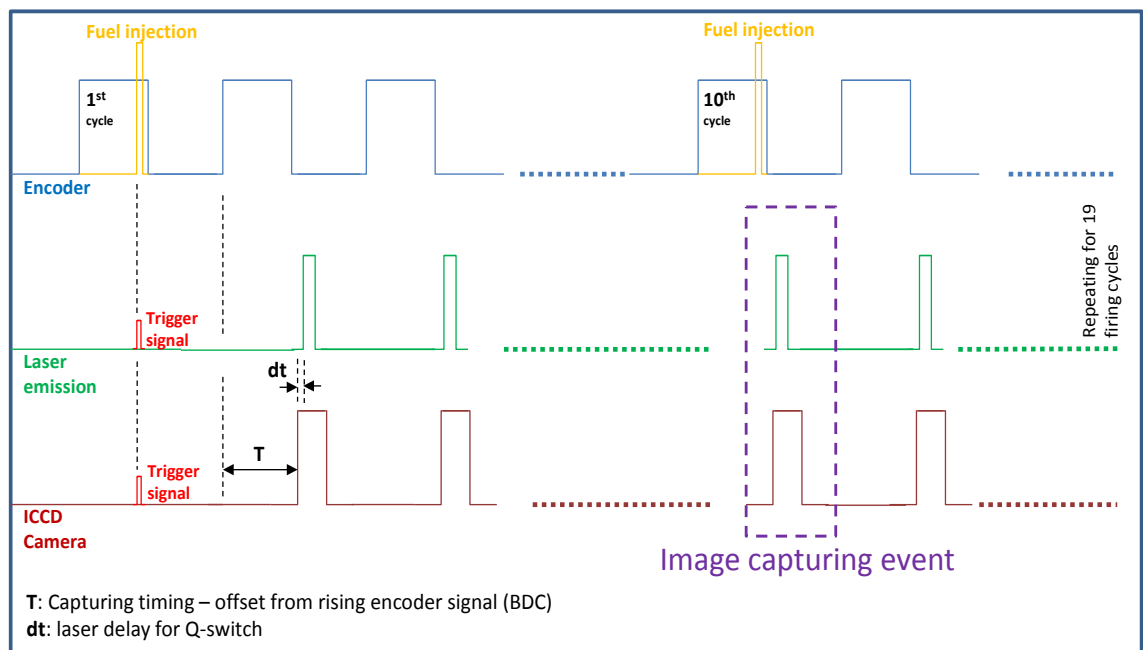


Figure 4.3 Timing diagram for the synchronisation of the engine, laser system and camera for laser-based diagnostics. Laser timing can be disregarded for chemiluminescence imaging

exposure period to maximise the signal strength. Hence, another delay Δt is added to the offset time T for the laser emission signal to accommodate for electronic jittering. The encoder was also installed so that the rising edge of its signal is at bottom dead centre (BDC), making it easy to define the timing of the lasing and capturing event. The synchronisation for chemiluminescence imaging used the same method as the laser-based imaging (without the lasing event).

4.2.4. Capturing parameters

Table 4.1 lists all the parameters of the image capturing system used for the optical diagnostics of this study. The parameters were chosen after multiple trial and error attempts to make sure they can provide the best signal-to-noise ratio as well as a proper saturation level for each diagnostic technique.

Table 4.1 ICCD camera capturing parameters used for each optical diagnostic techniques

| Diagnostic technique | ICCD camera gate (μs) | ICCD camera gain | Optical filters |
|---|--|-------------------------|---------------------------------------|
| Cool-flame chemiluminescence | 100 | 100% | None |
| OH* chemiluminescence | 70 | 25% | 300 nm bandpass and WG305 |
| OH-PLIF (online/offline and fuel-PLIF) | 0.1 | 90% | 300 nm bandpass and WG305 |
| Soot-PLII | 0.05 | 60% | 430 nm bandpass and 450 nm short-pass |

4.3. Image processing and presentation

All captured images from the imaging diagnostics were originally in gray-scale. These images were post-processed using an inhouse-developed MATLAB code. The post-processing procedures include the background noise subtraction, image rotation, pseudo-colouring and annotations. Figure 4.4 shows a sample image that was captured from fuel-PLIF imaging. Its

annotations and styling were used in all other images in the following chapters. The red circle represents the field-of-view bounded by the piston-bowl quartz window. The crank angle locations after top dead centre ($^{\circ}\text{CA aTDC}$) and after start-of-injection ($^{\circ}\text{CA aSOI}$) denoting the imaging timing are shown on the top left and top right corner of the image, respectively. There are scales in mm representing the distance from the nozzle (at the centre of combustion chamber) on the left edge and bottom edge. The online OH-PLIF signals are pseudo-coloured blue. Because more than one imaging diagnostics were applied for the same flame at a given crank angle, different signals were processed to have different false colours, assisting the clarity and interpretation of the images. Table 4.2 summarises the colour used for each signal.

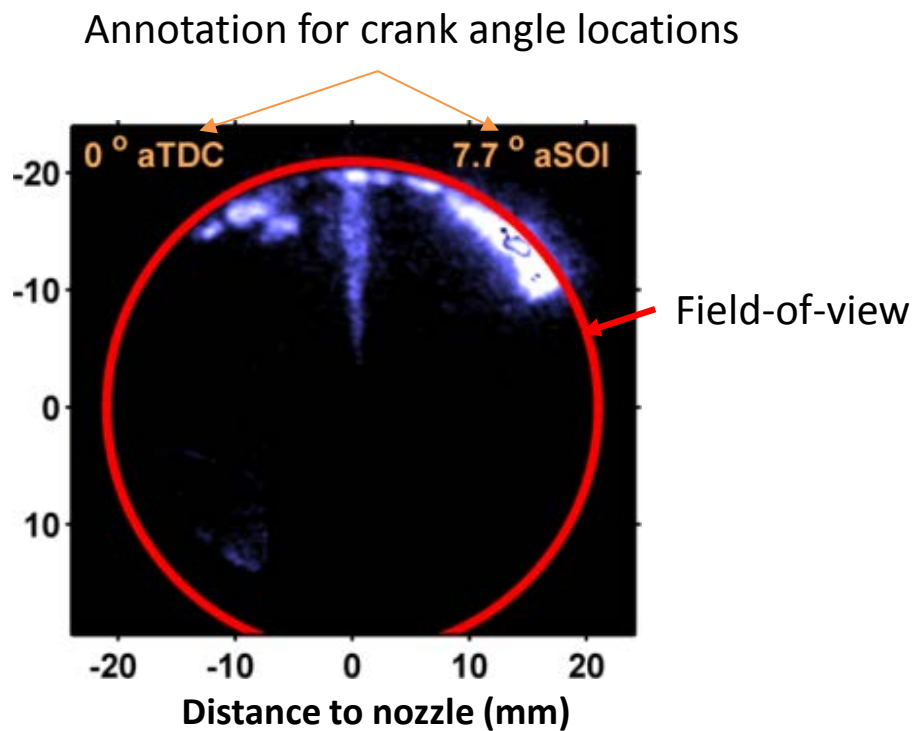


Figure 4.4 An example image from fuel-PLIF taken at TDC with Piston A at fixed operating condition and 130 MPa injection pressure

Table 4.2 Pseudo-colouring for the images from each optical diagnostics

| Optical diagnostics | Pseudo-colour |
|-------------------------------------|----------------------|
| Cool-flame chemiluminescence | Orange |
| OH* chemiluminescence | Light green/cyan |
| Online OH-PLIF | Blue |
| Offline OH-PLIF | Yellow |
| Soot-PLII | Red |

4.4. Cyclic variations

Reacting diesel jets inside the engine cylinder are highly turbulent with irregular mixture and temperature distributions, leading to cyclic variations. To minimise the cyclic dispersion, the optical diesel engine used in this study was operated at fixed wall (coolant) temperature, intake air temperature, and engine speed. The skip-firing also helped reduce the cyclic variations caused by residual gases from previous firing cycles. However, some cyclic variations were still unavoidable.

4.4.1. Variations in in-cylinder pressure data

Figure 4.5 shows in-cylinder pressure traces (top) and corresponding aHRR (bottom) for the fixed operating conditions of Table 3.2 at injection pressure condition of 130 MPa (see Table 3.1 and Table 3.2 for operating conditions). All the in-cylinder pressure traces recorded from 20 firing cycles (black lines) are plotted together with their ensemble-averaged trace (red). The figure shows that the individual traces are very consistent before the combustion started at around 5°CA aTDC, suggesting stable thermal and ambient gas conditions of the engine. However, as the combustion-induced heat release occurs and thus the in-cylinder pressure increasing drastically, some variations are found in the in-cylinder pressure traces. For example, the start of combustion (identified by the drastic pressure rise) occurs at various crank angle

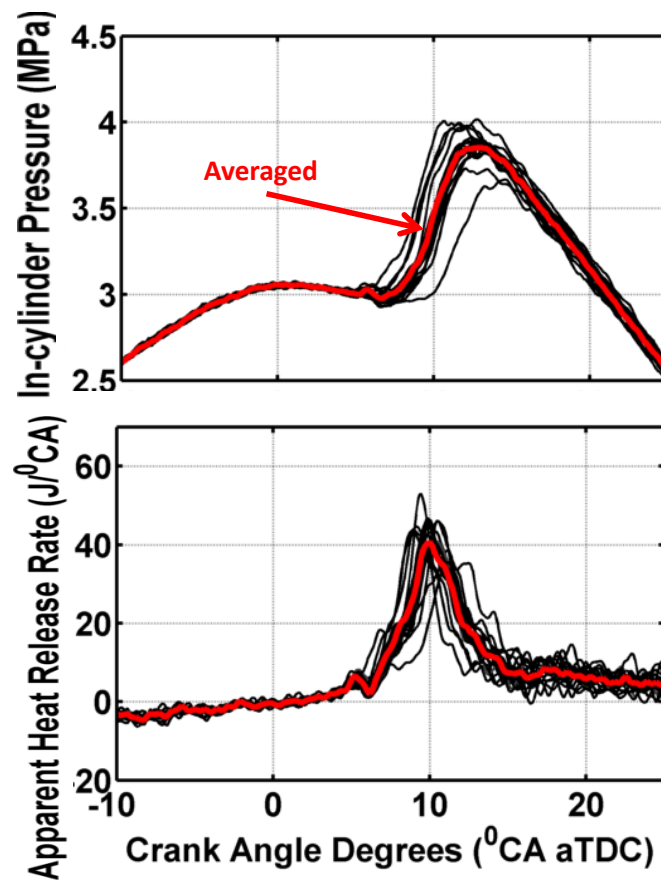


Figure 4.5 In-cylinder pressure traces of 20 instantaneous cycles (black lines) and their ensemble average (red line) at the 130-MPa injection pressure condition. Their corresponding apparent heat release rates are also shown at the bottom.

locations ranging from 6 to 8°CA aTDC and the peak in-cylinder pressure fluctuates between 3.7 and 4 MPa. However, in this study, these in-cylinder pressure variations are smaller than the differences caused by the variations in injection pressure, which will be later shown in the following chapters. The aHRR of individual cycles (black lines) and their cycle-averaged value (red line) are also shown at the bottom of Fig. 4.5, which also suggests a similar degree of cyclic variations to the pressure trace. Although the peak value fluctuates, it is noted that the sharp rise of aHRR at around 7°CA aTDC is very consistent among all the instantaneous cycles. Also, a small peak in aHRR is observed consistently at about 5°CA aTDC for all the cycles.

4.4.2. Cyclic variations in images

Variations in OH-PLIF images

First of all, OH-PLIF signals can contain an extra degree of cyclic variations due to fluctuations in the excitation laser sheet as well as the interferences of non-OH signals. However, the variation in the laser sheet is minor, and the interference signals or signal trapping will in fact reduce the degree of cyclic variations in the early OH-PLIF images during the fuel injection event because the signals from fuel-PLIF are more consistent. Despite this, the OH-PLIF data can potentially still carry significant cyclic variations as the turbulent nature of jet

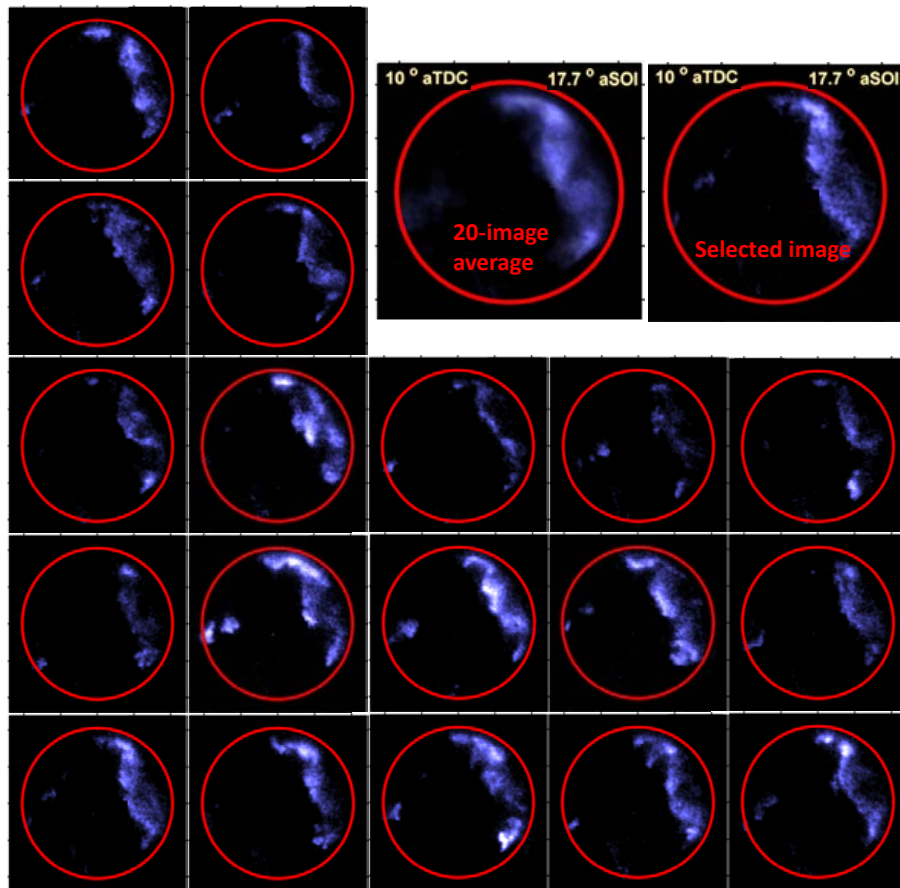


Figure 4.6 Individual “online” OH-PLIF images of all engine cycles captured at 10°CA aTDC at the 130-MPa injection pressure. The averaged image and selected individual image are shown at the top right.

development during diesel combustion will affect the flame structures directly, especially during the main combustion event where fuel-PLIF is much weaker. Figure 4.6 shows “on-line” OH-PLIF images from many different firing cycles as an example. The images were taken when a peak heat release rate was observed for the 130-MPa injection pressure condition, the same condition as in Fig. 4.5. This timing is in the middle of the main combustion event and therefore is most likely to be dominated by high-temperature reactions. Variations can be observed both in terms of intensity and spatial distributions; the bottom two rows have higher intensity and wider signal areas than other images.

An important issue associated with this high cyclic dispersion is that the average image shown at the top-right appeared to lose some key information from individual OH-PLIF images such as turbulent flame structures and high contrasts evident at the flame boundaries even though the general spatial distribution is well represented. The image is blurry and smeared out due to the cycle averaging of each pixel. To address this issue, a best-representing individual OH-PLIF image was selected for the interpretation purposes instead of the average image by applying a correlation-coefficient based method, similar to Refs. [13, 27, 78]. Specifically, a two-dimensional, normalised cross-correlation coefficient ($r_{2d,xy}$) was calculated for each set of images of a particular timing using:

$$r_{2d,xy} = \frac{\sum_i \sum_j (x_{i,j} - \bar{x})(y_{i,j} - \bar{y})}{\sqrt{\sum_i \sum_j (x_{i,j} - \bar{x})^2 \cdot \sum_i \sum_j (y_{i,j} - \bar{y})^2}} \quad (4.2)$$

where x is the ensemble-averaged image count, \bar{x} is the image mean of the ensemble-averaged image count, y is an image count of an instantaneous image, \bar{y} is the image value of the instantaneous image, and i and j denote the row and column pixel, respectively. The cross-correlation coefficient represents the degree of similarity between two images; the higher the coefficient, the more the resemblance. In the present study, a correlation between the average image and the individual ones was evaluated – the individual image that scores the highest was

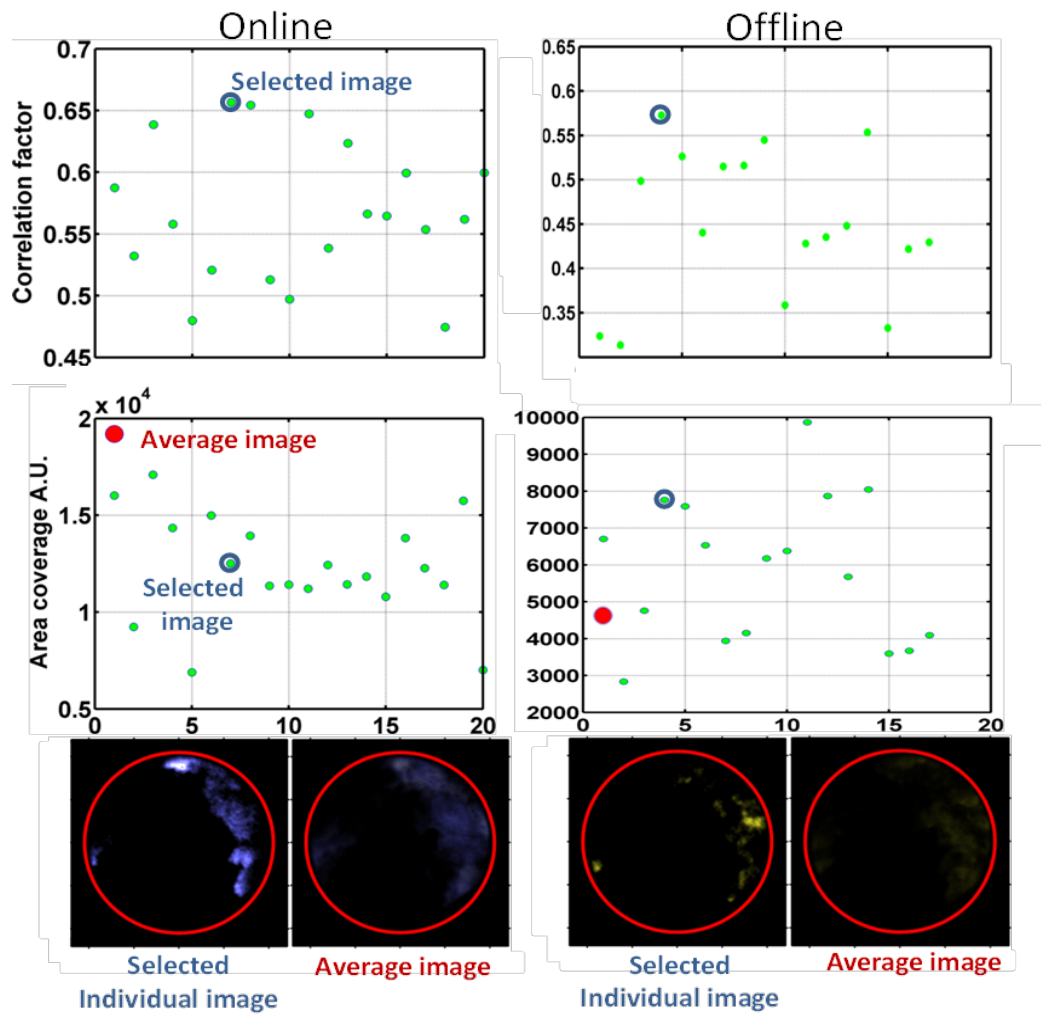


Figure 4.7 The correlation factors (top) and the area coverage of PLIF signal (middle) for all individual images captured at 13.5°C aTDC and 70 MPa injection pressure. Both online and offline images taken at 7 mm from the cylinder head are analysed. Shown at the bottom are a selected individual image for the highest correlation factor and the average of 20 images.

chosen. The selected image represents the overall diesel jet shape as the average image does while keeping turbulent structures on the flame boundaries.

An example is shown in Fig. 4.7: The correlation factors calculated for the images were plotted for both online and offline images. It is seen that the highest correlation factor for a given data set was 0.66 and 0.58 for the online and offline OH-PLIF images, respectively. On the bottom row, the selected individual image together with the average image of all 20 firing

cycles was presented. It is clear through visual evaluation and area coverage data that the selected individual image resembles the overall shape of the ensemble-averaged image while still maintaining the turbulent structure and spatial distributions of the diesel flame. This selection method also worked well regardless of the conditions as also seen in the selected image of Fig. 4.6. The same correlation factor-based selection method was applied not only for OH-PLIF images but also for fuel-PLIF and PLII images.

Variations in line-of-sight integrated images

Figures 4.8(a) and 4.8(b) display OH* and cool-flame chemiluminescence images from 19 selected individual cycles captured at 5° and 10°CA aTDC, respectively and at fixed injection pressure of 130 MPa. Also shown at the top right of each figure is the 20-image average and selected image using cross correlation. Among the individual images, the variations in the signal intensity and spatial distributions are noticeable in both cool-flame and OH* chemiluminescence. For instance, some cool-flame images show higher signal intensity on the up-swirl side (left-hand side) while others show the opposite trend (Fig. 4.8 (b)). Most of the OH* chemiluminescence images show comparable signal intensities between the up-swirl and down-swirl side of the jet but the images shown in the bottom row display the down-swirl signal only (Fig. 4.8(a)). Despite these cyclic dispersions, a majority of these images show a sharp resemblance to the overall structure of the average image, more so than OH-PLIF signals, likely because they are line-of-sight integrated. This is consistent with many studies using the averaged OH* images to understand overall diesel flame structures and to extract lift-off length information [7, 51, 58, 26]. Moreover, this suggests that the interpretation of OH* signal will not be influenced by the fact whether one uses an ensemble-averaged image or an individual instantaneous image. Therefore, for consistency, the same image selection method for OH-PLIF was applied for the presentation of cool-flame and OH* chemiluminescence images in the following chapters.

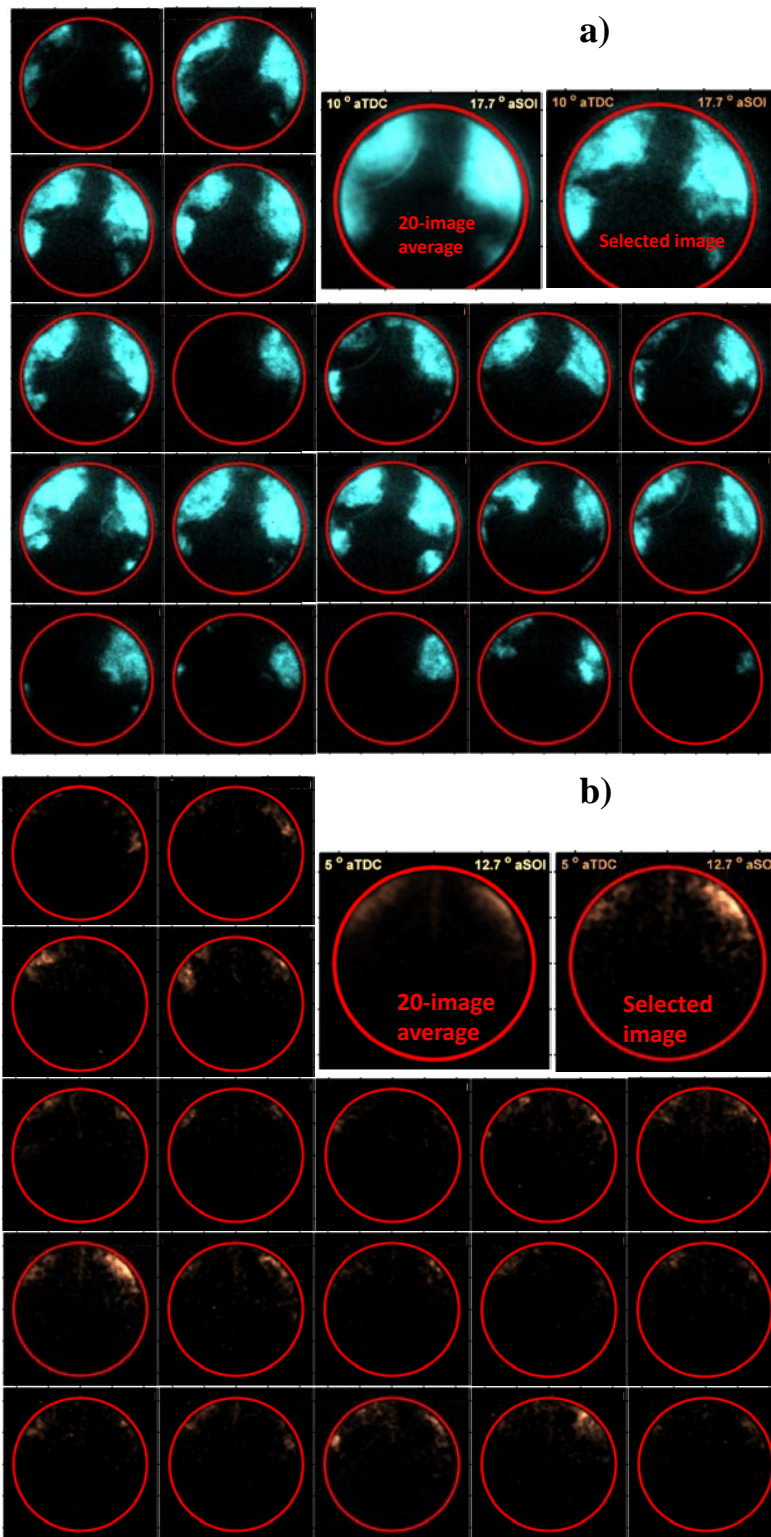


Figure 4.8. a) Individual OH* chemiluminescence images of 19 selected cycles captured at 10°CA aTDC at the 130-MPa injection pressure condition. Shown at the top right are the ensemble averaged image and the selected image. b) Individual cool-flame chemiluminescence images of 19 selected engine cycles captured at 5°CA aTDC at the 130-MPa injection pressure condition. The ensemble averaged image and the selected image are shown at the top right.

Chapter 5.

Development of a wall-interacting diesel jet

5.1. Experimental approach

To observe the evolution of a fuel jet under the strong influences of jet-wall interaction and swirl flow in a small-bore diesel engine, optical and laser-based imaging diagnostics were performed. The engine was operated at fixed operating conditions listed in Table 3.1 with selected injection conditions of 70 MPa injection pressure and long injection duration of 2.36 ms (Table 3.2). Piston type A and conventional ultra-low sulphur diesel fuel were used for this investigation. Both online (284.007 nm) and offline (283.875 nm) OH-PLIF images were obtained to detect and differentiate OH signals from interferences. Line-of-sight integrated imaging of cool flame and OH* chemiluminescence was also employed to provide complementary information to the planar OH-PLIF images. In addition, prior to the start of combustion when no OH signals were expected, captured PLIF images were used to discuss the liquid/vapour fuel penetration, given that the fuel fluorescence should be predominant signal. Pseudo-colouring schemes as listed in Table 4.2 and other image post-processing procedures were applied on all images for presentation and interpretation purposes.

5.1.1. Laser planes for planar laser diagnostics and nozzle selection

The OH-PLIF images were taken at various distances from the cylinder head. It has been determined that at -7.3°CA aTDC (or 7.3°CA bTDC), the fuel jet will impinge on the bowl wall at around 6.7 mm below the cylinder head. Therefore, three different laser planes at 5, 7 and 10 mm below the cylinder head were selected to cover the top, middle and bottom part of the fuel jet. Figure 5.1 (bottom left) depicts the location of these imaging planes with respect to the piston-bowl geometry of piston type A and the trajectory of the nominal jet. Also shown at the top of the figure is an illustration of the target jet relative to the laser coverage. To eliminate

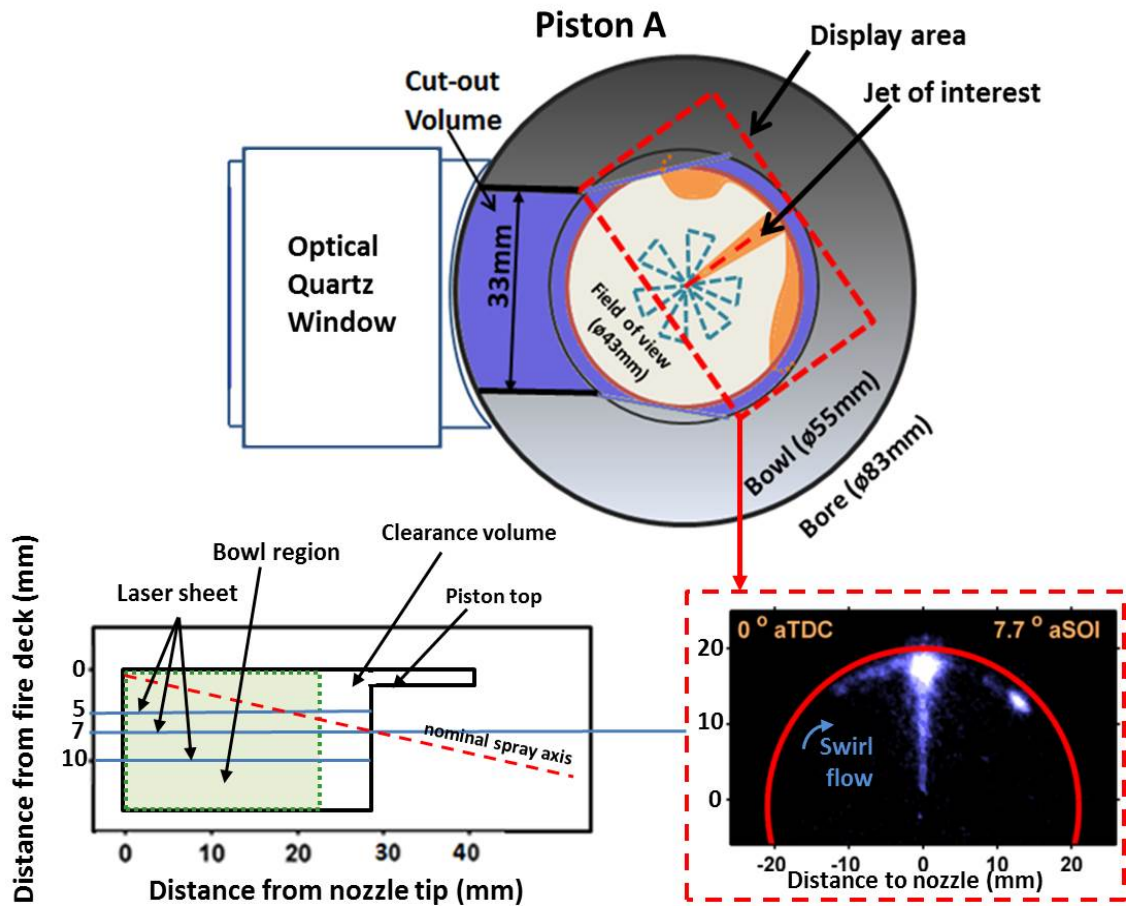


Figure 5.1 The laser beam path and area coverage (top), the field of view of PLIF imaging in r- θ plane (bottom-left), and illustration of the laser sheets for various distances from the cylinder head as well as the nominal spray axis and piston-bowl geometry in r-z plane (bottom-right).

possible impacts that the bowl-rim cut-out could have on the jet, the jet of interest was selected so that the fuel penetrated toward 2 o'clock position, away from the cut-out. The coverage of the laser sheet also suggest that visualisation of the target jet within the entire field-of-view is possible. While the piston quartz window doesn't allow for imaging of the region immediately on the piston-bowl wall, the effect of jet-wall interaction will still be prominent across the whole jet and can be observed with the jet development. The rectangle bounded by red dashed lines illustrates the region of interest that will be used in the following results and discussion section. An example image of fuel-PLIF at TDC taken at 7 mm is displayed on the bottom right of this figure. The captured image was rotated so that the jet axis would be at 12 o'clock.

5.1.2. *Online vs. offline OH-PLIF presentation*

For comparison purposes, the boundaries of the offline OH-PLIF signals were overlaid onto the corresponding online OH-PLIF image. An example of this arrangement is shown in the right image of Fig. 5.2. The images were taken at 13.5°CA aTDC where high-temperature reaction was predominant and thus OH radicals were expected. The offline OH-PLIF image on the left displays some signals near the piston-bowl wall at 3 and 8 o'clock directions, which is markedly

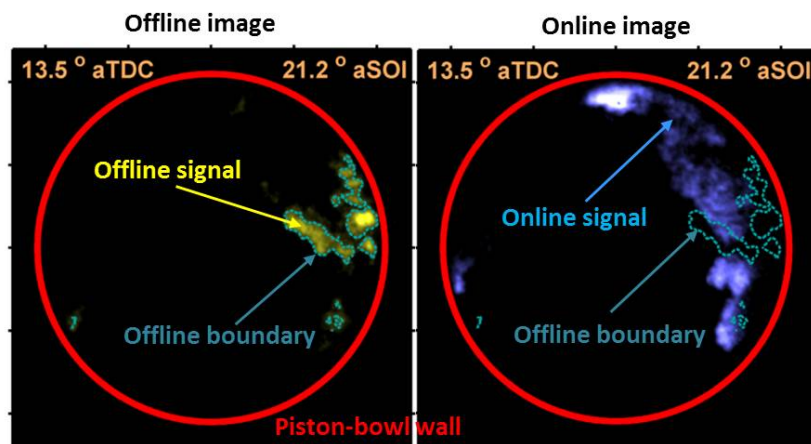


Figure 5.2 Post-processing of an offline OH-PLIF image for boundary detection (left) and the offline boundaries overlaid on the online OH-PLIF image (right) taken at the same 13.5°CA aTDC.

different from the online OH-PLIF signal in the image shown on the right. When the boundary has been plotted on top, it is evident that PLIF zones in the online signal are much larger than those of the offline image, suggesting that indeed the OH is predominant at the selected imaged crank angle location.

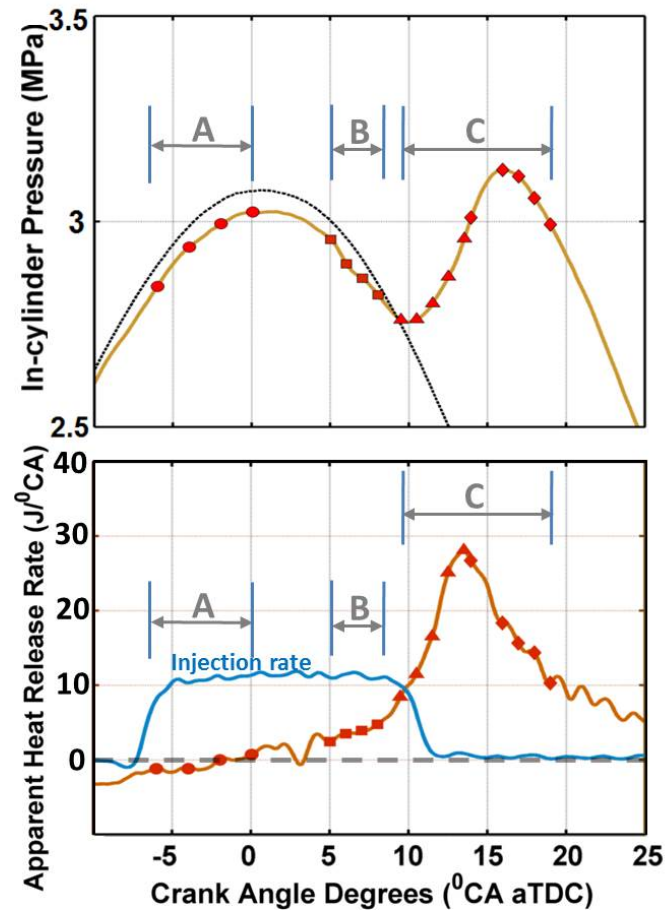


Figure 5.3 Average in-cylinder pressure trace for motoring (black dot line) and firing (brown solid line) cycles shown at the top and the apparent heat release rate (aHRR) trace at the bottom. Also shown is the measured fuel injection rate (blue solid line). To illustrate, symbols are provided on the pressure and aHRR traces for each image time for three combustion stages of this study, including liquid/vapour penetration (A: circles), low-temperature reaction (B: squares), high-temperature reaction I (C: triangles and diamonds).

5.2. In-cylinder pressure and apparent heat release rate

Fig. 5.3 shows the in-cylinder pressure traces for motoring and firing modes (top) and the apparent heat release rate together with the measured injection rate (bottom) for the condition of this investigation. Various symbols are drawn on the in-cylinder pressure and aHRR traces to illustrate the corresponding times to the images presented in the following sections, including circles for combustion stage A: liquid/vapour penetration, squares for combustion stage B: low-temperature reaction, and triangles and diamonds for combustion stage C: high-temperature reaction.

The in-cylinder pressure traces show that the fired pressure is lower than the motored pressure upon the start of fuel injection occurred at -7°CA aTDC (or 7°CA bTDC). This is due to the evaporative cooling of liquid diesel [4, 3, 93], which is also justified by the negative heat release rate. At this early stage (combustion stage A), the reaction does not occur but there are liquid and vapour-phase fuel penetrations, which can be visualised through fuel-PLIF imaging. As the entrainment of hot air into the fuel jet continued, the fuel-air mixture self-ignited [71], leading to a positive value in the apparent heat release rate. The heat release rate at this stage (combustion stage B) is very low with only a gradual rise, similar to a first-stage ignition process found in many low-temperature combustion (LTC) engine studies [12, 14, 38, 58]. As mentioned previously, the first-stage ignition induces weak signals from CH, CO and HCHO radicals. Therefore, cool flame chemiluminescence imaging has been performed for this combustion stage. The low heat release rate continues until 10°CA aTDC at which a steep rise of the heat release rate starts to occur due to the high temperature reactions of the second-stage ignition (combustion stage C). The fired pressure also exceeds the motored pressure at this crank angle. The high-temperature reactions at near stoichiometric mixtures normally result in very strong heat release as well as a high concentration of OH radicals, enabling OH-PLIF and OH* chemiluminescence imaging. In Fig. 5.3, it is noticeable that the fuel injection event occurs throughout the combustion stage B up to the early phases of combustion stage C,

creating a negative ignition dwell as typically found at high-load injection conditions. The peak heat release rate is observed at 13.5°CA aTDC, 2.5°CA after the end of injection, and then the apparent heat release rate starts to decrease, signalling the burning out of combustion products.

5.3. Combustion stage A: liquid/vapour penetration

Fig. 5.4 (left) shows the fuel-PLIF images taken at 7 mm below the cylinder head between -6°CA aTDC and TDC, corresponding to 1.7°CA and 7.7°CA after the start of injection (aSOI),

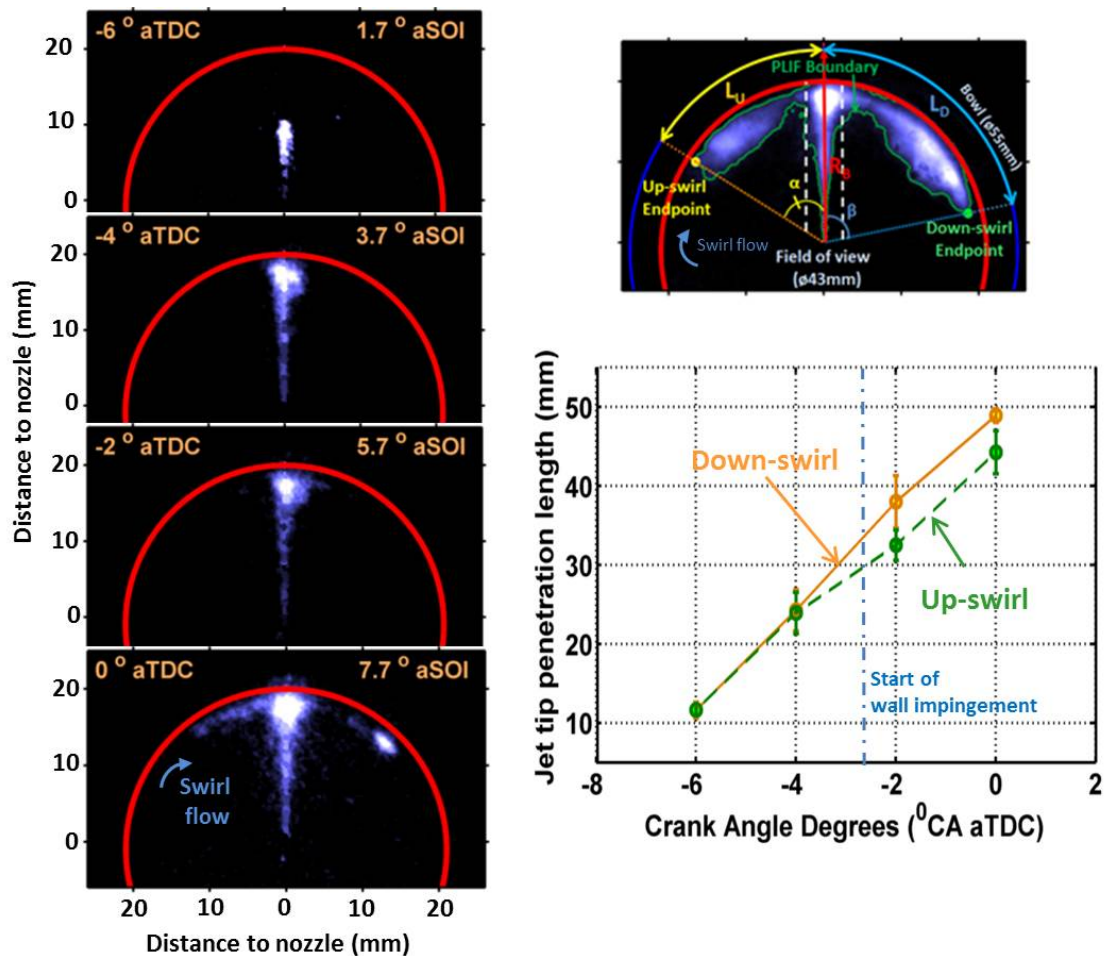


Figure 5.4 PLIF images of fuel fluorescence during combustion stage A: liquid/vapour penetration. Only online images are shown for the plane at 7 mm below the cylinder head due to non-reacting conditions (left). Shown on the top-right corner illustrates the estimation of the wall-jet tip penetration length. The results are shown in the bottom-right for both up-swirl and down-swirl sides of the diesel jet.

respectively. At this stage, there is no reaction as evidenced by the in-cylinder pressure and heat release rate (Fig. 5.3); therefore, only laser-induced fluorescence signals from diesel fuel should be expected. This non-reacting period provides a good opportunity to study a vaporising diesel jet before complex reactions take place.

In Fig. 5.4 (left), it is seen that a free diesel jet develops until -4°CA aTDC (or 4°CA bTDC) upon which jet-wall interactions starts to occur. In the imaging plane, the free jet is split into two: one half to the right and the other to the left; the penetrations occurs along the piston-bowl wall. Interestingly, the jet head on the right side shows a longer penetration length than that on the left side. This was due to the in-cylinder swirl flow that exists in the clock-wise direction in the field-of-view, meaning the left side of the jet penetrates against the swirl direction (i.e. up-swirl) whereas the right side of the jet travels in the same direction of the swirl flow (i.e. down-swirl).

To further investigate the wall-interacting jet penetration, the tip penetration lengths were derived from the fuel-PLIF images. A schematics explaining how the tip penetration was estimated is presented on the top-right corner of Fig. 5.4. As shown in the figure, the boundary of the fuel-PLIF region was first detected using an in-house developed MATLAB algorithm, and then used to select the end-points of each wall-jet. These points were then used to calculate the tip penetration length by adding the axial penetration length along the jet axis to the arc length between the jet axis and the wall-jet tip. The results are plotted in Fig. 5.4 (bottom-right). Since 20 fuel-PLIF images were used at each crank angle location, the mean value is presented together with the uncertainty error range of $1.96\sigma/\sqrt{n}$ [94]. The plot shows that the jet development during the free (no wall interaction) jet displays a linear increase in the tip penetration length, similar to Ref. [95-97]. As the jet impinges on the wall, however, the tip penetration lengths of the up-swirl and down-swirl jets shows a separation from shorter penetration for the up-swirl jet in comparison to the down-swirl jet. In fact, the down-swirl jet penetrates at similar rate to the free jet period but the up-swirl jet penetration appears to slow

down. This clearly demonstrates a strong influence of the swirl flow on the fuel penetration, particularly when the jet travels against the swirl flow direction. The swirl flow will also influence the fuel-air mixing such that the mixtures on the up-swirl side can be relatively leaner than that of the down-swirl jet, potentially leading to less intense reactions and lower heat release. In contrast to the significant impact on the development of the wall-jet, the swirl flow does not appear to affect the free-jet region near the nozzle. In the tested small-bore engine, the free-jet period is very short, meaning that the fuel jet develops mostly as a wall jet. The injection momentum is also very high, making it impossible for the swirl flow to impact the free-jet penetration.

5.4. Combustion stage B: low-temperature reaction

The apparent heat release rate shown in Fig. 5.3 suggests that reactions started from TDC. Since the low heat release rate in Fig. 5.3 resembles the first-stage, low-temperature ignition as in Refs. [12, 14, 78], cool flame chemiluminescence is expected in this stage. Therefore, direct imaging has been performed with no optical filters placed in front of the UV-enhanced lens, using cool-flame settings as per Table 4.1. Fig. 5.5 (left-most column) shows the cool flame chemiluminescence images taken between 5 and 8°CA aTDC, corresponding to 12.7 and 15.7°CA aSOI, respectively.

It is noted that the injection still continues at this combustion stage, as the end of injection occurred at 11.5°CA aTDC (see Fig. 5.3). During the experiments, there are no detectable cool flame signals at 5°CA aTDC, despite a positive heat release rate. This should be due to very weak signals that can not be captured for the given sensitivity of this optical setup. Fig. 5.5 shows that the first signal is observed at 5°CA aTDC when about 10 J/°CA of heat release rate is measured. Interestingly, this first signal is found in the wall-jet area, not in the free jet region. It is likely that the mixtures in the free jet region are too rich to be auto-ignited since the fuel is still being injected. In fact, this wall-jet ignition is very different from the free-jet ignition in a lifted jet flame that is often found in heavy-duty diesel engines [6, 12, 15]. Another interesting

observation is that the effect of swirl on low-temperature reaction is minimal with both up-swirl and down-swirl jets showing cool flame chemiluminescence in the wall-jet head region. This is in contrast with the shorter penetration length of the up-swirl jet (Fig. 5.4) due to the swirl flow, suggesting that variations in the degree of mixing due to swirl flow are not a predominant factor for the low-temperature reaction occurring in the pre-mixed charge. Previous studies [14, 40, 78] reported similar results that the distribution of HCHO, a good marker of low-temperature reaction, is not significantly affected by the mixture quality and swirl flow. The insensitivity to swirl-flow induced mixture fraction variations is also seen when low-temperature reaction (or cool flame) signals appears at the same timing on both down-swirl and up-swirl side of the jet. Noticeably, both sides of the wall-interacting jet shows the same cool flame intensity throughout the low-temperature reaction period. At 8°CA aTDC (the bottom row), however, the down-swirl side of the jet indicates stronger signals. This potentially suggests that the transition from first-stage, low-temperature ignition to second-stage, high-temperature ignition occurs on the down-swirl side of the jet first. Stronger down-swirl signals persists throughout the high-temperature reaction period as will be shown in the following section.

Fig. 5.5 (right) also shows offline and online OH-PLIF images taken at the same imaging time of the cool flame chemiluminescence images on the left. In each image, offline OH-PLIF boundaries were overlaid on a corresponding online OH-PLIF image. As in Fig. 5.4, these planar images were taken at 7 mm below the cylinder head. Since OH is a good marker of high-temperature reaction, PLIF signals from OH radicals are unlikely at this low-temperature reaction stage. Fig. 5.5 confirms it. The offline OH-PLIF boundaries overlaid on the online OH-PLIF images proves that the two signals are very similar. It is noticeable that the free jet region where no cool flame chemiluminescence signal is visualised shows PLIF signals in both offline and online OH-PLIF images. This suggests that the PLIF signals here includes strong fuel-PLIF, meaning online OH-PLIF images shown at the rightmost column also display fuel fluorescence signals. Together with the cool flame chemiluminescence images, the PLIF images exhibits the

continued fuel penetration along the bowl wall and the start of the low-temperature reaction in the wall-jet head region.

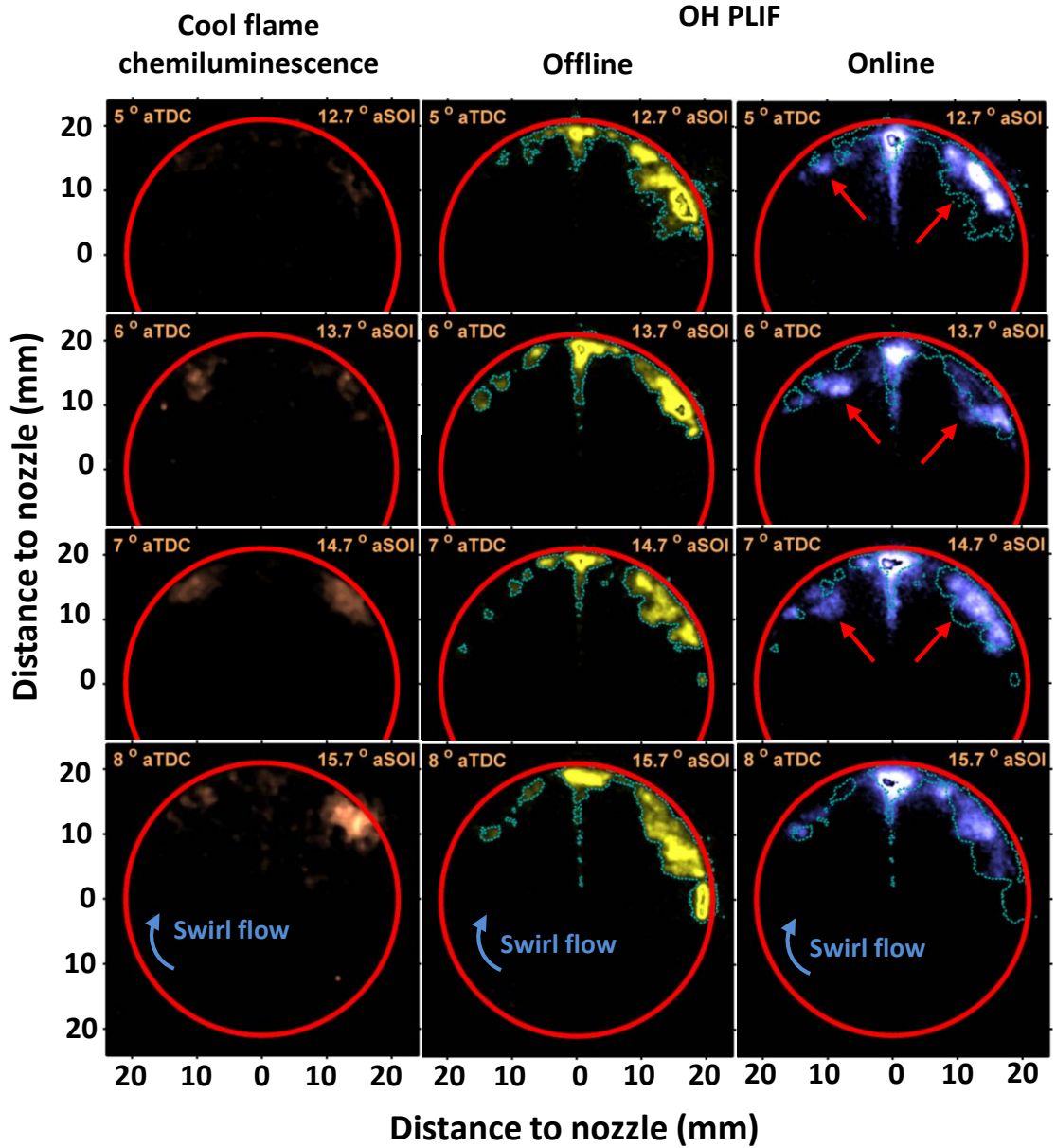


Figure 5.5 Cool flame chemiluminescence images (left), offline OH-PLIF images (middle) and online OH-PLIF images (right) during combustion stage B: low-temperature reaction. The PLIF images were taken at 7 mm below the cylinder head. The boundaries of offline images are overlaid on the online images for comparison purposes.

An interesting observation from Fig. 5.5 is an expansion of the PLIF signals at the wall-jet head (annotated by red arrows) in both the up-swirl and down-swirl jets. This is likely due to a turbulent ring-vortex forming at the jet head upon the impingement of the fuel jet on the bowl wall [18, 19]; potentially leading to locally enhanced mixing [18]. These head vortices have formed during the initial jet-wall interactions at the jet head region. As the injection continues, the vortices grow more in size rather than moving faster downstream. Therefore, the expansion observed in Fig. 5.5 does not move very far downstream but rather stays within the vicinity of its original location. When the injection ends, the absence of momentum stops the development of the vortices. This suggests the mixing has been improved right from the first appearance of the vortices and sustains throughout the injection period. It is noted that this expansion occurs at the same location as the cool flame chemiluminescence, suggesting the enhanced pre-combustion mixing at the initial jet head vortex to initiate the first auto-ignition in this region. Between the up-swirl and down-swirl wall jets, the stronger PLIF signals on the down-swirl side than on the up-swirl side is obvious, which can be explained by the relatively richer mixture as the fuel was transported by the swirl flow.

5.5. Combustion stage C: high-temperature reaction

Previous studies suggested that the transition from the first-stage, low-temperature ignition to the second stage, high-temperature ignition occurs as HCHO signals diminish and OH signals increase [14, 40, 41]. Fig. 5.6 shows OH* chemiluminescence (left), offline OH-PLIF (middle) and online OH-PLIF (right) images between 9.5 and 13.5°CA aTDC, corresponding to 17.2 and 21.2°CA aSOI, respectively. The end of injection occurs at 11.5°CA aTDC (or 19.2°CA aSOI). It should be noted that various optical filters and different capturing settings were used (see Chapter 4) for the OH* imaging which reduced the signal significantly. This means OH* signals shown in Fig. 5.6 are much stronger than unfiltered cool-flame chemiluminescence images in Fig. 5.5. As in Fig. 5.5, the offline OH-PLIF boundaries were overlaid on the online-PLIF images. In this combustion stage, a steep increase in the apparent heat release rate takes place

(see Fig. 5.3), suggesting the second-stage, high-temperature ignition. The OH* chemiluminescence in Fig. 5.6 is consistent with the apparent heat release rate trend such that the strong signals can be seen developing along the bowl wall. Interestingly, the OH* chemiluminescence appears to develop from the wall-jet head region where the cool flame chemiluminescence is also observed at earlier crank angle locations. The OH* chemiluminescence signals continues to grow and eventually at the end of injection (EOI), the signals observed move toward the wall impingement point, filling the space between the up-swirl and down-swirl jet heads. It is explained that, during the low-temperature reaction (Fig. 5.5), the mixtures near the wall impingement point and along the free jet region are too rich for the auto-ignition to occur. Upon the end of injection, however, some mixtures in these regions have got closer to the stoichiometry [98, 99] so that the high temperature reaction can be initiated. It is noticeable that the reaction zone does not expand towards the free jet region, likely due to overly lean mixtures formed after the end of injection [98, 99].

In the OH* images, earlier and more intense high-temperature reaction in the down-swirl jet than the up-swirl jet is obvious. For example, the OH* chemiluminescence of the down-swirl jet is seen at 9.5°CA aTDC at which the up-swirl jet shows no signals. Since the strain rate in the opposing fuel and air flows is higher than the parallel flows, the higher scalar dissipation rate is expected on the up-swirl side of the jet [100]. Therefore, the second-stage ignition of the up-swirl jet can occur later than the down-swirl jet [101]. It is consistent with the fact that the first appearance of the OH* chemiluminescence in the up-swirl jet occurs at 10.5°CA aTDC when the injection momentum and thus jet velocity starts to decrease. This can be explained that the reduced jet velocity (relative to the swirl velocity) decreases the dissipation rate, thereby inducing the second-stage ignition of the mixture. Moreover, the OH* in the down-swirl jet becomes stronger and larger than the up-swirl jet as the high-temperature reaction continues. The lower strain of the down-swirl jet than that of the up-swirl jet can also increase the OH* signal intensity while the relatively richer down-swirl jet mixtures owing to

the fuel being transported by the swirl flow can also lead to more intense high-temperature reaction.

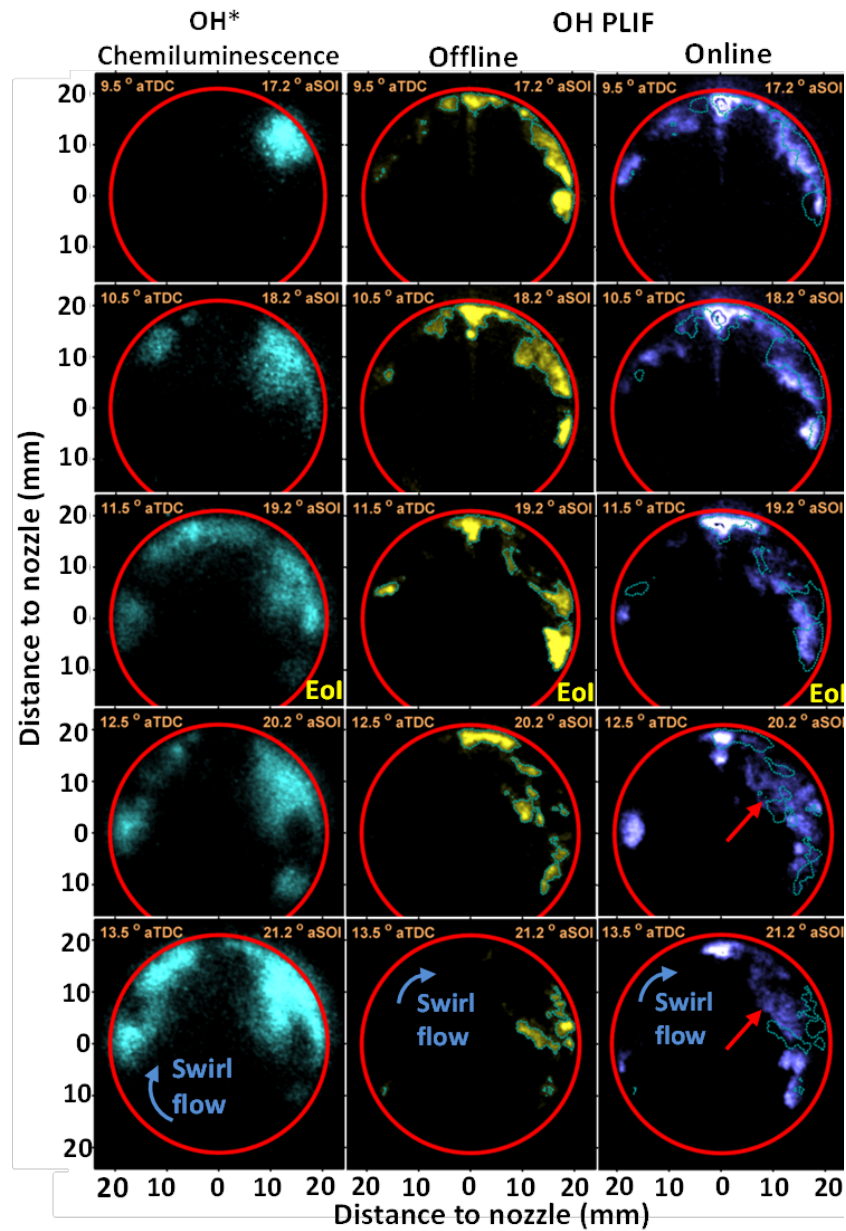


Figure 5.6 OH* chemiluminescence images (left), offline OH-PLIF images (middle) and online OH-PLIF images (right) during combustion stage C: high-temperature reaction between 9.5 and 13.5°CA aTDC when the apparent heat release rate increases. The PLIF images were taken at 7 mm below the cylinder head. The boundaries of offline images are overlaid on the online images for comparison purposes. The red arrows shown on the online images at 12.5 and 13.5°CA are to annotate the expansion of OH signals behind the jet head. EoI denotes the end of injection.

The OH-PLIF images shown next to the OH* chemiluminescence images also suggest the same findings of the first high-temperature reaction originating from the wall-jet head region and more intense reaction are found in the down-swirl jet. The image plane of 7 mm below the cylinder head is presented as in Figs. 5.4 and 5.5. The offline OH-PLIF images, primarily fuel fluorescence signals up to the end of injection, exhibit a temporal evolution of the fuel jet along the bowl wall. While the signal intensity on these images is similar to the PLIF signals during the cool flame period due to strong fuel-PLIF early on, it is seen that the offline signals become weaker with increasing crank angle degrees, particularly after the end of injection. For example, at 13.5°CA aTDC where the peak apparent heat release rate is observed, very weak offline OH-PLIF signals are shown in the up-swirl jet. Also the offline OH-PLIF signals appears first to be connected, forming a wall-jet structure (e.g. the first two images from the top). However, in the images at later crank angle locations, the signals are disconnected, forming many isolated fragments. This might suggest the transition of the offline signals from the fuel fluorescence to the reaction products such as soot precursors and soot pockets [13, 40, 71].

Similar to that of Fig. 5.5, the offline OH-PLIF boundaries were overlaid on the online OH-PLIF images as shown in the rightmost column of Fig. 5.6. The online OH images at 9.5°CA aTDC displays OH signals, larger than the offline boundaries on both the up- and down-swirl sides of the jet. Interestingly, the OH signals in the up-swirl jet are evident at this crank angle even though the OH* chemiluminescence image shows no signal. The cause for this mismatch is not entirely clear but it can be explained that in this early stage of high-temperature reaction, some OH radicals are formed during the cool flame reaction [14]. That is, the OH concentration from the first-stage ignition is sufficient to induce the laser-induced fluorescence signals, although the high-temperature reaction is not intense enough to emit OH* chemiluminescence signals. At 10.5°CA aTDC, the OH-PLIF images shows similar trends of the OH* chemiluminescence images with both OH-PLIF and OH* signals seen in the up-swirl jet. Also, the expansion of the down-swirl jet reaction zones in the OH* images is also visible in the OH-

PLIF images (annotated by red arrows). As mentioned previously, this wall-jet head region was positioned where a turbulent ring-vortex would likely form [18-20] and thus the enhanced mixing would lead to earlier and more intense second-stage ignition. From 11.5°CA aTDC, online OH-PLIF signals clearly outperforms the offline signals and are also seen near the wall impingement point, consistent with the OH* signals. Again, the OH-PLIF signals are not found in the free jet region, even after the end of injection. Later at 13.5°CA aTDC, the offline boundaries are surrounded by strong OH signals, possibly suggesting the soot oxidation due to the OH attack [14, 61].

While the online OH-PLIF signals in Fig. 5.6, together with the offline boundaries provides valuable information about the spatial and temporal development of the down-swirl jet, questions are raised about the up-swirl jet. Upon the end of injection, up-swirl signals are virtually non-existent with only small pocket of OH-PLIF seen at 20 mm from the nozzle in the radial direction. Since strong OH* signals are detected with the chemiluminescence images in the leftmost column, a long time after the cool flame reaction, this weak OH-PLIF signals are not expected. It could be because the OH-PLIF signals in other horizontal planes were not

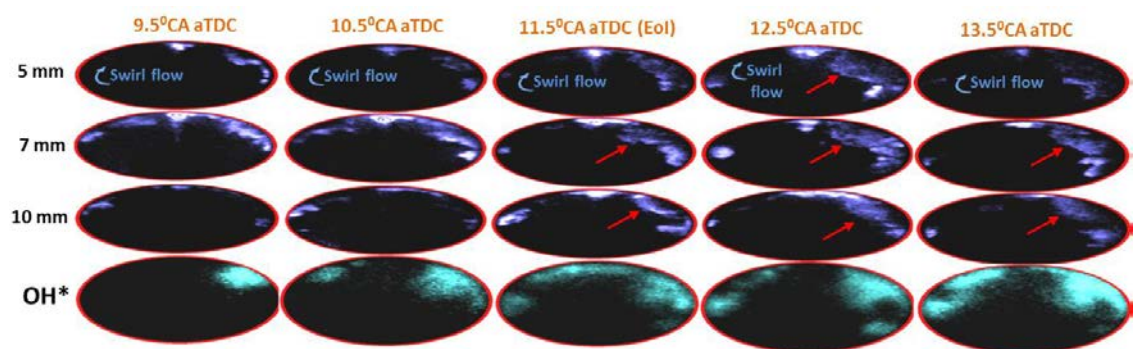


Figure 5.7 Online OH-PLIF images during combustion stage C: high-temperature reaction between 9.5 and 13.5°CA aTDC when the apparent heat release rate increases. The planar images are presented at various distances from the cylinder head. Shown at the bottom are line-of-sight integrated OH* chemiluminescence images (from Fig. 10). The red arrows point out the expansion of OH signals in the jet head region.

evaluated. Fig. 5.7 shows OH-PLIF images taken at three different image planes (5, 7, and 10 mm below the cylinder head). The OH* chemiluminescence images corresponding to the imaging crank angle locations of the OH-PLIF images are also presented at the bottom row. It is clearly seen when the OH-PLIF signals are integrated for the three planes, they do present on the up-swirl side of the jet. For example, at 11.5°CA aTDC, the top two planes show very weak OH-PLIF signals but the 10 mm plane displays a strong signal, which if integrated, are well reflected in the below OH* image. In addition, the expansion of the high-temperature reaction in the wall-jet head region (annotated by red arrows) is evident in all image planes, consistent with Fig. 5.6.

The apparent heat release rate in Fig. 5.3 suggests the decreased high-temperature reaction between 14 and 19°CA aTDC. At this stage, the high-temperature reaction signals are captured but there is no more fuel supply and thus the reaction slowly diminishes. How the diesel flame evolves at this stage is shown in Fig. 5.8. The online OH-PLIF images are presented for two different image planes of 7 and 10 mm below the cylinder head, similar to those of Fig. 5.7. The 5 mm plane was also attempted; however, the signal was very weak likely because the flames were transported by the downward movement of the piston. Fig. 5.8 shows that the OH signals appeared to be distributed widely compared to earlier crank angle locations. The OH signals continued to flow along the bowl wall and eventually become very weak by 19°CA aTDC. Later crank angle locations were also attempted but the signal was very minimal.

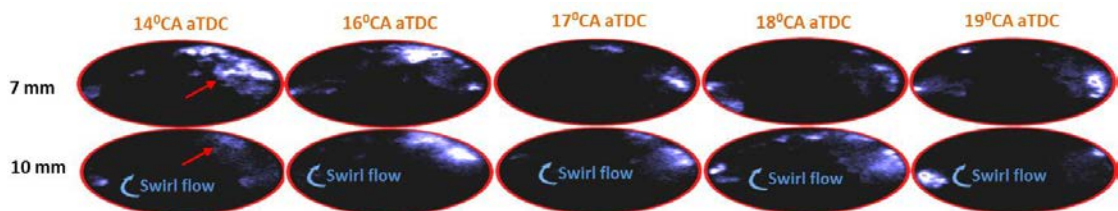


Figure 5.8 Online OH-PLIF images during combustion stage C: high-temperature reaction between 14 and 19 °CA aTDC when the apparatne heat release rate decreases. The planar images are shown at 7 and 10 mm below the cylinder head.

5.6. Summary

In this chapter, various optical/laser-based imaging diagnostics of OH-PLIF and fuel-PLIF as well as cool-flame and OH* chemiluminescence signals were performed in a small-bore optical diesel engine. The development of a reacting diesel jet under the strong influence of jet-wall interactions and swirl flow was clarified. The major findings from this chapter are summarised as follows:

- The low-temperature reaction of a wall-interacting diesel jet occurs in the jet head region where a turbulent ring-vortex is formed upon the jet impingement on the wall. The high-temperature reaction starts from the same wall-jet head region.
- During the premixed burn phase, the expansion of high-temperature reaction zone occurs in the same wall-jet head region of low-temperature reactions where the turbulent ring-vortex is expected.
- The swirl flow causes asymmetric jet structures such that the fuel penetration distance is longer on the down-swirl side than that on the up-swirl side. Moreover, the flame structures asymmetry is also found as the high-temperature reaction occurs earlier and is stronger on the down-swirl side of the jet due to the swirl-induced richer mixture.

Chapter 6.

The effect of injection pressure on the wall interacting jet

From the Chapter 5, it has been clear that further investigation of the turbulent ring-vortex created in the wall-jet head region is essential, especially at conditions where increased injection momentum might enhance the ring vortex. The engine operating conditions are as listed in Table 3.2 with fixed total fuel mass for various injection pressures. Therefore, this chapter presents images from similar optical/laser-based diagnostics as in Chapter 5 but with an emphasis on the influence of increased injection pressure on the wall-interacting jet development.

6.1. *Experimental approach*

From preliminary tests of high injection pressure conditions, laser beam attenuation was identified on the up-swirl side of the jet (i.e. the jet travelling against the swirl flow). This issue is illustrated in Fig. 6.1. Higher injection pressure is expected to result in longer penetration length with reaction occurring further downstream [102,103]. Therefore, the sooting flame penetrated along the wall and eventually the up-swirl jet was in the way of the incoming laser sheet, leading to the laser beam attenuation. This issue was unavoidable as a conventional diesel fuel with many added aromatic hydrocarbons was used, which are also known precursors for

soot formation. Both soot particles and aromatic hydrocarbons are well-known sources of strong interference and attenuation for the OH-PLIF signal. Therefore, the discussions about OH-PLIF images will be emphasised on the down-swirl side of the jet.

6.2. Variations in in-cylinder pressure and apparent heat release rate

Shown at the top of Fig. 6.2 are the in-cylinder pressure traces for motoring and firing cycles. The motoring cycle is plotted using a black dashed line while green, blue, and red solid lines are used for firing cycles at 70, 100, and 130 MPa injection pressure conditions, respectively. The corresponding aHRR and measured injection rate are shown at the bottom of Fig. 6.2. It is clearly seen that all the fired pressures are lower than the motored pressure upon the start of fuel injection at 7°CA bTDC which is due to the same evaporative cooling effect of liquid-phase diesel fuel previously observed at 70 MPa condition. During this period, no signals

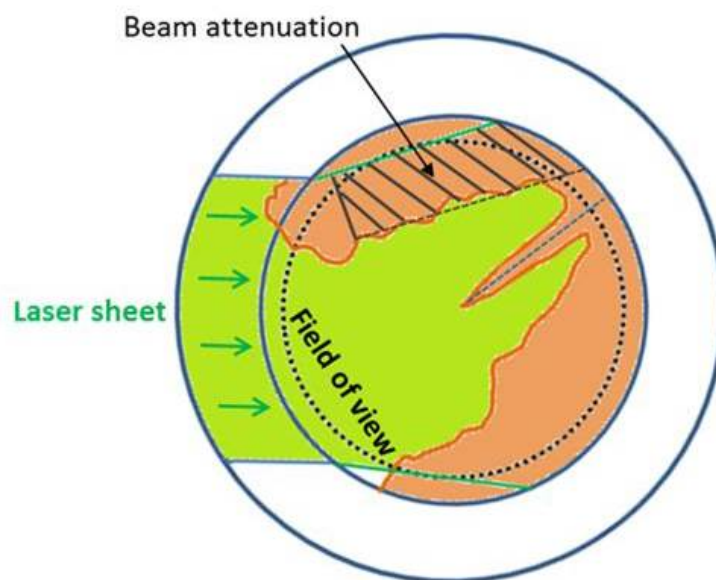


Figure 6.1 Laser attenuation issue at higher injection pressure

are expected from cool-flame or OH* chemiluminescence.

The start of second-stage ignition appears to occur during the decreasing phase of the injection rate for all injection pressures, right before the end of injection. As the injection duration is shorter for higher injection pressure, the start of combustion occurs at an earlier crank angle. The earlier start of high-temperature reaction for higher injection pressure is indeed expected because the increased jet momentum will cause higher air entrainment and thus better

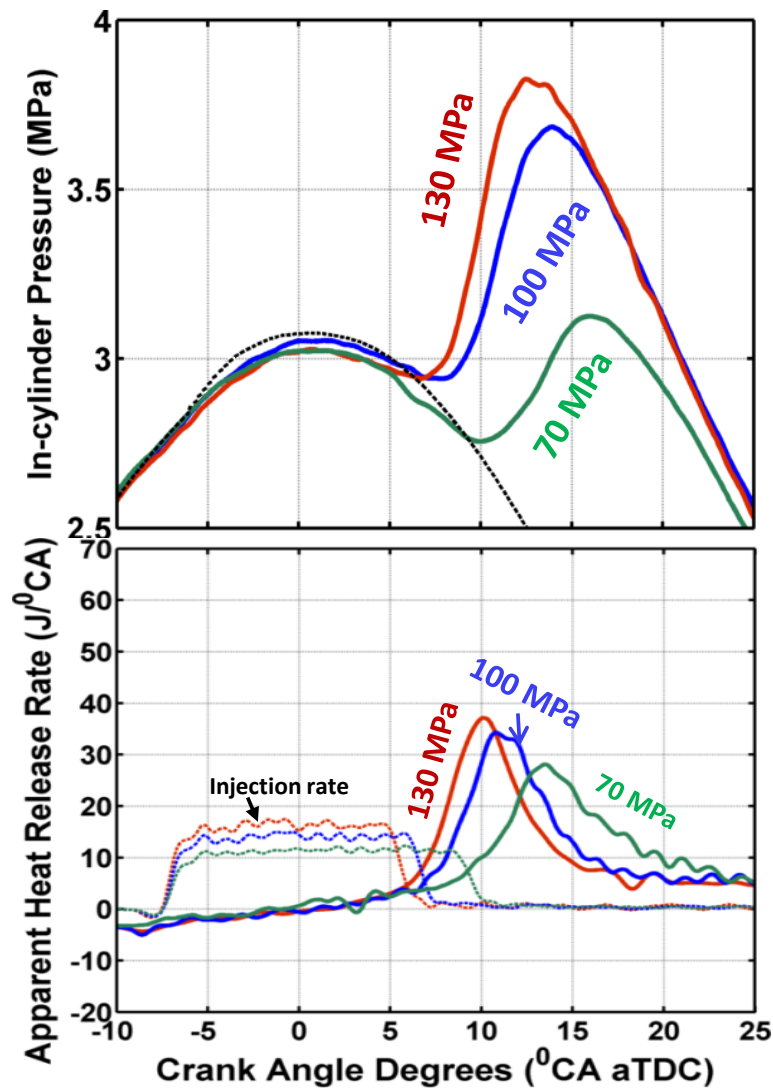


Figure 6.2 Average in-cylinder pressure traces (top) and apparent heat release rates (bottom) for various injection pressures. Also shown at the bottom is the injection rate profiles measured using a Bosch-tube-type injection rate meter.

mixing for a fixed injection mass, which is consistent with the previous studies reporting the decreased ignition delay with increasing injection pressure [47, 96, 103, 104].

Not only the timing but also the magnitude of in-cylinder pressure is affected by the injection pressure. Figure 6.2, for example, shows that higher injection pressure results in higher in-cylinder pressure at any fixed crank angle location. In fact, this is due to the enhanced mixing leading to the faster burning. For higher injection pressure conditions, the aHRR increases more rapidly and declines at a higher rate, suggesting shorter burn duration. The decreased burn duration results in a higher rate of heat release and increased flame temperature, leading to the increased in-cylinder pressure [105]. The faster burning also affects heat loss characteristics. With increasing injection pressure, the shorter burn duration will lead to increased reacting gas temperature, which then will increase the heat loss; however, the faster burning would also limit the time for heat loss between reacting gases and the cylinder walls [106]. The latter should be the case for the higher in-cylinder pressure seen in Fig. 6.2.

6.3. Fuel jet penetration at higher injection pressures

Figure 6.3 (top) shows fuel-PLIF images taken at 7 mm below the cylinder head between -6°CA aTDC (or 6°CA bTDC) and TDC for the 130-MPa injection pressure. At these crank angles, the in-cylinder pressure and aHRR suggest that an evaporative cooling process occurs well before the commencement of low- and high-temperature reactions (Fig.6.2). Therefore, it is expected that the laser-induced fluorescence signals come solely from fuel (i.e. fuel-PLIF). This non-reacting period is useful to study the penetrations of a vaporising diesel jet for various injection pressures. Fuel-PLIF images in Fig. 6.3 (top) show that the diesel jet also impinges on the bowl wall shortly after the start of injection. As a result, a wall-interacting diesel jet is formed with some portion of the jet travelling against the swirl flow (clock-wise rotation in the field of view) and the rest penetrating in the same direction.

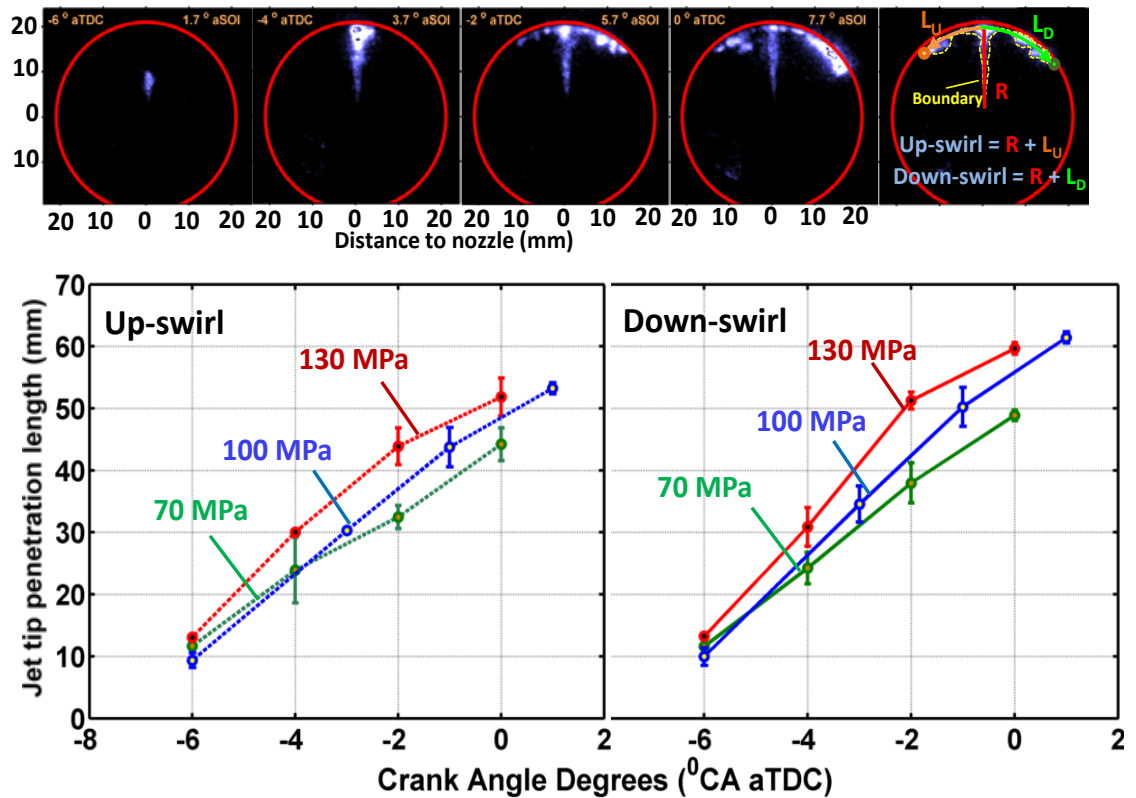


Figure 6.3 Example fuel-PLIF images at 7mm below the cylinder head for the 130-MPa injection pressure condition and the illustration of the penetration length measurement (top). Shown at the bottom are the jet tip penetration lengths on the up-swirl side (left) and down-swirl side (right) of the jet for various injection pressures.

The tip penetration length of vaporising diesel jets for higher injection pressures of this study (100 and 130 MPa) was also calculated using the fuel-PLIF images with the same method described in Chapter 5. Mean values and the uncertainties of $1.96\sigma\sqrt{n}$ are plotted in Fig. 6.3 (bottom) for all injection pressures tested in the present study and for both up-swirl and down-swirl side of the jet. As expected, the figure shows that the jet tip penetration length increases with increasing injection pressure in both up-swirl and down-swirl jet due to the increased injection momentum. Therefore, fuel-air mixing should be enhanced for higher injection pressure conditions considering the injected fuel mass is fixed. It is also noticeable that the jet tip penetration length on the down-swirl side is longer than that on the up-swirl side regardless

of the injection pressure, indicating that the swirl-induced jet asymmetry exists even at higher injection momentum.

6.4. Low-temperature reaction for various injection pressures

The cool-flame chemiluminescence imaging was performed for various injection pressure conditions. Figure 6.4 shows these captured cool-flame chemiluminescence images. It should be noted that the cool-flame chemiluminescence was extremely weak when the signal was first

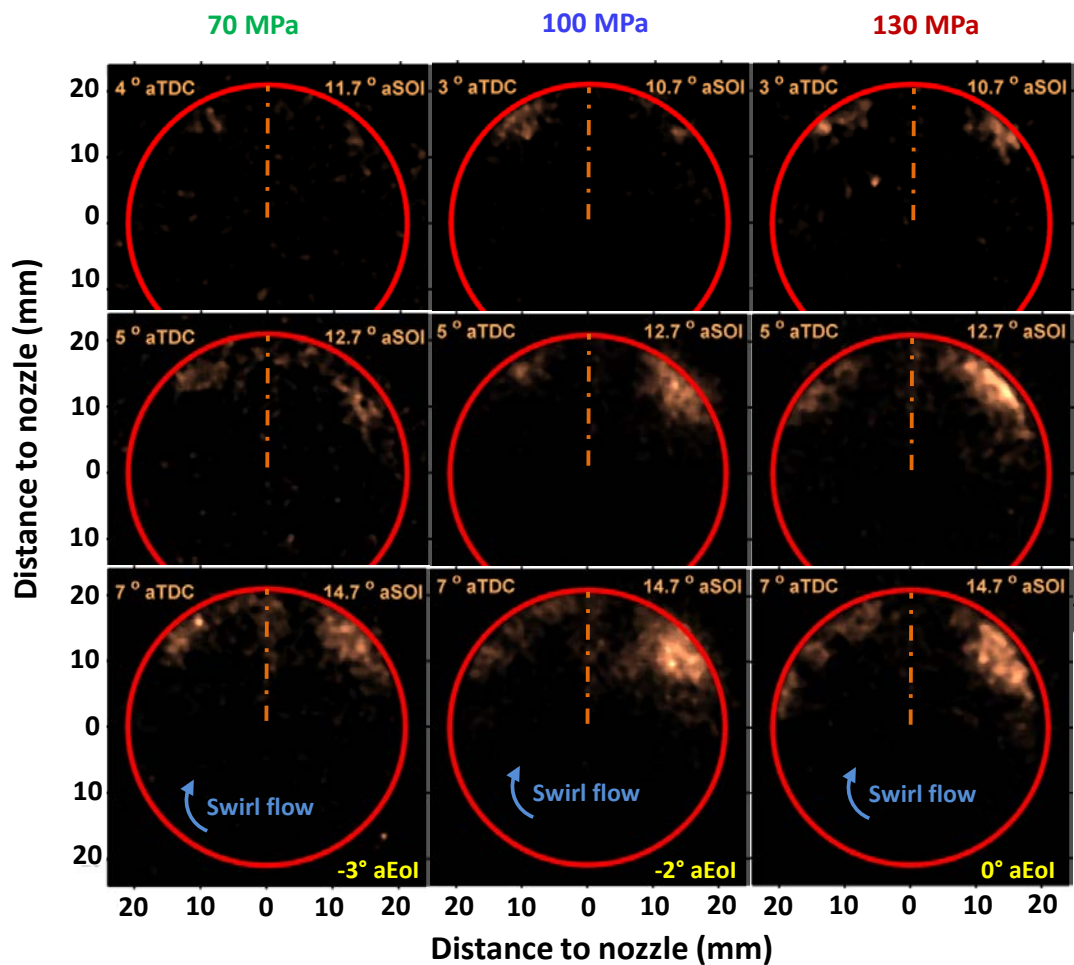


Figure 6.4 Natural “cool-flame” chemiluminescence images during the low-temperature reaction period for various injection pressures. A jet axis is drawn in each figure to denote the continuing fuel injection.

detected at around 3~4°CA aTDC for all injection pressures tested in the present study. Imaging at earlier crank angle locations was again attempted considering a positive value of the aHRRs (see Fig. 6.2); however, still no signal was found for given optical settings.

In Fig. 6.4, vertical dashed-dot lines are also drawn on each image to denote the fuel jet axis. It is noticeable that the cool-flame signals are originated from the wall-jet head region regardless of the injection pressure. The results in Chapter 5 suggested that a likely cause for the observed trend was locally enhanced mixing in the wall-jet head region due to a turbulent ring-vortex formed during jet-wall interactions. The same explanation is also applicable for higher injection pressure conditions. A general trend in Fig. 6.4 is that the intensity of cool-flame chemiluminescence increases with increasing injection pressure. It is conceivable that the higher intensity of cool-flame is caused by the enhanced head vortex due to the increased injection momentum [18]. Furthermore, as the cool-flame reaction starts at approximately the same time across all injection pressures, the higher amount of fuel presents at higher injection pressure conditions before this start of reaction causes enhanced decomposition of KHP molecules, thereby increasing the cool-flame chemiluminescence. Also, the signals are found in larger areas for higher injection pressure conditions, which is consistent with the increased vapour penetration length (Fig. 6.3). It should be noted, however, that the variations in the cool-flame chemiluminescence signals do not make a significant impact on the in-cylinder conditions. As observed in Fig. 6.2, negligible variations are found in the aHRRs between all injection pressure conditions of the present study. A cause for this discrepancy is not entirely clear but it can be explained that the minor heat energy released by cool flames will not stand out in a bulk-gas phenomenon.

An interesting trend in Fig. 6.4 is that the signal difference between the up-swirl and down-swirl jet becomes higher as the injection pressure increases. As observed in Chapter 5, the cool-flame signals from the 70-MPa injection condition suggested that the first-stage ignition was not sensitive to the mixture variations caused by the swirl flow. However, as the injection pressure

increases to 100 and 130 MPa, it is noticeable that both the intensity and spatial distribution of cool-flame chemiluminescence are much higher in the down-swirl jet. This can actually be explained by relatively richer mixtures as well as lower scalar dissipation rates on the down-swirl side as the fuel jet penetrates in the same direction of the swirl flow. This difference must also exist at the 70 MPa injection case, however, it was not eminent because the overall intensity of the low-temperature reaction was low.

Figure 6.5 shows the online OH-PLIF images with overlaid offline signal boundaries for all

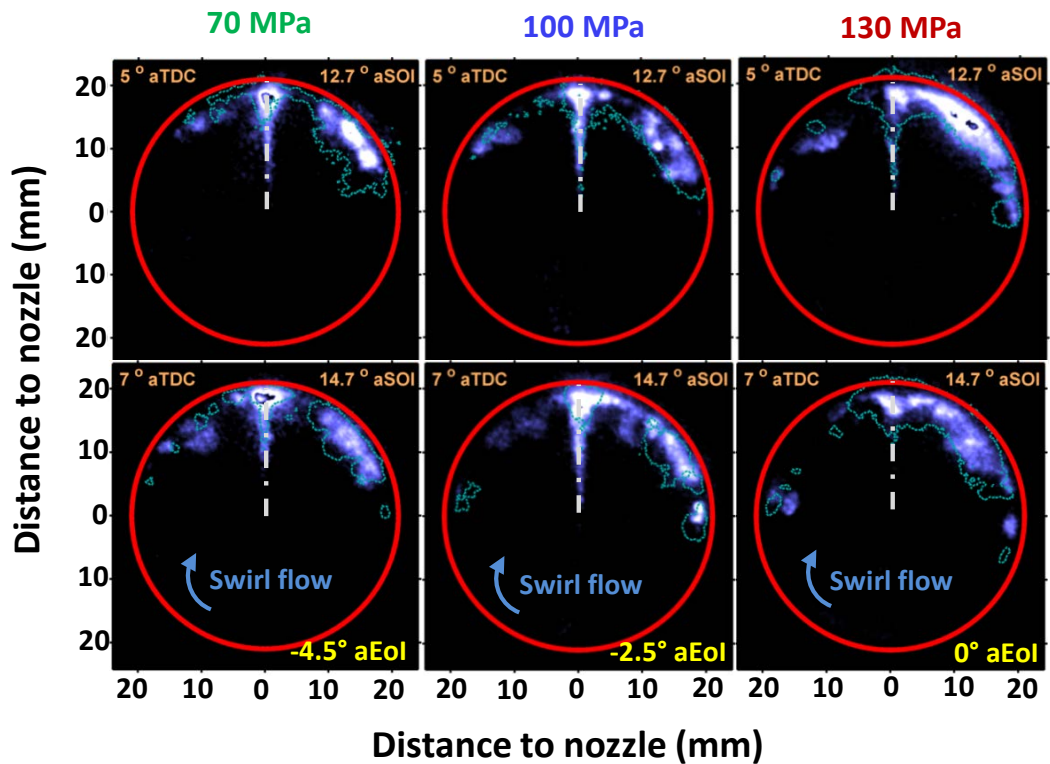


Figure 6.5 Offline OH-PLIF boundaries overlaid on online OH-PLIF images during the low-temperature reaction period for various injection pressures. The planar images were obtained at 7 mm below the cylinder head. Similar to Figure 10, a jet axis is drawn on each image to denote the continuing fuel injection.

injection pressures tested in the present study. The images are shown for 5°CA and 7°CA aTDC where strong signals from cool-flame chemiluminescence are observed for high injection pressure (Fig. 6.4). The images show that online OH-PLIF signals are still very similar to the offline OH-PLIF boundaries in all conditions despite the fact that the images were taken from different engine cycles. As the injection continues at these crank angle locations (see the injection rate in Fig. 6.2) and online and offline OH-PLIF signals are evident along the jet axis, both PLIF signals should be mostly from fuel fluorescence.

6.5. High-temperature reaction at various injection pressures

Figure 6.6 shows the temporal and spatial development of OH* chemiluminescence during the main combustion event for all injection pressures. Also drawn on some images in this figure is a jet-axis denoting when the injection still takes place. For the 70-MPa injection, the end of injection occurs near the peak aHRR timing whereas the injection ends 1.5°CA and 3°CA before the peak aHRR timing for the 100-MPa and 130-MPa conditions, respectively. As mentioned previously, the earlier end of injection results in the increased pre-combustion mixing and thus higher rate of heat release. This is consistent with the increased OH* chemiluminescence signals observed at higher injection pressures. Not only the OH* intensity but also the OH* areas grow with increasing injection pressure. The imaging was performed at every crank angle locations (or half crank angle if needed) and various numbers of OH* images were selected depending on the injection pressure condition. In Fig. 6.6, three images are presented before the peak aHRR timing for the 70-MPa injection case. Due to the faster burning at higher injection pressure conditions, only two and one images are presented before the peak aHRR timing for the 100-MPa and 130-MPa conditions, respectively. When the images taken at 9°CA aTDC (the top row) are compared, the OH* signals show further developed structures at higher injection pressures confirming the faster burning rate. For the 100-MPa and 130-MPa injection conditions, the first evidence of OH* signals (very weak and not shown in Fig. 6.6) are detected at 8.5°CA and 7.5°CA aTDC, 0.5 and 1.5°CA earlier than the 70-MPa injection case,

respectively. This indicates that the high-temperature reaction starts to occur earlier and becomes stronger at higher injection pressure conditions, which can be explained by the enhanced mixing. The OH* chemiluminescence images in Fig. 6.6 show the same trend for other injection pressures tested in this investigation. For example, the first OH* signals are not observed in the free jet or the jet-wall impingement region but at the jet head where cool-flame chemiluminescence signals grow gradually (Fig. 6.4) for any fixed injection pressure conditions. Also, the expansion of OH* signals in the wall-jet head region (denoted by red arrows) is evident particularly at the peak aHRR timing regardless of the injection pressure. Furthermore, the OH* chemiluminescence appears on the down-swirl side first and then grows more rapidly than the up-swirl side of the jet for all injection pressures tested.

When the images at the peak aHRR timing are compared, it is clearly seen that the OH* signals in the down-swirl jet expands more at higher injection pressure conditions (red arrows aiming at the right side of the jet). The growth of OH* signals also occurs at a higher rate which explains the steeper increase of the aHRR at higher injection rate (Fig. 6.2). A significant difference is also found on the up-swirl side of the jet. For the 70-MPa injection pressure, the up-swirl OH* signal is weaker and the coverage area is smaller than that of the down-swirl signal due to relatively locally leaner mixtures and higher dissipation rate [100, 101]. However, at higher injection pressure conditions, the up-swirl signal increases and eventually becomes comparable to its down-swirl counterpart. This should be the result of the increased injection momentum that overcomes the swirl flow, forming relatively richer mixtures on the up-swirl side. Nevertheless, the asymmetry caused by the swirl flow is still found on the up-swirl jet development. Figure 6.6 shows that the expansion of OH* signals on the up-swirl side appears closer to the jet axis (red arrows aiming at the left side of the jet) than that on the down-swirl side, which was found earlier for 70 MPa condition but now is also noticeable at 100 and 130 MPa, the cause for this can be that the initial formation of a turbulent ring-vortex occurred closer to the jet axis due to the counter-acting swirl flow.

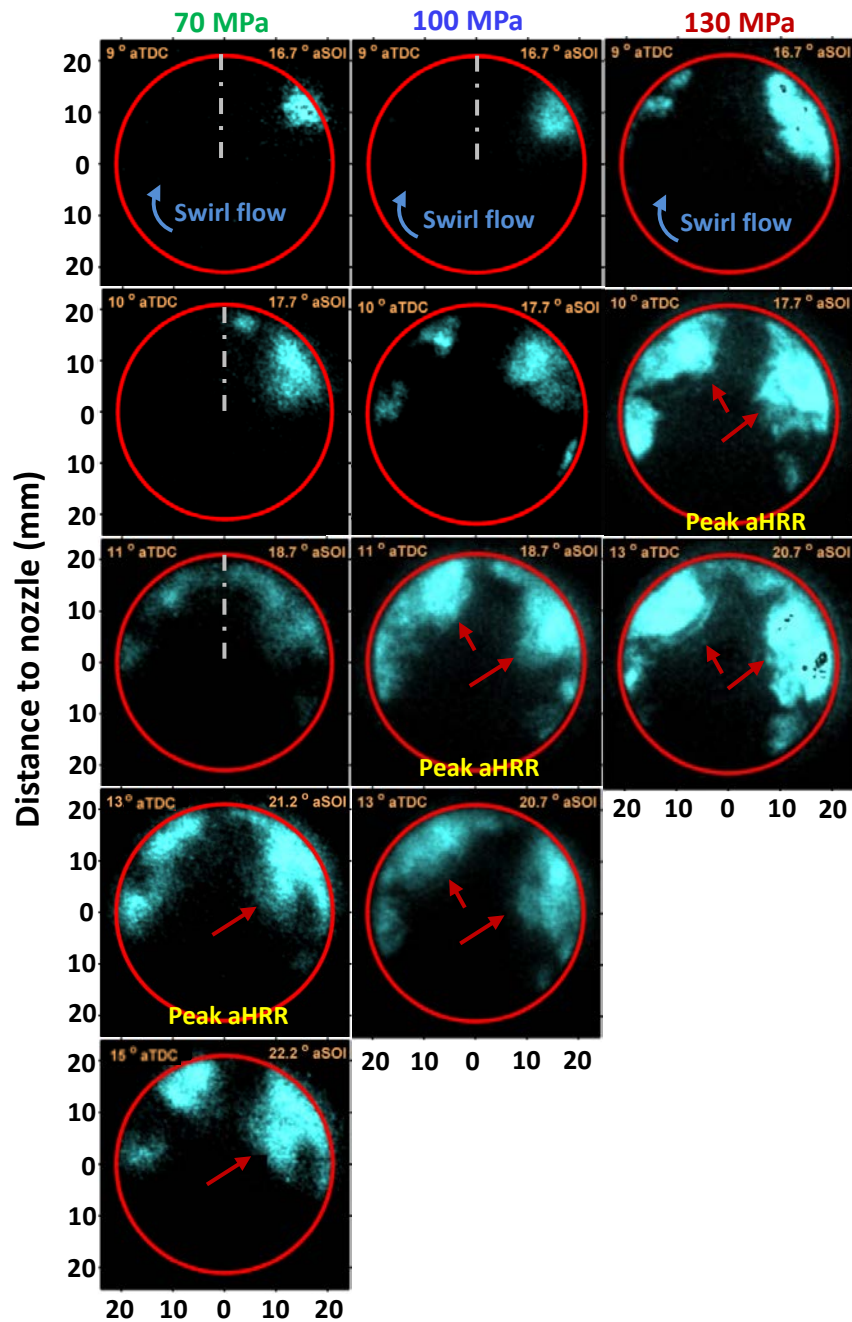


Figure 6.6 OH* chemiluminescence images during the high-temperature reaction period for various injection pressures. A jet axis is drawn jet in some images to denote the continuing fuel injection. The swirl flow rotates in the clock-wise direction as illustrated at the top images. The red arrows point out the expansion of OH* zones occurring in the wall-jet head region. As annotated, the images corresponding to the peak apparent heat release rate are 13, 11, and 10°CA aTDC for 70, 100, and 130 MPa injection pressure conditions, respectively.

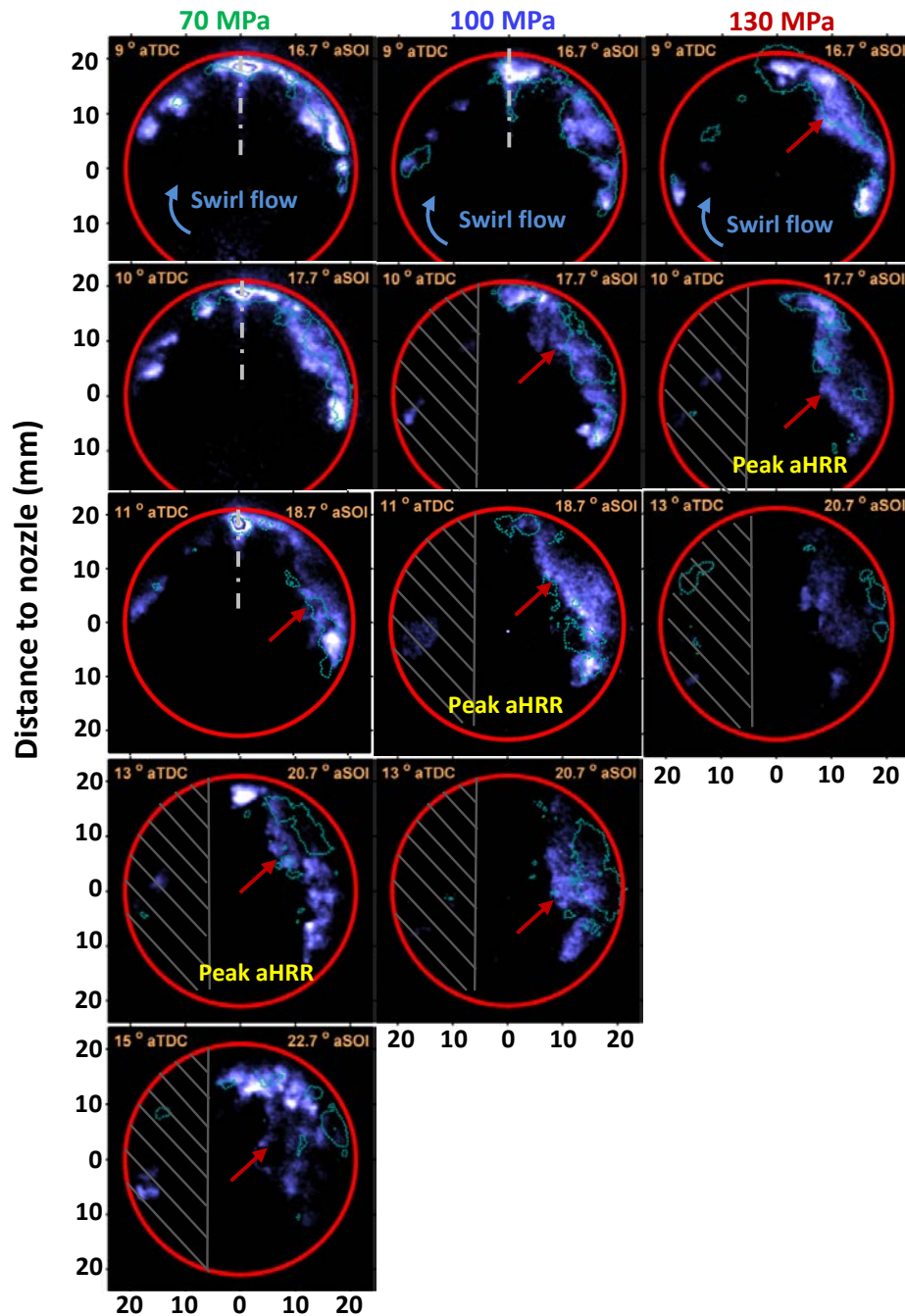


Figure 6.7 Offline OH-PLIF boundaries overlaid on online OH-PLIF images during the high-temperature reaction period as of Figure 12 for various injection pressures. The planar images were obtained at 7 mm below the cylinder head. The red arrows indicate the expansion of OH-PLIF signals occurring in the wall-jet head region. As annotated, the images corresponding to the peak apparent heat release rate are 13, 11, and 10°CA aTDC for 70, 100, and 130 MPa injection pressure conditions, respectively.

For the same crank angle locations and injection pressures conditions of Fig. 6.6, Fig. 6.7 shows offline PLIF signal boundaries overlaid on the online OH-PLIF images. The laser sheet was inserted horizontally at 7 mm below the cylinder head. As mentioned previously, the beam attenuation due to high sooting gases was problematic. The region of high attenuation issues are covered with grey lines to avoid the misinterpretation of signals observed in the region. Although the online and offline OH-PLIF images were taken from different engine cycles, the use of the correlation factor-based method to select an individual representative image is still very effective in obtaining the offline signal boundaries that well represent the general behaviour of interference signals with respect to the online OH-PLIF signals at high injection pressure conditions.

A first noticeable trend in Fig. 6.7 is that the offline signals are much weaker and appear as scattered pocket-like structures within the OH-PLIF signals (except 9 and 10°CA aTDC for the 70-MPa injection case when there was still ongoing fuel injection). These offline signals are most likely soot incandescence, indicating the soot pockets surrounded by OH radicals during the oxidation process. The OH-PLIF images support the finding about the expansion of high-temperature reaction zone from the OH* chemiluminescence images. That is, the expansion of the OH-PLIF signals is observed in the wall-jet head region where a turbulent ring-vortex formation is expected (highlighted by red arrows). This expansion becomes more evident at higher injection pressure conditions. For example, at the peak aHRR timing, the OH-PLIF signals appear as thick flame boundaries with highly curved structures for the 130-MPa injection case. This is markedly different from spread-out distributions of OH-PLIF signals at lower injection pressure conditions. Another interesting trend that is only observed in the OH-PLIF images is that the expansion of the high-temperature reaction zone appears to gradually move further downstream for higher injection pressure. This is simply due to longer penetration and higher momentum of the jet at higher injection pressure conditions. However, this is not evident in the OH* chemiluminescence images (Fig. 6.6), likely due to the line-of-sight

integrated nature of the signals; only when a thin layer of the flame is visualised, the shift of the expansion zone becomes clearer.

The OH-PLIF images taken at three different horizontal planes of 5, 7 and 10 mm below the cylinder head are shown in Fig. 6.8 using three-dimensional configurations. For presentations purposes, the offline boundaries are not overlaid and only two crank angle locations from each injection pressure data are presented. These images are divided into two groups: one for those obtained before the peak aHRR and the other at the peak aHRR timing. The crank angle location is shown at the top of each image. The up-swirl signal should be ignored in Fig. 6.8 due to the beam attenuation issue. A first noticeable trend from the OH-PLIF images is that the expansion of the high-temperature reaction in the wall-jet head region occurs in all three planes (annotated by red arrows) with increased expansion and distance away from the jet-axis for

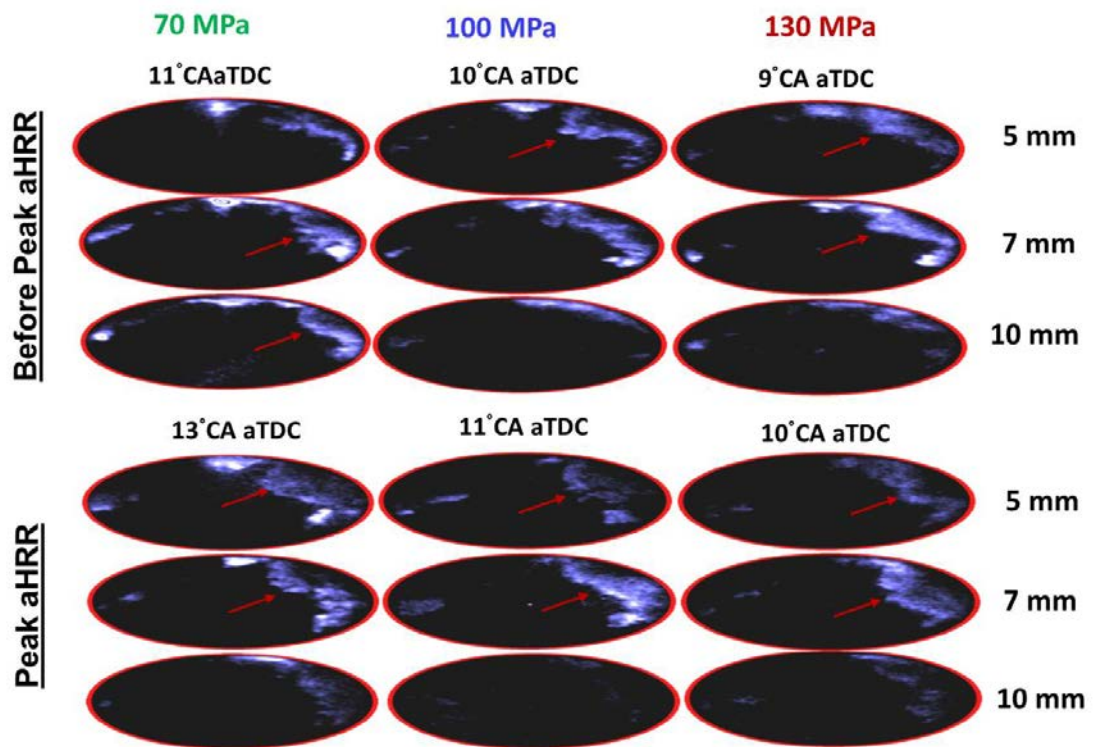


Figure 6.8 The OH-PLIF images taken at 5, 7 and 10 mm below the cylinder head at around the peak aHRR timing for various injection pressures. The 7-mm images are repeated from Figure 13 for comparison purposes

higher injection pressure conditions. The influence of injection pressure on the vertical distribution of OH signals is also observed in Fig. 6.8. For example, the OH signals appear to spread widely to the lower plane in all planes for the 70-MPa injection condition, but the OH signals are found mostly in the first two planes for higher injection pressure conditions. This indicates that the high-temperature reaction occurs at higher plane for higher injection pressure, most likely because the fuel jet would impinge on the bowl wall and then moves further up towards the cylinder head [14].

6.6. Summary

The main findings from the injection pressure variations are summarised as follow:

- The start of high-temperature reaction occurs earlier for higher injection pressure due to the increased air entrainment and better fuel-air mixing. The burn duration decreases with increasing injection pressure which increases the rate of heat release and in turn the in-cylinder pressure.
- For any fixed injection pressure condition, the up-swirl side of a wall-interacting jet shows shorter penetration length than that on the down-swirl side. With increasing injection pressure, both up-swirl and down-swirl jet penetrate further due to higher injection momentum.
- The cool-flame signals are originated from the wall-jet head region regardless of the injection pressure likely due to locally enhanced mixing in the wall-jet head region as a turbulent ring-vortex is formed during jet-wall interactions. This head vortex will become stronger with increasing injection pressure which contributes to the increased cool-flame chemiluminescence signals, together with the earlier end of injection and thus increased pre-combustion mixing time.
- The high-temperature reaction starts to occur in the same wall-jet head region of the low-temperature reaction and the turbulent ring-vortex for all injection pressures.

The expansion of both OH* and OH-PLIF in this region is evident and becomes larger with increasing injection pressure, likely due to the enhanced heat vortex. The higher injection pressure also causes earlier start of combustion on account of the enhanced mixing. The difference between up-swirl and down-swirl sides of the jet diminishes as the injection pressure increases and overcomes the swirl flow. However, the swirl still has impacts on the diesel jet structure such that the up-swirl reaction occurs closer to the jet axis than the down-swirl reaction does.

Chapter 7.

Soot processes

Previous chapters focusing on the development of fuel jet and high-temperature flame structures have provided an improved understanding of a wall-interacting fuel jet in a light-duty diesel engine. This chapter presents additional information about soot within the flame by performing planar laser induced incandescence (PLII) imaging. All the diagnostics performed in the previous chapters were repeated once again to compare the structures of a reacting fuel jet and soot within it. The same optical diesel engine and fuel injection system (including a single hole nozzle orientated to 2 o'clock) were used while a selected injection pressure of 100 MPa with injection timing at -7.3°CA aTDC (or 7.3°CA bTDC) and injected mass of 10 mg was applied. At the conclusion of Chapter 6, however, two major changes were made in terms of the piston shape and fuel. As mentioned previously, the former was to include a curved bowl-wall shape so that the fuel penetration back towards the nozzle via a tumbling motion, which is widely found in production engines, could be reproduced. The latter was due to the diagnostic considerations such that a conventional diesel fuel with high aromatics contents would cause significant beam attenuation issues and thus a low-sooting surrogate fuel would be required, especially for soot diagnostics. These two issues will be discussed in details before the results are presented.

7.1. Curved piston bowl – Piston B

As discussed in detail in Chapter 3.1.2, the piston underwent a design modification for the increased field of view and for the inclusion of a curved bowl-wall shape. Figure 7.1 shows still images from high-speed movies of natural combustion luminosity (predominantly hot soot luminosity [13, 20, 81]) when the optical engine was equipped with Piston A (top two rows) and Piston B (bottom two rows), both at the same operating condition of 100 MPa injection pressure (Table 3.3). The movies were taken using a high-speed CMOS camera (VisionResearch

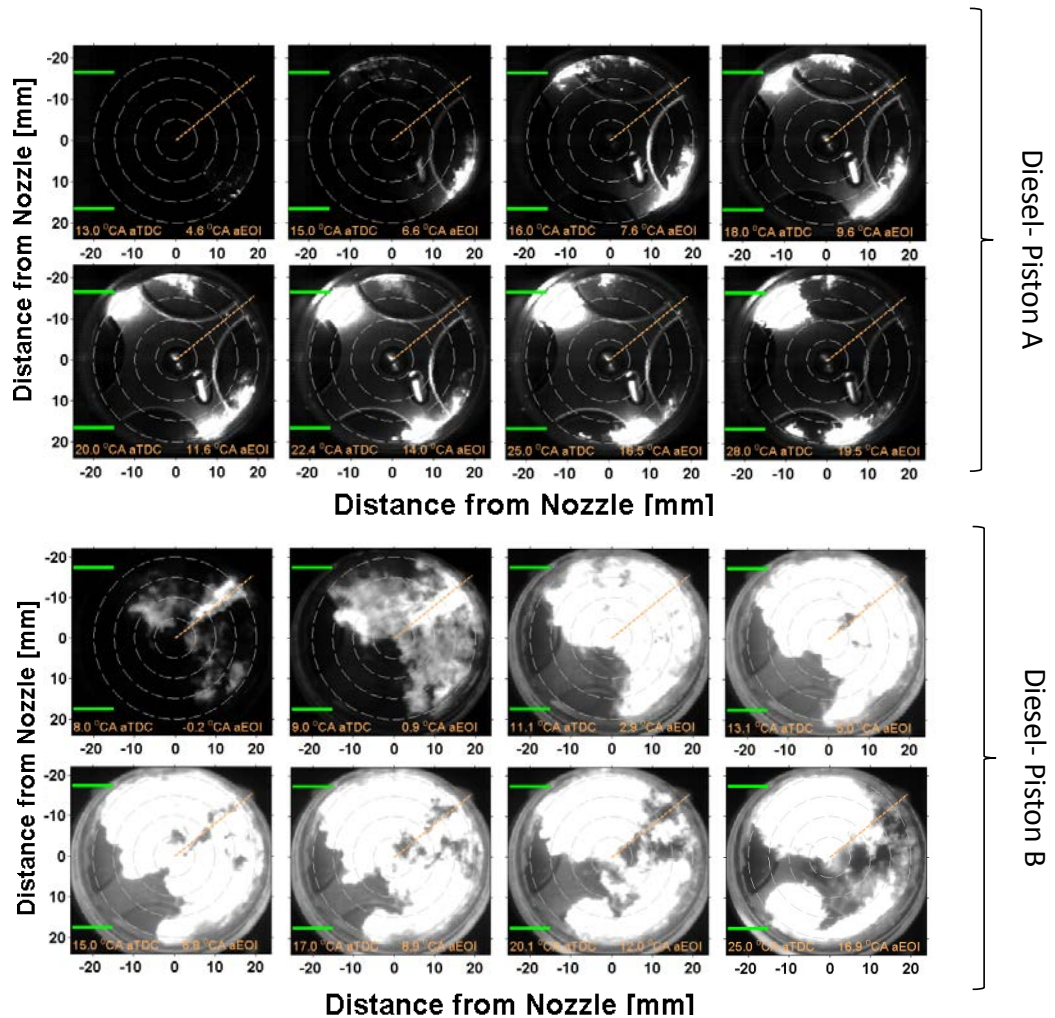


Figure 7.1 Still images from high-speed movies of natural diesel combustion luminosity for a selected cycle of piston type A (top) and piston type B (bottom)

Phantom v7.3) equipped with a 50-mm f/1.4 Nikkor lens . The imaging was performed at 36,000 frames per second and with 10 μ s exposure time. Despite being line-of-sight integrated ones containing broadband signals, the combustion luminosity images provide useful information about the overall fuel jet development. In each image, a dashed line pointing at 2 o'clock is illustrated to denote the jet trajectory of the single-hole nozzle. The green horizontal lines shown on the left illustrate the bowl-rim cut-out region from which the laser sheet is inserted. On the bottom-left and bottom-right corners of each image, the corresponding crank angle location ($^{\circ}$ CA aTDC) and time after the end of injection ($^{\circ}$ CA aEOI) are noted, respectively.

Measurable differences in terms of jet development dynamics are seen in Fig. 7.1. For Piston A, the jet splits up into two halves that travel along the wall upon the wall impingement. Also, the luminosity signals appear close to the edge of the field-of-view with no signals in the middle of the bowl, suggesting that the tumbling motion of the jet back towards the nozzle along the bottom of the bowl surface is non-existent. This penetration behaviour is indeed what was observed from the results of Chapters 5 and 6. On the other hand, for Piston B, the soot luminosity signals spread across the bowl surface in addition to the penetration along the bowl wall, indicating there is a significant tumbling motion of the jet back towards the nozzle. It is likely that the fuel jet penetration has been guided by the curved-lip piston bowl-wall as commonly found in production engines. Compared to Piston A, Piston B also provides a larger field of view and more details near the bowl wall, which is advantageous for the study of a wall-interacting jet. However, the strong soot luminosity signals in the laser beam path (left-to-right in Fig. 7.1) suggest a significant beam attenuation issue.

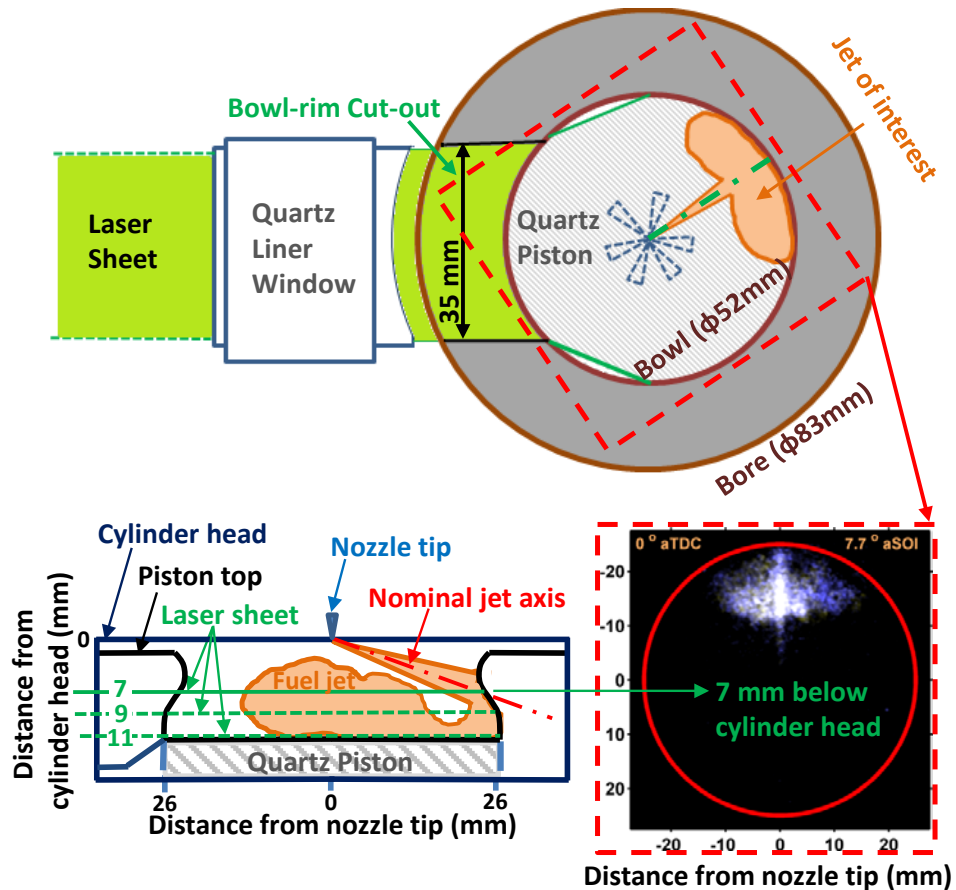


Figure 7.2 Illustration of the laser sheet with respect to the piston bowl and fuel jet in the bottom view (top) and side view (bottom-left). Also shown on the bottom-right corner is an example image of laser-induced fuel fluorescence obtained at 7 mm below the cylinder head.

Figure 7.2 shows the jet development and laser plane positions corresponding to the new piston type B. The new quartz piston, together with slightly widened bowl-rim cut-out, provides a larger field of view of 52 mm in diameter, compared to 43 mm in diameter for piston type A. It has been estimated that the intersection between the nominal jet-axis and the piston bowl wall is about 6.5 mm from the cylinder head, which is below the curved lip area. Therefore, it is expected that most of the fuel will penetrate into the bowl region. This required the planar laser beams to be positioned at 7, 9 and 11 mm below the cylinder head to ensure the visualisation of most of the fuel jet. It is noted that the 7 mm laser plane corresponds to the area where the nominal jet axis intersects the piston bowl wall during the injection event and thus it will be

used as a reference plane. An example image taken at this plane and post-processed for presentation is shown on the bottom-right corner of Fig 7.2. The original image has been rotated so that the fuel jet is shown to be injected upwards (12 o'clock direction) and the wall-impinged jet is penetrating downwards (back towards the nozzle) upon the impingement on the bowl wall.

7.2. Methyl decanoate – low sooting surrogate fuel

Having been added with aromatics (up to 30%), a conventional diesel fuel produces a large amount of soot, which causes a serious beam attenuation issue. As mentioned in the previous chapter, the beam attenuation was already problematic with OH-PLIF. If PLII imaging were

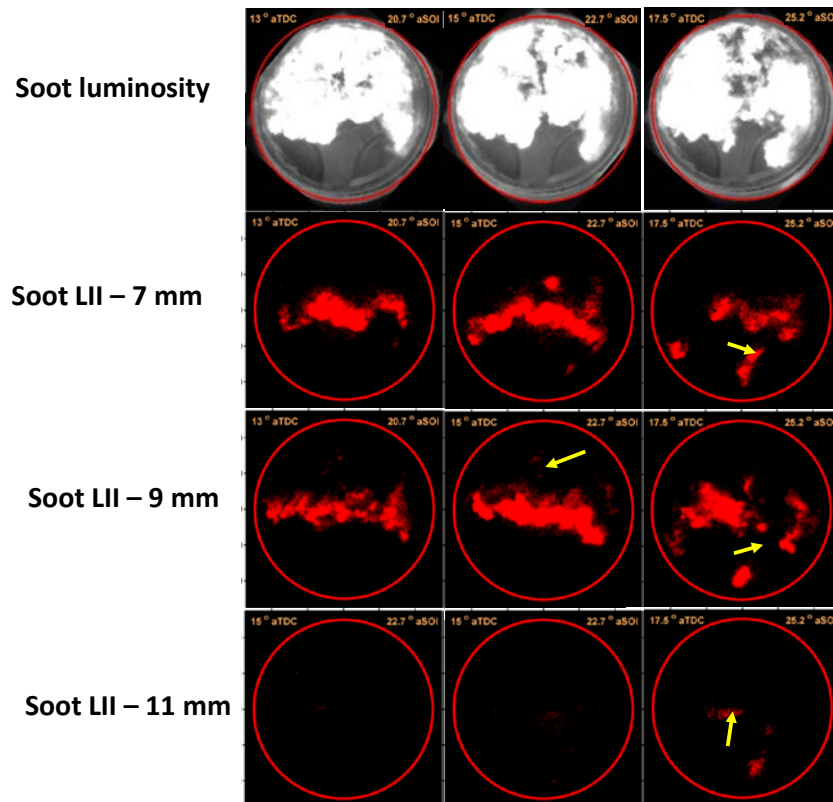


Figure 7.3 . Line-of-sight integrated soot luminosity (top row) and soot planar laser-induced incandescence (PLII) images at 7, 9 and 11 mm (bottom) from conventional diesel during the sooting period at 13°, 15° and 17.5°CA aTDC. Yellow arrows highlight the area where signals were lost due to attenuation

performed under such a condition, a significant portion of the signals would be lost. Figure 7.3 shows some preliminary results allowing to discuss the beam attenuation issue associated with the use of a conventional diesel fuel. The figure presents the images captured from soot luminosity (first row) and soot-PLII (pseudo-coloured red) during the main sooting period from 10° to 20°CA aTDC, when the engine was operated on conventional ultra-low sulphur diesel fuel and equipped with Piston B. The PLII images were obtained from three different laser planes so that once they were integrated, the overall soot structures would match the shape of soot luminosity signals. However, it is very obvious from the images of Fig. 7.3 that the signals near the bowl wall cannot be detected due to the attenuation of laser beam travelling from bottom-left to top-right for the given image orientation. PLII signals can also be seen to be abruptly cut off at certain zones, further indicating attenuation. Via visual inspection, the yellow arrows in Fig. 7.3 were added to highlight these attenuated areas.

Previous researchers addressed the beam attenuation issue by using aromatics-free, single-component fuels with similar ignition quality and physical properties of conventional diesel. For instance, Dec *et al* used a mixture of tetra-eth-oxy-propane (TEOP) and hepta-methyl-nonane (HMN) [46, 70] for its low soot and fuel fluorescence signals (or interference) [13]. Many studies used n-heptane due to the availability and simplicity of chemical kinetic models, providing opportunities for computational modelling [33, 38, 39, 107]. Table 7.1 summaries various surrogate fuels used for soot diagnostics.

Table 7.1 Alternative fuels used in diesel combustion researches

| Fuel type | REF. |
|---|--------------------|
| Reference diesel/ultra-low sulphur diesel | 11, 13, 33, 108 |
| Mixture of TEOP (tetra-eth-oxy-propane) and HMN (hepta-methyl-nonane) | 46, 70 |
| 32 % HMN and 68 % n-Hexadecane (nC16) | 33 |
| n-Heptane | 33, 38, 39, 41, 72 |
| Mixture of n-heptane and iso-octane | 41, 109, 110 |
| $C_{12}H_{26}$ (19.7 %) $C_{13}H_{28}$ 52.4 % $C_{14}H_{30}$ 27.1 % | 111, 112 |

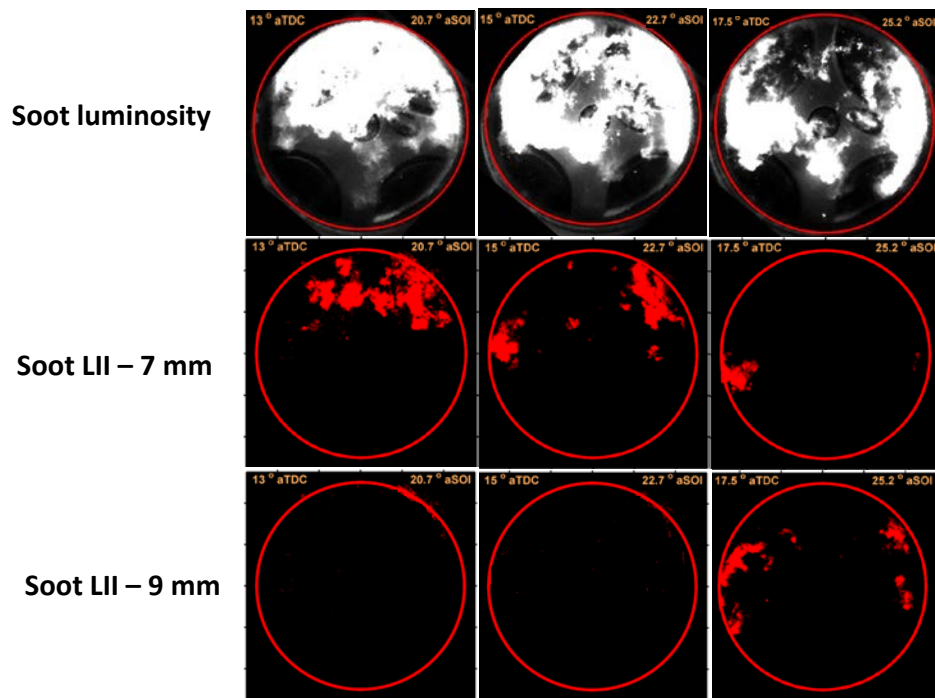
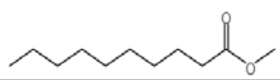


Figure 7.4 Line-of-sight integrated soot luminosity (top row) and soot planar laser-induced incandescence (PLII) images at 7, 9 and 11 mm (bottom) from Methyl-decanoate (MD) during the sooting period at 13°, 15° and 17.5° CA aTDC.

In the present study, methyl decanoate ($C_{11}H_{22}O_2$) was selected as a low-sooting surrogate fuel for diagnostic purposes. This fuel is oxygenated and as a fatty acid methyl ester, it can be considered as a surrogate fuel for biodiesel. There are chemical kinetic models available for computational simulation [113-115] and the cetane number of 47-52 [116-118] is similar to a conventional diesel fuel (i.e. 51) used in the previous experiments. Previous studies confirmed that the methyl decanoate is very low sooting, which therefore is a good candidate for PLII diagnostics [116]. Table 7.2 lists selected properties of the tested methyl decanoate together with diesel properties.

Table 7.2 Properties of Methyl-decanoate and conventional diesel

| Properties of Fuel | Methyl-decanoate value [117-121] | Diesel value [122] |
|--------------------------------|---|------------------------|
| Composition | $C_{11}H_{22}O_2$  | - |
| Cetane number | 48-52 | 52 |
| Heat of combustion | 36.67 MJ/kg | 45.6 MJ/kg |
| Kinematic viscosity | 1.71 mm ² /s | 3.0 mm ² /s |
| Density @ 297°K | 0.871 g/ml | 0.83 g/ml |
| O₂ ratio (Ω) | 6.1% | - |

Preliminary tests performed using methyl decanoate showed promising results. Figure 7.4 shows the soot luminosity and soot LII images taken at 13°, 15° and 17.5°CA aTDC corresponding to the high sooting period of methyl decanoate. Compared to the results shown in Fig. 7.3, the images in Fig. 7.4 clearly indicate that the soot LII images are free from the beam attenuation issue with strong signals observed even near the bowl wall.

While the beam attenuation issue has been resolved using methyl decanoate, a question is raised: what if the flame structures are largely different between diesel and methyl decanoate? Figure 7.5 shows images from hot soot luminosity movies to address this question. The images show that the hot soot luminosity appears at 7.9°CA aTDC for diesel, earlier than for methyl decanoate at 9°CA aTDC . At a given crank angle location, the hot soot region is much larger for diesel and the signal lasts longer. For example, at 25°CA aTDC , the diesel soot luminosity is still strong and retains the flame structure whereas the methyl decanoate signals are almost all burnt out (bottom-right image). While the soot luminosity signal strength is very different, it is important to note that the dynamics of the wall-interacting jet development characterised by the

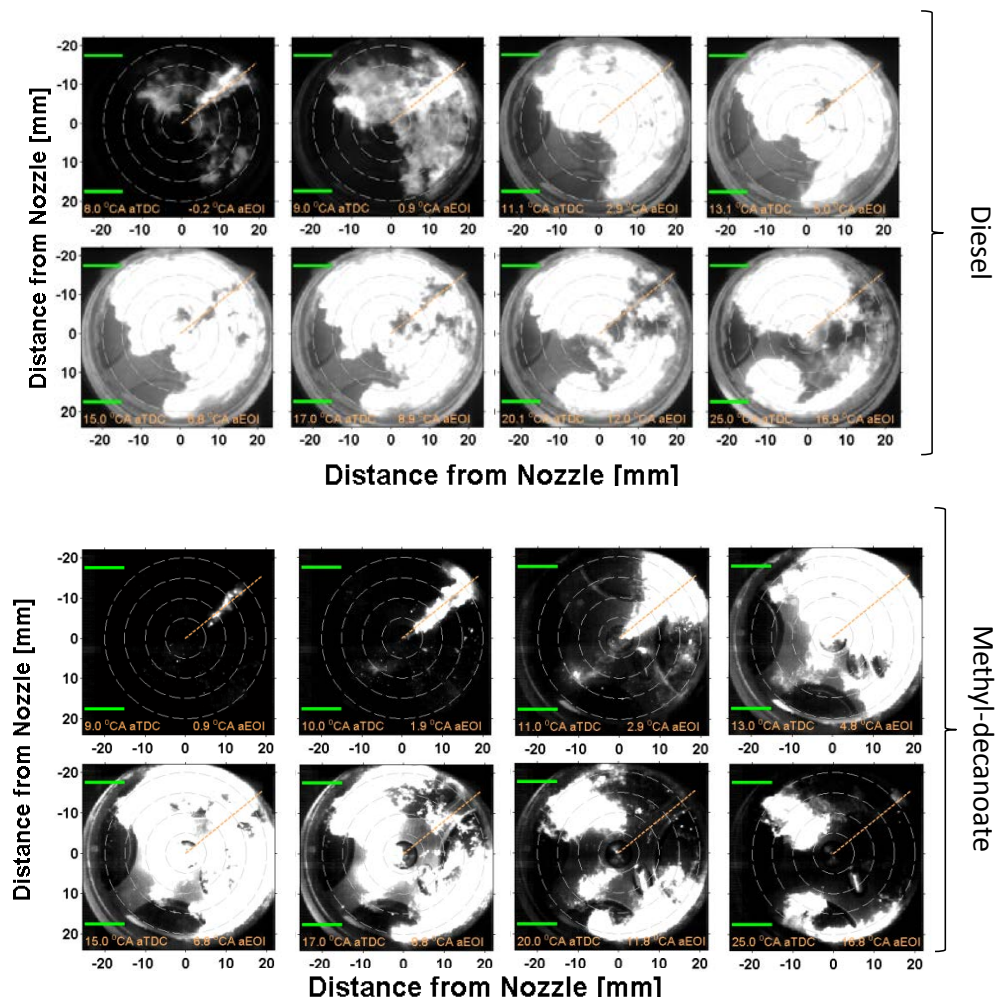


Figure 7.5 Still images from high-speed movies of hot soot luminosity for a selected cycle of diesel (top) and methyl decanoate fuel (bottom)

fuel impingement on the wall soon after the start of injection, the rebound against to the bowl wall, the penetration back towards the nozzle and the flow along the wall curvature are very similar between two fuels. The strong circulating signals in the wall-jet head region, indicating the ring vortices formed during the jet-wall interaction [18, 20], are also evident for both fuels. Therefore, the hot soot luminosity images in Fig. 7.4 confirm that methyl decanoate is an excellent surrogate fuel to study the development of a wall-interacting diesel jet with its lower sooting tendency to help reduce the laser attenuation issue.

7.3. Combined PLII and OH-PLIF images

In addition to PLII images, online and offline OH-PLIF imaging were repeated using the new piston and new fuel. Figure 7.6 shows an example of these images with the combined

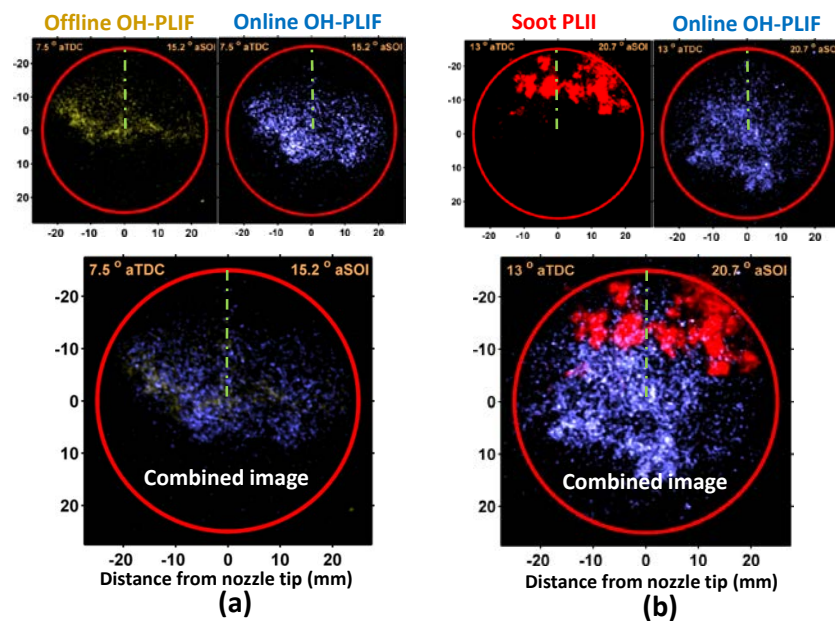


Figure 7.6 (a) Offline OH-PLIF (top-left) and online OH-PLIF signals (top-right) pseudo-coloured in yellow and blue, respectively, and their combined image (bottom) and (b) Soot-PLII (top-left) and OH-PLIF signals (top-right) pseudo-coloured in red and blue, respectively, and their combined image (bottom). On the combined images, the corresponding imaging times are denoted in crank angle degrees after top dead centre ($^{\circ}$ aTDC) and after the start of fuel injection ($^{\circ}$ aSOI). All images were obtained 7 mm below the cylinder head.

online/offline image on the left and the combined PLII/OH-PLIF image on the right. The combined image of PLII and OH-PLIF provides a great opportunity to discuss potential soot oxidation due to OH radicals by being able to compare their structures.

7.4. Cyclic variations of PLII images

As discussed in section 4.4 of Chapter 4, there are inherent cyclic variations impacting the laser-based images. Figure 7.7 shows the traces of in-cylinder pressure and corresponding apparent rate of heat release (aHRR) for all 20 firing cycles for the new piston type B and methyl decanoate fuel. Also shown using a red line are ensemble-averaged traces. It is observed that before the start of injection at 7°CA bTDC, the individual in-cylinder pressure traces match well with the ensemble-averaged trace. However, as the injection starts, the variations due to evaporative cooling become noticeable. The variations during the combustion event are also

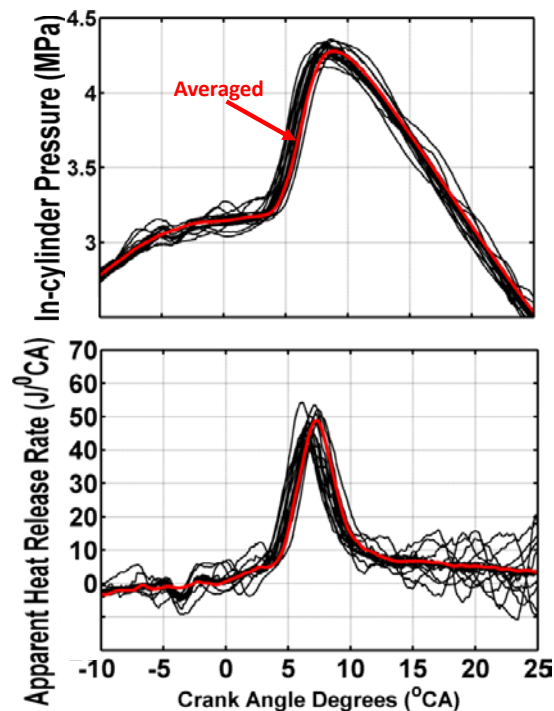


Figure 7.7 In-cylinder pressure traces of 20 instantaneous cycles and their ensemble average (top). Shown at the bottom are the corresponding traces of apparent heat release rate.

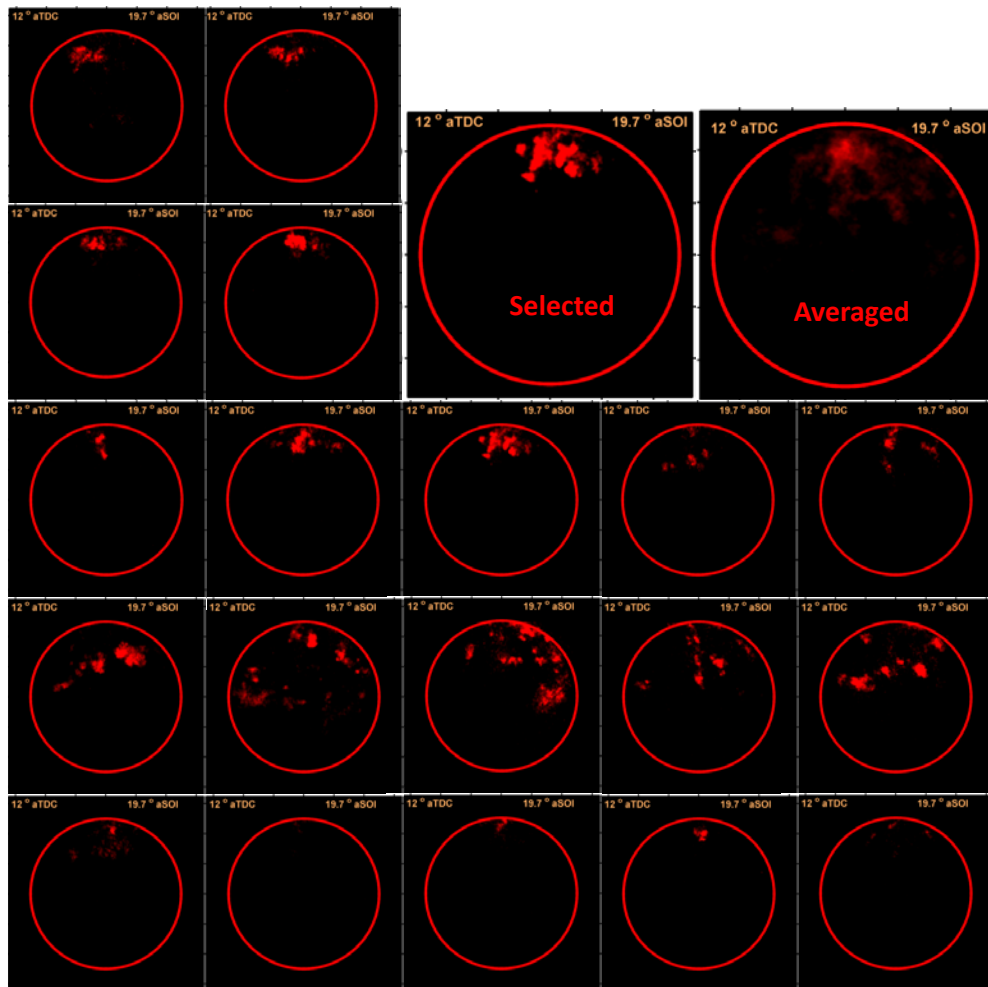


Figure 7.8 Individual soot-PLII images of 20 engine cycles at 12°CA aTDC. The representative PLII image of the 20-image set is shown at the top-right. All images were taken at 7 mm below the cylinder head.

measurable with the rise of the in-cylinder pressure starting between 3~5°CA aTDC and the peak pressure varying between 4.3~4.4 MPa.

Figure 7.8 shows that the cyclic variations in the PLII images are quite measurable, which is more significant than those in OH-PLIF images. For example, the LII signals are found near the bowl wall at 12 o'clock position in most of the images; however, it is also seen that the soot pockets are scattered as in the second last row or non-existent as in the bottom row. Similar to the OH-PLIF images, however, the image averaging results in smeared out signals missing

details associated with turbulent soot structures. Therefore, in this chapter, a similar image selection method used for the OH-PLIF images was used again. The selected image shown in Fig. 7.8 suggests that the overall structure matches well with the averaged image while maintaining structural details such as a few soot pockets with various sizes and shapes.

7.5. In-cylinder pressure and apparent heat release rate

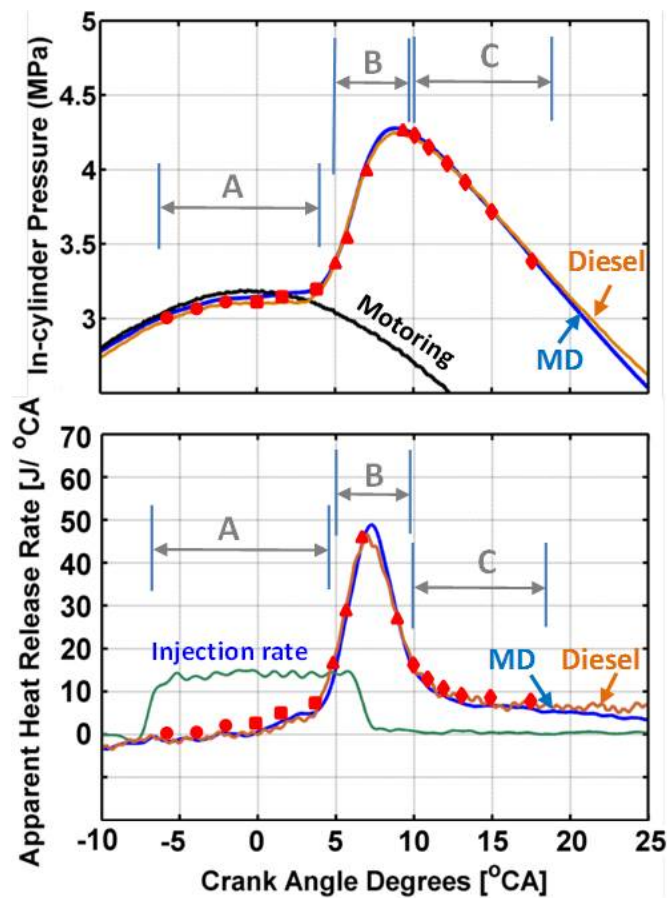


Figure 7.9 Averaged in-cylinder pressure (top) and the apparent heat release rate (aHRR) traces (bottom) for the selected engine operating conditions. The traces for conventional diesel are orange coloured and MD's blue. Also shown in the aHRR plot is the measured injection rate profile for both fuels. The laser-based imaging times are illustrated on both in-cylinder pressure and aHRR traces using (A) circles/squares for the ignition delay phase, (B) triangles for the premixed combustion phase, and (C) diamonds for the mixing-controlled combustion phase.

Figure 7.9 shows the in-cylinder pressure traces for motoring (no fuel injection) and firing modes (top) and the derived apparent heat release rate together with the measured injection rate (bottom). The pressure and heat release traces of methyl decanoate (abbreviated to MD) are plotted together with the diesel traces, with blue lines representing MD and orange ones for diesel. Shown on the traces of MD are symbols to indicate the corresponding crank angle locations of the OH-PLIF and PLII imaging for various combustion stages including circles and squares for the ignition delay period (A), triangles for the premixed combustion stage (B) and diamonds for the mixing-controlled combustion phase (C). It is noticeable that the in-cylinder and aHRR traces of MD and diesel are very similar, which is consistent with the similar cetane number.

Figure 7.9 shows that the in-cylinder pressure of the firing mode initially follows the motoring trace but becomes lower as the fuel injection starts at 7°CA bTDC. Similar to diesel, this is due to the evaporative cooling of liquid-phase methyl decanoate, which also explains the negative aHRR [4, 47]. During this early stage, identified as the ignition delay period, PLIF signals should be predominant from vaporising fuel as observed in the previous chapters. While the fuel injection continues, a mild increase in the aHRR is noticeable at around TDC to 4°CA aTDC. This corresponds to the first-stage ignition and low-temperature reaction [14] where cool-flame chemiluminescence signals can be captured from early combustion products such as CH, CO and HCHO radicals. The aHRR starts to increase at a much higher rate from 4°CA aTDC, suggesting the second-stage ignition and high-temperature reaction [93] – i.e. start of combustion. The mixture prepared during the ignition delay period combusts quickly during this premixed burn phase [4], emitting strong signals from OH radicals. Therefore, the offline/online OH-PLIF imaging together with the OH* chemiluminescence and PLII imaging was performed from this main combustion stage. The aHRR peaks at 7.5°CA aTDC and declines as quickly as it rises until 10°CA aTDC. It is noted that the injection ends in the middle of the premixed burn phase at around 7.5°CA aTDC but the remaining fuel still combusts while being mixed with air

in the following crank angles – i.e. mixing-controlled burn phase (including late-cycle burn-out). This is evidenced by the slowdown of the aHRR from 10°CA aTDC. The imaging diagnostics were performed up to 25°CA aTDC when the aHRR returned back to the level at the start of combustion at 4°CA aTDC.

7.6. Ignition delay period and low-temperature reaction

Figure 7.10 displays the images corresponding to the ignition delay period. Shown in the top row are the fuel-PLIF images taken at 7 mm below the cylinder head for three different

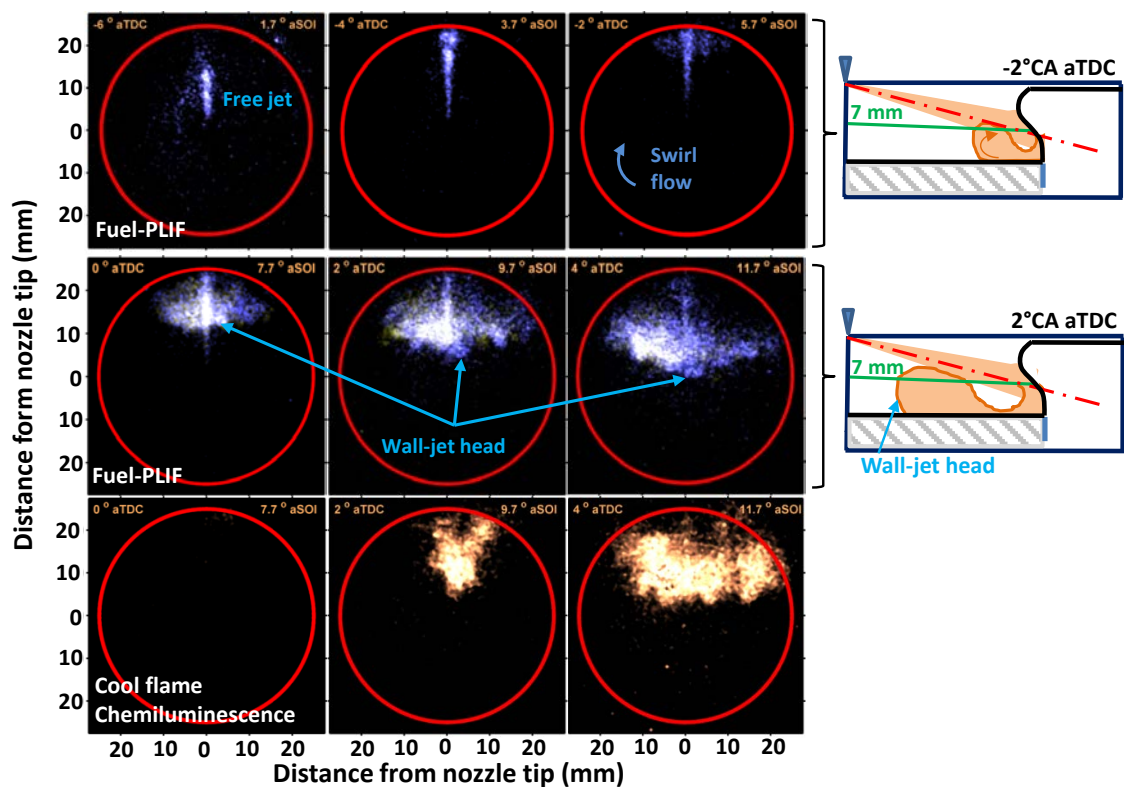


Figure 7.10 Planar laser induced fluorescence (PLIF) signals and cool-flame chemiluminescence signals during the ignition delay period. Shown on the first two rows is the development of a non-reacting fuel jet during jet-wall interaction. Also shown on the bottom row are the cool-flame signals corresponding to the images on the middle row. Illustrations at the right show the used laser sheet position (7 mm below the cylinder head) with respect to the piston position at a given crank angle location and the postulated fuel jet development.

crank angles of -6, -4, and -2°CA aTDC. It should be noted that the red circle on each image illustrates the bowl wall as well as the field-of-view provided by the quartz window (i.e. the field-of-view covers the entire bowl). On the right side of the three images, the side-view illustration of fuel jet and laser sheet corresponding to the piston position at -2°CA aTDC is presented. The fuel-PLIF images show that the methyl decanoate jet penetrates freely upon the start of injection before it impinges on the bowl wall at -4°CA aTDC. After the wall-impingement, the fuel jet travels not only along the bowl wall but also along the bottom of the piston bowl as seen at -2°CA aTDC. Shown in the middle row of Fig. 7.10 are the PLIF images at the same 7 mm laser plane from TDC to 4°CA aTDC and on the right is the side-view illustrations of the laser plane, piston bowl and the fuel jet. Since Fig. 7.9 shows positive aHRR at these crank angles, thus reactions being expected, both online and offline OH-PLIF imaging have been performed. When they are combined onto one image using yellow for the offline signal and blue for the online OH-PLIF, the signals overlap in most of the jet area and appear in white colour. Therefore, the PLIF signals are interpreted as fuel-PLIF again. The images show that the fuel jet continues to penetrate further along the bowl wall reaching half of the bowl circumference at 4°CA aTDC. At the same time, the fuel jet appears to bounce off the bowl wall and travels back towards the nozzle, which is shown as a downward movement of the wall-jet head in these bottom-view images. It is noted that this downward penetration occurs below the free jet trajectory, which is enhanced due to the curved lip design of the used piston. This means the wall-interacting fuel jet also travels along the bottom surface of the bowl.

In the bottom row of Fig. 7.10 are shown, the cool-flame chemiluminescence images corresponding to the fuel-PLIF images in the middle row. It is seen that the cool-flame signals first appear near the jet axis and in the wall-jet head region at 2°CA aTDC when the aHRR becomes positive (Fig. 7.8). The cool-flame region grows quickly, matching the size of the fuel jet head region in just two crank angles. It is noticeable that the cool-flame signals are much stronger at the wall-jet head than those near the bowl wall. Similar to previous observations in

Chapters 5 and 6, this promotion to first-stage ignition is likely due to the enhanced mixing caused by the jet-wall interaction-induced turbulent ring-vortex. In contrast to the diesel fuel in previous chapters, however, it is interesting to note that the fuel-PLIF images show no strong influence of the in-cylinder swirl flow. This can be explained that the curved bowl-lip shape added to the piston causes the downward penetration of the jet and therefore, the swirl-induced jet asymmetry does not stand out as much as in previous experiments. It should be noted, however, the swirl ratio of this study is low at 1.4. If higher swirl ratios were applied, a significant influence of swirl observed in the previous chapters for piston type A would also be seen for piston type B.

7.7. High-temperature reaction: premixed burn phase

Figure 7.11 shows the OH* chemiluminescence images (top row) and the combined online/offline OH-PLIF images at 7 mm below the cylinder head (bottom row) for various crank angles of 5~9°CA aTDC. On each image, a green vertical dash line is drawn to illustrate the jet axis. The transition from the first-stage ignition to the second-stage one occurs very quickly. For comparison purposes, the cool-flame boundary at 4°CA aTDC is overlaid on the OH* chemiluminescence image taken at 5°CA aTDC and is shown on the top-left. It is seen that the first OH* signal appears within the cool-flame boundary and to the right of the jet axis, before they grow further in the radial direction.

The effect of in-cylinder swirl flow is again seen in the earlier appearance and faster growth of OH* zone on the right side of the jet. It is likely that, although it has had only a minor influence on the jet penetration and low-temperature reaction (Fig. 7.10), the effect of higher scalar dissipation rate caused by the opposing swirl-flow is still extant [100, 101]. The OH* chemiluminescence signals then grow rapidly across the entire wall-jet region. By 7°CA aTDC, almost half of the bowl area is filled up with OH* signals and at 9°CA aTDC, OH* is found

throughout the bowl area. It should be noted that the growing OH* chemiluminescence region is also consistent with the high aHRR seen in Fig. 7.9.

However, OH* chemiluminescence signals are line-of-sight integrated and thus the information is limited. For example, whether the first OH* signal observed at 5°CA aTDC is from the near nozzle region close to the cylinder head or the leading edge of the penetrating wall-jet below the cylinder head is unclear. Therefore, the combined online/offline OH-PLIF images taken at 7 and 9 mm below the cylinder head are used for analysis, as shown in Fig. 7.11. The PLIF image at 5°CA aTDC demonstrates that the signals are mostly yellow (as on the far left) or white (as on the left to the jet axis) in both laser planes, suggesting that the fuel

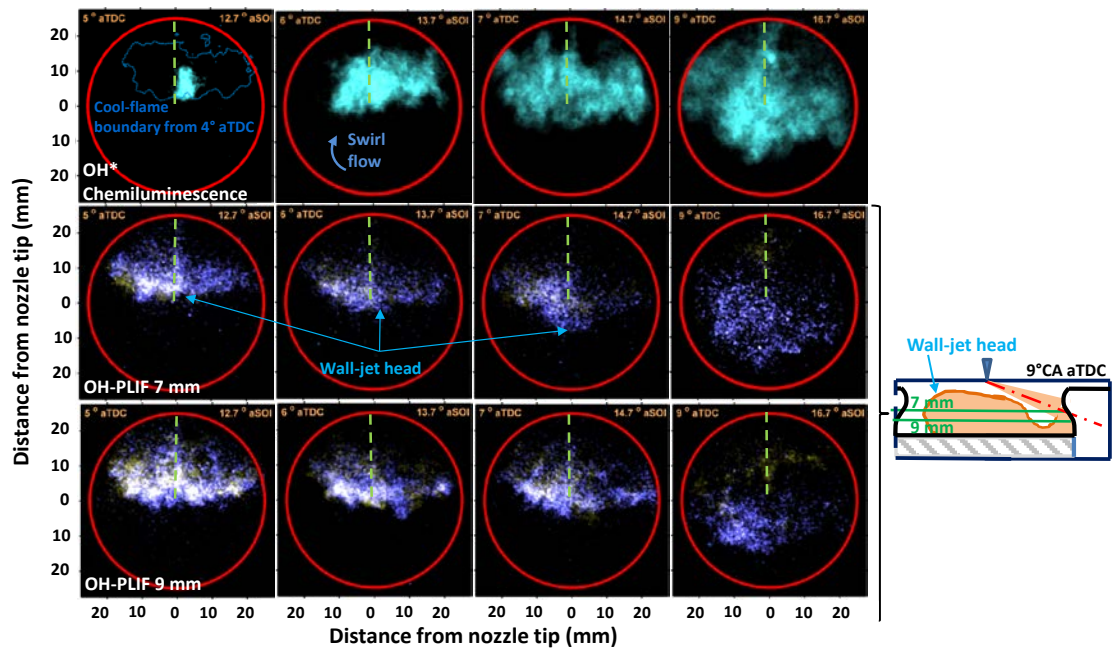


Figure 7.11 OH* chemiluminescence images (top) and corresponding planar laser induced fluorescence (PLIF) signals of OH (online/offline combined) at 7 mm (middle) and 9 mm (bottom) below the cylinder head during the premixed burn phase. The vertical dashed-dot line indicates the fuel jet trajectory. Illustration to the right shows the used laser sheet position with respect to the piston position at a given crank angle and the postulated fuel jet development

fluorescence is still dominant. However, from the 7 mm plane, it is noticeable that the signals on the right to the jet axis are dominantly blue with minimal or no yellow, indicating that OH radicals are generating in this region as the high-temperature reaction starts to occur. As this region is penetrating past the nozzle centre line in the opposite direction to the injection, at 7 mm from the fire deck, the first detected OH* chemiluminescence signal is not likely from the near nozzle region but from the tip of the penetrating wall-jet. This is consistent with the observation in the previous chapters about the wall-interacting jet that the high-temperature reaction was originated from the head vortex region where mixing was locally enhanced and the first low-temperature reactions occurred.

At later crank angles, signals from the fuel fluorescence (i.e. yellow and white) diminish quickly at the jet head region and by 9°CA aTDC, OH signals are mostly found. However, the yellow-coloured fuel region is still observed near the wall-impingement point at both 7 and 9 mm below the cylinder head. It is noted that the end of injection occurred at 7.5°CA aTDC (see Fig. 7.9) and thus these fuel fluorescence signals near the wall are likely from the last portion of the fuel injection where the injection rate declines. The reduced momentum of the fuel induces slower penetration and due to the limited air entrainment near the wall-impingement point, the mixtures in this region could be relatively richer [98, 123].

7.8. High-temperature reaction: mixing-controlled burn phase

As the high-temperature reactions continue to occur, the fuel near the bowl wall seen in Fig. 7.10 and 7.11 is consumed quickly. This is clearly noticed in the OH-PLIF images at later crank angles of 10 to 17.5°CA aTDC, as shown in Fig. 7.12. In the top row, the online/offline combined OH-PLIF images taken at 7 mm below the cylinder head are presented, in which the signals are purely blue OH-PLIF and no more interferences are detectable. Since the injection ended at 7.5°CA aTDC and the aHRR continued to decline at this imaging time, it was

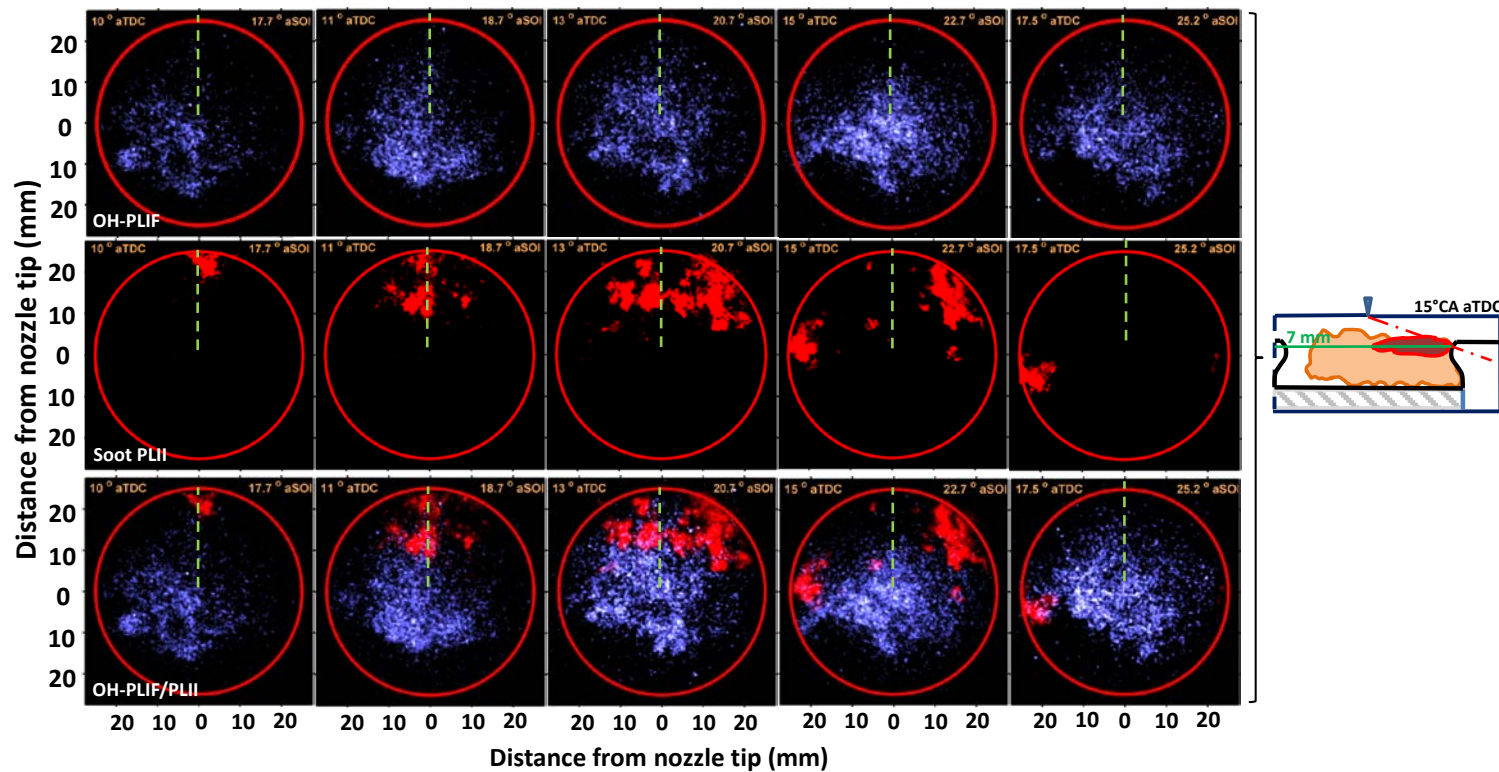


Figure 7.12 Planar laser induced fluorescence (PLIF) signals of OH (online/offline combined, top), planar laser-induced incandescence (PLII, middle) of soot, and the combined image (bottom) during the mixing-controlled burn phase. The vertical dashed-dot line indicates the fuel jet trajectory. Illustration at the right shows the used laser sheet position (7 mm below the cylinder head) with respect to the piston position at a given crank angle location and the postulated fuel jet development

identified as the mixing-controlled burn phase. An interesting trend observed from the OH-PLIF images in Fig. 7.12 is that strong OH signals persist for a long while. The downward penetration of reacting wall-jet and expansion of high-temperature reaction zone continues until the OH signals are found near the opposite side of the bowl wall at 10°CA aTDC. Then, the overall flame structure based on OH distributions remains unchanged until 17.5°CA aTDC. By contrast, marked variations are found in soot distributions as shown in the PLII images taken at the same laser plane and at the same crank angles. The red-coloured images of PLII signals are presented in the middle row of Fig. 7.12. It should be noted that the PLII imaging was performed at earlier crank angles but no signals were observed until the start of mixing-controlled burn at around 10°CA aTDC. The lack of soot formation during the premixed burn phase is different from conventional diesel combustion in a heavy-duty engine [4, 61]; however, it is widely found in highly-diluted low-sooting combustion regimes regardless of the engine size [13, 14, 124]. It should be considered that methyl decanoate used in the present study is a very low-sooting fuel, which also contributes to the delayed soot formation despite no dilution conditions (i.e. no exhaust gas recirculation).

The PLII images also show an interesting trend that soot signals first appear in the wall-impingement point of the jet. As mentioned previously, this is the region with limited mixing and thus locally rich mixtures are expected [18], explaining the high and early soot formation. The soot signals near the wall-impingement point continues to grow between 10 and 13°CA aTDC with increasing numbers of soot pockets in various sizes and shapes. An interesting trend observed from the PLII image at 13°CA aTDC is that the signals are stronger and take up larger space on the right side of the jet axis. This should be explained as the effect of the swirl flow in clockwise direction. In other words, the relatively richer mixture on the down-swirl side leads to higher soot formation than the leaner mixture formed on the up-swirl side, due to the wall-jet travelling against the swirl flow. It is also noticeable that from 13 to 17.5°CA aTDC, the soot pockets appear to be divided into two groups with each flowing along

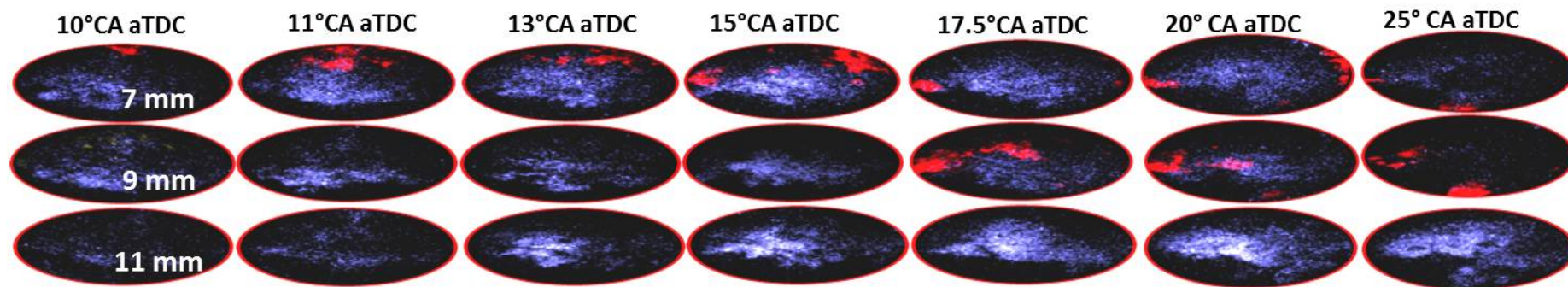


Figure 7.13 The combined images of OH-PLIF signals (online/offline combined) and PLII signals during the mixing-controlled combustion phase. The images were taken at 7, 9, and 11 mm below the cylinder head. Illustration on the right shows the used laser sheet positions with respect to the piston position at a given crank angle location and the postulated fuel jet development.

the bowl wall in either up-swirl or down-swirl direction. At 15°CA aTDC, no soot signals are detected near the wall-impingement point and the soot pockets appear to shrink in size compared to those at 13°CA aTDC, suggesting that the soot oxidation occurs while the pockets flow along the bowl wall.

To further discuss the soot oxidation, the OH-PLIF and PLII images are combined and presented in the bottom row of Fig. 7.12. The images clearly indicate that the soot pockets are surrounded by OH radicals at 10~13°CA aTDC. However, at 15°CA aTDC, the OH signals start to disappear from the wall-impingement region where strong soot signals were found at earlier crank angles. This might suggest that the OH radicals are consumed in the oxidation of soot particles [61, 63, 64]. It is noticeable that at 17.5°CA aTDC, all the soot pockets developed on the right side of the jet axis completely disappear, which once again is consistent with the weakening of OH-PLIF signals in that region. However, there is a small soot pocket remaining in the 9 o'clock position. The cause for this persisting soot pocket is not entirely clear but it could be that the relatively slower development of OH region on the up-swirl side of the jet (see Fig. 7.11) has led to a lower soot oxidation rate. The combined OH-PLIF and PLII images from the other two planes of 9 and 11 mm below the cylinder head are presented in Fig. 7.13. For ease of interpretation, the 7 mm plane is also shown again in a three-dimensional configuration. The figure shows that the OH signals are initially stronger in the upper planes (e.g. 10~13°CA aTDC) but gradually become weaker while the signals increase in the lower planes (15~25°CA aTDC). This is consistent with the downward movement of piston in the expansion stroke. At 25°CA aTDC, the OH-PLIF in the 7 and 9 mm planes are very weak and only the 11 mm plane shows a measurable signal. In comparison, the PLII signals are found only in the 7 mm plane from 10 to 13°CA aTDC. This suggests that the initial soot formation occurs near the bowl-lip area as was observed in Fig. 7.12. The soot signals are not found in the lower planes until 15°CA aTDC. At 17.5°CA aTDC, strong LII signals are observed in the 9 mm plane in the 9 o'clock position as well as in the centre of the bowl. These soot pockets persist quite a while, as shown

in the images at 20 and 25°CA aTDC. Since the new soot formation at this late timing is unlikely, it is thought that the soot formed in the upper plane has been transported into the centre of bowl due to the piston movement. Since the active OH radicals hardly exist at this late crank angle, it is hypothesised that these soot pockets cannot be oxidised but exit through the exhaust.

7.9. Summary

In this chapter, PLII imaging for the investigation of soot processes together with OH-PLIF and fuel-PLIF diagnostics were performed. The same engine and fuel injection system as in the previous chapters were used; however, a new piston shape including a curved bowl-lip design and a new low-sooting fuel for reduced beam attenuation issue were applied. The major findings from this chapter are summarised as follows:

- The curved bowl-lip shape in the piston induces significant jet-wall interactions such that the jet not only travels along the bowl-wall but also bounces off the bowl wall and penetrates back towards the nozzle.
- With the new piston, the swirl flow does not exert significant impact on fuel penetration and low-temperature reaction; however, high influence on high-temperature reactions still exist, evidenced by earlier appearance and faster growth of OH radicals.
- The first PLII signals are detected at the end of premixed burn and at the start of the mixing-controlled combustion phase when the heat release rate declines.
- The first PLII signals are found at the fuel-rich region near the wall impingement point of the fuel jet. The soot pockets then travels along the bowl wall in both up-swirl and down-swirl directions.
- The OH radicals surrounding these pockets disappear while oxidising soot – i.e. OH attack on soot.

- Some remaining soot is transported into the centre of combustion chamber during the downward movement of the piston. These soot signals persist as there are no active OH radicals.

Chapter 8.

Conclusion

In this study, various optical/laser-based imaging diagnostics were performed in a single-cylinder, light-duty, optical diesel engine. These include imaging of natural combustion luminosity, cool-flame chemiluminescence, OH* chemiluminescence, fuel-PLIF, OH-PLIF and soot-PLII. The in-cylinder pressure was also measured to identify the combustion stage corresponding to the imaging timing. The primary aim was to clarify the development of a reacting wall-interacting jet in terms of fuel penetration, low- and high-temperature reaction, and soot behaviour. Based on the major findings from each chapter, new combustion models have been developed as shown in Figs. 8.1 and 8.2.

Figure 8.1 shows that, in a small-bore diesel engine, a diesel jet impinges on the bowl wall forming a wall-interacting jet shortly after the start of injection. The fuel jet splits into two sides with one penetrating against the swirl flow and the other travelling with the swirl. Due to the swirl effect, the up-swirl side of a wall-interacting jet shows shorter penetration length than that on the down-swirl side, suggesting leaner mixtures. The low-temperature reaction of a wall-interacting diesel jet first occurs in the jet head region where a turbulent ring-vortex is formed upon the jet impingement on the wall. The high-temperature reaction then follows, starting from the same wall-jet head region. The swirl flow causes asymmetric flame structures such that the

high-temperature reaction occurs earlier and is stronger on the down-swirl side of the jet due to the swirl-induced richer mixture and lower dissipation rate. During the premixed burn phase, the high-temperature reaction zone continues to expand across the same wall-jet head region where the turbulent ring-vortex is expected.

With increasing injection pressure, both up-swirl and down-swirl jets penetrate further due to higher injection momentum and combustion starts earlier on account of the enhanced fuel-air mixing. The turbulent ring vortex also becomes stronger with increasing injection pressure which contributes to the more intense cool-flame chemiluminescence signals, together with the earlier end of injection and thus increased pre-combustion mixing time. Moreover, the expansion of high-temperature reaction zone in the wall-jet head region becomes larger with increasing injection pressure, likely due to the enhanced ring vortex. As the high temperature reaction matures during the premixed combustion, the difference between up-swirl and down-swirl sides of the jet diminishes, owing to the increase in injection momentum that helps overcome the swirl flow. However, the swirl impacts the diesel jet structure such that the up-swirl reaction occurs closer to the jet axis than the down-swirl reaction.

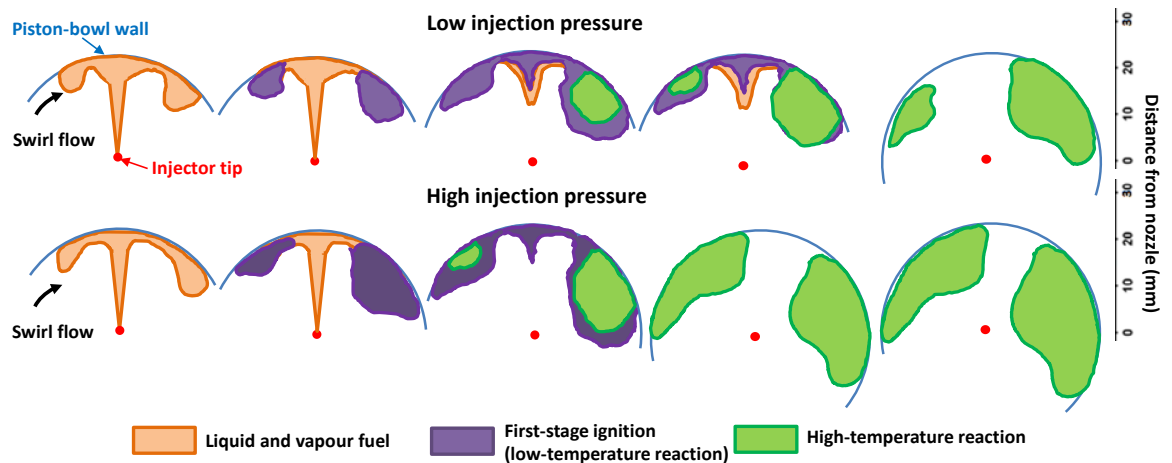


Figure 8.1 Illustration of the influence of injection pressure on the development of a wall-interacting diesel jet in a small-bore diesel engine. The images are arranged in an increasing temporal order from left to right.

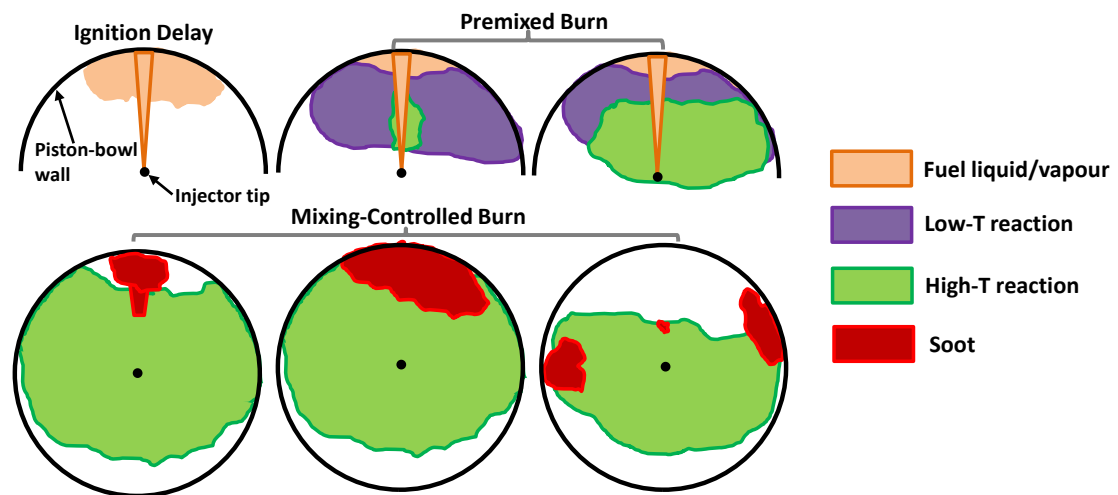


Figure 8.2 Illustration of the development of fuel, low-temperature and high-temperature reactions, and soot of a single fuel jet in a small-bore diesel engine

Figure 8.2 shows the wall-interacting jet development when a curved bowl-lip design is included in the piston shape. Notably, soot is included in the combustion model shown in Fig. 8.2. During the ignition delay period, the injected fuel initially travels as a free jet before impinging on the bowl wall to form a wall-interacting jet. Upon wall-impingement, the fuel jet flows along the bowl wall while at the same time bounces off the bowl wall and travels back towards the nozzle due to the enhanced tumbling motion of the fuel jet. The latter movement occurs below the free jet trajectory and along the bottom surface of the bowl. The jet-wall interaction creates a turbulent ring-vortex in the wall-jet head region where the locally enhanced mixing causes earlier low-temperature reactions. This cool-flame region then grows quickly, matching the size of the entire fuel jet head region. During the premixed burn phase, the transition from the low-temperature reaction to high-temperature reaction first occurs in the leading edge of the penetrating wall-jet. This also first happens on the down-swirl side as the second-stage ignition on the up-swirl side of the jet is delayed due to the higher scalar dissipation rate, resulting in the opposing swirl flow. The high-temperature reaction then expands across the wall-jet head region when the peak rate of the apparent heat release is measured. As the injection ends in the middle of the premixed burn phase, the apparent heat

release rate soon declines and the mixing-controlled burn commences. The soot formation first occurs at around the start of mixing-controlled burn and from the fuel-rich region near the wall-impingement point. This soot region continues to grow with increasing numbers of soot pockets in various sizes and shapes and then get transported along the bowl-wall in both up-swirl and down-swirl directions, most likely due to the strong jet momentum. The soot pockets shrink in size and eventually disappear as the OH radicals are consumed to oxidise soot particles. As the piston moves down late in the expansion stroke, soot pockets follows. However, the soot oxidation process ceases due to OH radicals becoming inactive and these survived soots can exit through the exhaust.

Future work

Combustion inside the cylinder of light-duty engines is very complicated and there are many areas that still require a lot of research efforts to further improve our fundamental understanding. It is noted that this thesis utilised only a single-hole nozzle to isolate the wall-interacting jet development from jet-jet interactions. In production engines, multi-hole nozzles are used to supply required amounts of fuel in a short period at high engine speeds. Therefore, investigations of complicated jet-jet interactions and their impact on the high-temperature reaction zone and soot regions will be needed. The use of optical engine and laser diagnostics similar to those applied in this study will again be very useful to explore the effect of such phenomenon. The flow field measurement using a high-speed Nd:YAG laser will be another diagnostic of interest. The flow measurements both within the jet and surrounding air flows will help understand details of the turbulent ring vortex formation and how quantitatively it impacts the high temperature reactions. Moreover, the engine is operated in naturally aspirated condition in this study, without using emissions reduction technologies such as exhaust gas recirculation and intake air boosting. Hence, further studies repeating these investigations in different engine conditions when incorporating these technologies will provide great support for the development of modern diesel engine.

References

1. European Vehicle Market Statistics, 2013; The International Council on Clean Transportation: [Internet] 2013; [cited 2015 July 21]. Available from: <http://www.theicct.org/european-vehicle-market-statistics2013>
2. Motor Vehicle Census, Australia; Australian Bureau of Statistics [Internet], 2014; [cited 2015 July 21]. Available from: <http://www.abs.gov.au/AUSSTATS/abs@.nsf/DetailsPage/9309.031%20Jan%202012?OpenDocument>
3. Johnson T. Vehicular Emissions in Review. SAE Int J Engines 2014;7(3):1207-1227
4. Dec JE. A Conceptual Model of DI Diesel Combustion Based on Laser-Sheet Imaging. SAE paper 970873; 1997.
5. Siebers D, Higgins B. Flame Lift-Off on Direct-Injection Diesel Sprays Under Quiescent Conditions. SAE paper 2001-01-0530; 2001.
6. Pickett LM, Siebers DL, Idicheria CA. Relationship Between Ignition Processes and the Lift-Off Length of Diesel Fuel Jets. SAE Paper 2005-01-3843; 2005.
7. Higgins, B and Siebers, D. Measurement of the Flame Lift-Off Location on DI Diesel Sprays Using OH Chemiluminescence. SAE Technical Paper 2001-01-0918, 2001
8. The Engine Combustion Network, Lift-Off Length, [Internet] [Cited 2014 Oct]. Available from : <http://www.sandia.gov/ecn/cvdata/expDiag/liftoff.php>.

9. Pickett LM, Siebers DL. Soot Formation in Diesel Fuel Jets Near the Lift-Off Length. *Int J Engine Res* 2006;7:103-30.
10. Siebers DL, Higgins B, Pickett L. Flame lift-off on direct-injection diesel fuel jets: oxygen concentration effects. SAE Paper 2002-01-0890; 2002.
11. Dec, J. and Kelly-Zion, P., "The Effects of Injection Timing and Diluent Addition on Late-Combustion Soot Burnout in a DI Diesel Engine Based on Simultaneous 2-D Imaging of OH and Soot," SAE Technical Paper 2000-01-0238, 2000.
12. Pickett LM, Kook S, Williams TC. Visualization of Diesel Spray Penetration, Cool-Flame, Ignition, High-Temperature Combustion, and Soot Formation Using High-Speed Imaging. *SAE Int J Engines* 2009;2:439-59.
13. Musculus, M. Multiple Simultaneous Optical Diagnostic Imaging of Early-Injection Low-Temperature Combustion in a Heavy-Duty Diesel Engine. SAE Technical Paper 2006-01-0079, 2006.
14. Musculus MPB, Miles PC, Pickett LM. Conceptual models for partially premixed low-temperature diesel combustion. *Prog Energ Combust* 2013;39:246-83.
15. Bruneaux G. Combustion structure of free and wall-impinging diesel jets by simultaneous laser-induced fluorescence of formaldehyde, poly-aromatic hydrocarbons, and hydroxides. *Int J Engine Res* 2008;9:249-65.
16. Andreassi L, Ubertini S, Allocca L. Experimental and numerical analysis of high pressure diesel spray-wall interaction. *Int J Multiphas Flow* 2007;33:742-65.
17. Cossali GE, Coghe A, Brunello G. Effect of Spray-Wall Interaction on Air Entrainment in a Transient Diesel Spray. SAE Paper 930920; 1993.
18. Bruneaux G, Mixing Process in High Pressure Diesel Jets by Normalized Laser Induced Exciplex Fluorescence Part II: Wall Impinging Versus Free Jet, SAE 2005-01-2097, 2005.
19. Song L, Abraham J. The Structure of Wall-Impinging Jets: Computed Versus Theoretical and Measured Results. *ASME J Fluid Eng* 2004;125:997-1005.
20. Pickett LM, López JJ. Jet-Wall Interaction Effects on Diesel Combustion and Soot Formation. SAE paper 2005-01-0921; 2005.

21. Aizawa T, Kosaka H. Laser-Induced Phosphorescence Thermography of Combustion Chamber Wall of Diesel Engine. *SAE Int J Engines* 2008;1:549-58.
22. Bozic G, Ekoto IW, Petersen BR, Kook S, Miles PC. Optical Investigation Into Wall Wetting From Late-Cycle Post-Injections Used for Diesel Particulate Filter Regeneration. *J Eng Gas Turb Power* 2011;133:092803-.
23. Wang X, Huang Z, Zhang W, Kuti OA, Nishida K. Effects of ultra-high injection pressure and micro-hole nozzle on flame structure and soot formation of impinging diesel spray. *Appl Energ* 2011; 88(5):1620-8
24. Chartier C, Aronsson U, Andersson Ö, Egnell R, Johansson B. Influence of jet–jet interactions on the lift-off length in an optical heavy-duty DI diesel engine. *Fuel* 2013;112:311-8.
25. Menkiel B, Donkerbroek A, Uitz R, Cracknell R, Ganippa L. Combustion and soot processes of diesel and rapeseed methyl ester in an optical diesel engine. *Fuel* 2014;118:406-15.
26. Rusly AM, Le MK, Kook S, Hawkes ER. The shortening of lift-off length associated with jet–wall and jet–jet interaction in a small-bore optical diesel engine. *Fuel* 2014;125:1-14.
27. Genzale CL, Reitz RD, Musculus MPB. Effects of Jet-Bowl and Jet-Jet Interactions on Late-Injection Low-Temperature Heavy-Duty Diesel Combustion. *THIESEL 2008 Conference on Thermo- and Fluid Dynamic Processes in Diesel Engines*; 2008.
28. Polonowski CJ, Mueller CJ, Gehrke CR, Bazyn T, Martin GC, Lillo PM. An Experimental Investigation of Low-Soot and Soot-Free Combustion Strategies in a Heavy-Duty, Single-Cylinder, Direct-Injection, Optical Diesel Engine. *SAE Int J Engines* 2011;5:51-77.
29. Ladommatos N, Abdelhalim SM, Zhao H. Effects of exhaust gas recirculation temperature on diesel engine combustion and emissions. *Proc IMechE Part D: J Automobile* 1998;212:479-500.
30. Miles PC. The Influence of Swirl on HSDI Diesel Combustion at Moderate Speed and Load. *SAE Paper 2000-01-1829*; 2000.

31. Bergin M, Reitz R, Oh S, Miles P et al. Fuel Injection and Mean Swirl Effects on Combustion and Soot Formation in Heavy Duty Diesel Engines. SAE Technical Paper 2007-01-0912, 20072006-01-0197
32. Musculus M. Effects of the In-Cylinder Environment on Diffusion Flame Lift-Off in a DI Diesel Engine. SAE Technical Paper 2003-01-0074, 2003
33. Genzale C, Reitz R, Wickman D. A Computational Investigation into the Effects of Spray Targeting, Bowl Geometry and Swirl Ratio for Low-Temperature Combustion in a Heavy-Duty Diesel Engine. SAE Technical Paper 2007-01-0119, 2007
34. Mathews W, Fang T, Coverdill R, Lee C et al. Soot Diagnostics Using Laser-Induced Incandescence within an Optically Accessible HSDI Diesel Engine SAE Technical Paper 2004-01-1412, 2004
35. Miles PC, Collin R, Hildingsson L, Hultqvist A, Andersson Ö. Combined measurements of flow structure, partially oxidized fuel, and soot in a high-speed, direct-injection diesel engine. P Combustion Inst 2007;31:2963-70.
36. Kim D, Ekoto I, Colban W, and Miles P. In-cylinder CO and UHC Imaging in a Light-Duty Diesel Engine during PPCI Low-Temperature Combustion. SAE Int J Fuels Lubr 2009;1:933-956
37. Hildingsson L, Persson H, Johansson B, Collin R. et al. Optical Diagnostics of HCCI and Low-Temperature Diesel Using Simultaneous 2-D PLIF of OH and Formaldehyde. SAE Technical Paper 2004-01-2949, 2004
38. Hildingsson L, Persson H, Johansson B, Collin R. et al. Optical Diagnostics of HCCI and UNIBUS Using 2-D PLIF of OH and Formaldehyde. SAE Technical Paper 2005-01-0175, 2005
39. Kashdan J, Docquier N, and Bruneaux G. Mixture Preparation and Combustion via LIEF and LIF of Combustion Radicals in a Direct-Injection, HCCI Diesel Engine. SAE Technical Paper 2004-01-2945, 2004.
40. Collin R, Nygren J, Richter M, Aldén M et al. Simultaneous OH- and Formaldehyde-LIF Measurements in an HCCI Engine. SAE Technical Paper 2003-01-3218, 2003

41. Amnéus P, Tunér M, Mauss F, Collin R et al. Formaldehyde and Hydroxyl Radicals in an HCCI Engine - Calculations and LIF-Measurements. SAE Technical Paper 2007-01-0049, 2007
42. Dubreuil A, Mounaïm-Rousselle C, Foucher F, and Dagaut P. Comparison between LIF Measurements and Modeling Predictions of OH-HCHO During HCCI Mode Combustion Development. SAE Technical Paper 2007-24-0019, 2007
43. Dec JE, Espey C. Ignition and Early Soot Formation in a DI Diesel Engine Using Multiple 2-D Imaging Diagnostics. SAE Paper 950456; 1995
44. Heywood JB. Combustion in compression-ignition engines. In: A.M. Duffy, J.M. (Ed.), editors. Internal combustion engine fundamentals, New York: McGraw-Hill, 1988, Chapter 8.3.
45. Birch S. Delphi claims world-first for direct-acting diesel injection. SAE International [Internet]. 2008 Sep [cited 2014 May 13]. [about 1 p.]. Available from: <http://articles.sae.org/4200/>
46. Dec, J and Tree, D. Diffusion-Flame / Wall Interactions in a Heavy-Duty DI Diesel Engine. SAE Technical Paper 2001-01-1295, 2001.
47. Kuti OA, Zhu J, Nishida K, Wang X, Huang Z. Characterization of spray and combustion processes of biodiesel fuel injected by diesel engine common rail system. Fuel 2013;104:838-46.
48. Shundoh S, Kakegawa T, Tsujimura K, and Kobayashi, S, The Effect of Injection Parameters and Swirl on Diesel Combustion with High Pressure Fuel Injection. SAE Technical Paper 910489, 1991
49. Rajalingam B and Farrell P. The Effect of Injection Pressure on Air Entrainment into Transient Diesel Sprays. SAE Technical Paper 1999-01-0523, 1999
50. Bruneaux G. Mixing Process in High Pressure Diesel Jets by Normalized Laser Induced Exciplex Fluorescence Part I: Free Jet. SAE Technical Paper 2005-01-2100, 2005

51. Rusly A, Le M, and Kook S. Effect of Injection Pressure on Transient Behaviour of Wall-Interacting Jet Flame Base in an Automotive-Size Diesel Engine. *SAE Int. J. Fuels Lubr.* 2013; 6(3):615-626
52. Bruneaux G. Liquid and vapor spray structure in high-pressure common rail diesel injection. *Atomization Sprays* 2001;11(5):533-556
53. Gumus M, Sayin C, Canakci M. The impact of fuel injection pressure on the exhaust emissions of a direct injection diesel engine fueled with biodiesel–diesel fuel blends. *Fuel* 2012;95:486-494
54. Labecki L, Ganippa LC. Effects of injection parameters and EGR on combustion and emission characteristics of rapeseed oil and its blends in diesel engines. *Fuel* 2012;98:15-28
55. Agarwal AK, Dhar A, Srivastava DK, Maurya RK et al. Effect of fuel injection pressure on diesel particulate size and number distribution in a CRDI single cylinder research engine. *Fuel* 2013;107:84-89
56. Wang X, Huang Z, Zhang W, Kuti OA et al. Effects of ultra-high injection pressure and micro-hole nozzle on flame structure and soot formation of impinging diesel spray. *Appl Energ* 2011;88:1620-1628.
57. Schmid M, Kaiser M, Koch P, Wensing M, Leipertz A. Optical Investigations on Partially Premixed Diesel Combustion for Different Operating Parameters. SAE paper 2008-01-0041; 2008.
58. Singh S, Musculus MPB, Reitz RD. Mixing and flame structures inferred from OH-PLIF for conventional and low-temperature diesel engine combustion. *Combust Flame* 2009;156:1898-908.
59. Siebers DL, Pickett LM, Injection pressure and orifice diameter effects on soot in diesel fuel jets. in: J.H. Whitelaw, F. Payri, C. Arcoumanis, J.M. Desantes (Eds.) *Thermo- and Fluid Dynamic Processes in Diesel Engines 2*, Springer Berlin Heidelberg, 2004, pp. 109-32.
60. Pickett LM, Siebers DL. Soot in diesel fuel jets: effects of ambient temperature, ambient density, and injection pressure. *Combust Flame* 2004;138:114-35.

61. Tree DR, Svensson KI. Soot processes in compression ignition engines. *Prog Energ Combust* 2007;33:272-309.
62. Aronsson U, Chartier C, Andersson Ö, Johansson B. et al. Analysis of EGR Effects on the Soot Distribution in a Heavy Duty Diesel Engine using Time-Resolved Laser Induced Incandescence. *SAE Int J Engines* 2010;3(2):137-155
63. Stanmore BR, Brilhac JF, Gilot P. The oxidation of soot: a review of experiments, mechanisms and models. *Carbon* 2001;39:2247-68.
64. Puri R, Santoro RJ, Smyth KC. The oxidation of soot and carbon monoxide in hydrocarbon diffusion flames. *Combust Flame* 1994;97:125-44.
65. Haudiquert M, Cessou A, Stepowski D, Coppalle A. OH and soot concentration measurements in a high-temperature laminar diffusion flame. *Combust Flame* 1997;111:338-49.
66. Zhang J, Jing W, Fang T. High speed imaging of OH* chemiluminescence and natural luminosity of low temperature diesel spray combustion. *Fuel* 2012;99:226-34.
67. Mancaruso E, Vaglieco BM. Spectroscopic measurements of premixed combustion in diesel engine. *Fuel* 2011;90:511-20.
68. Dec JE, Espey C. Chemiluminescence Imaging of Autoignition in a DI Diesel Engine. SAE paper 982685; 1998.
69. Higgins B, McQuay MQ, Lacas F, Rolon JC, Darabiha N, Candel S. Systematic measurements of OH chemiluminescence for fuel-lean, high-pressure, premixed, laminar flames. *Fuel* 2001;80:67-74.
70. Dronniou N, Kashdan J, Lecointe B, Sauve K, Soleri D. Optical Investigation of Dual-fuel CNG/Diesel Combustion Strategies to Reduce CO₂ Emissions. *SAE Int J Engines* 2014;7.
71. Dec J. and Coy E. OH Radical Imaging in a DI Diesel Engine and the Structure of the Early Diffusion Flame. SAE Technical Paper 960831, 1996

72. Donkerbroek AJ, van Vliet AP, Somers LMT, Dam NJ, ter Meulen JJ, "Relation between hydroxyl and formaldehyde in a direct-injection heavy-duty diesel engine", *Combust Flame* 158 (3):564-72, 2011
73. McManus K, Yip B, Candel S. Emission and laser-induced fluorescence imaging methods in experimental combustion. *Exp Therm Fluid Sci* 1995;10:486-502
74. Battles BE and Hanson RK. Laser-Induced Fluorescence Measurements of NO and OH Mole Fraction in Fuel-Lean, High-Pressure (1-10 atm) Methane Flames: Fluorescence Modeling and Experimental Validation. *J Quant Spectrosc Radiat Transfer* 1995;54:521-537.
75. Paul PH, Gray JA, Durant JL, Thoman JW. Collisional Quenching Corrections for Laser-Induced Fluorescence Measurements of NO A²Σ⁺. *AIAA*, 1994;32:1670-1675.
76. Ketterle W, Schäfer M, Arnold A, Wolfrum J. 2D SingleShot Imaging of OH Radicals Using Tunable Excimer Lasers. *Appl Phys B*, 1992;B54:109-112
77. Dieke GH, Crosswhite HM. The ultraviolet bands of OH Fundamental data. . *J Quant Spectrosc Ra* 1962;2:97-199.
78. Genzale CL, Reitz RD, Musculus MPB. Effects of Piston Bowl Geometry on Mixture Development and Late-Injection Low-Temperature Combustion in a Heavy-Duty Diesel Engine. *SAE Int J Engines* 2008;1:913-37.
79. Davidson DF, Roehrig M, Petersen EL, Rosa MDD, Hanson RK. Measurements of the OH A-X(0,0) 306 nm Absorption Bandhead at 60 atm and 1735 K. *J Quant Spectrosc Radiat Transfer*, 1996;55:755-762.
80. Dawson WR, Windsor MW. Fluorescence yields of aromatic compounds. *J Phys Chem* 1968;72:3251-60.
81. O'Connor J, Musculus M. In-cylinder mechanisms of soot reduction by close-coupled post-injections as revealed by imaging of soot luminosity and planar laser-induced soot incandescence in a heavy-duty diesel engine. *SAE Int J Engines* 2014;7:673-93.

82. Schulz C, Kock BF, Hofmann M, Michelsen H, Will S, Bougie B, et al. Laser-induced incandescence: recent trends and current questions. *Appl Phys B* 2006;83:333-54.
83. Bobba MK, Musculus MPB. Laser diagnostics of soot precursors in a heavy-duty diesel engine at low-temperature combustion conditions. *Combust Flame* 2012;159:832-43.
84. Vander Wal RL. Laser-induced incandescence: excitation and detection conditions, material transformations and calibration. *Appl Phys B* 2009;96:601-11.
85. Vander Wal RL, Weiland KJ. Laser-induced incandescence: Development and characterization towards a measurement of soot-volume fraction. *Appl Phys B* 1994;59:445-52.
86. Zhao H, Ladommatos N. Optical diagnostics for soot and temperature measurement in diesel engines. *Prog Energ Combust* 1998;24:221-55.
87. Fang, T. et al. Air–fuel mixing and combustion in a small-bore direct injection optically accessible diesel engine using a retarded single injection strategy. *Fuel*, 2009. 88(11): p. 2074-2082
88. Musculus, M. P. B.; Dec, J. E. and Tree, D. R. Effects of fuel parameters and diffusion flame lift-off on soot formation in a heavy-duty DI diesel engine. *SAE Technical Papers*, 2002, 2002-01-0889.
89. Design of pressure window. ISP optics. [Internet] [Cited 2014 Sep 1]. Available from:
[\]http://www.ispoptics.com/articles/8/DESIGN%20OF%20PRESSURE%20WINDO](http://www.ispoptics.com/articles/8/DESIGN%20OF%20PRESSURE%20WINDO)
W
90. Pasunurthi SS, Hawkes ER, Joelsson T, Rusly AM, Kook S, Lucchini T, D’Errico G. Numerical study of a diesel engine under motored and combustion conditions. *Proceedings of the 9th Asia-Pacific Conference on Combustion*. Gyeongju, Korea, May 19-22, 2013.
91. Exciton. Rhodamine 6G Data sheet. Available from:
<http://www.exciton.com/pdfs/RH590.pdf>

92. Technical resources. Edmund Optics [Internet] [Cited 2013]. Available from: <http://www.edmundoptics.com>
93. Heywood JB. Combustion in compression-ignition engines. In: A.M. Duffy, J.M. (Ed.), editors. Internal combustion engine fundamentals, New York: McGraw-Hill, 1988, pp. 509-10.
94. Antonius R. Interpreting quantitative data with SPSS, California: Sage Publications Ltd, 2004, pp. 165-467.
95. Naber JD, Siebers DL. Effects of Gas Density and Vaporization on Penetration and Dispersion of Diesel Sprays. SAE Paper 960034; 1996.
96. Chen P-C, Wang W-C, Roberts WL, Fang T. Spray and atomization of diesel fuel and its alternatives from a single-hole injector using a common rail fuel injection system. Fuel 2013;103:850-61.
97. Kim K, Kim D, Jung Y, Bae C. Spray and combustion characteristics of gasoline and diesel in a direct injection compression ignition engine. Fuel 2013;109:616-26.
98. Kook S, Pickett LM, Musculus MPB. Influence of Diesel Injection Parameters on End-of-Injection Liquid Length Recession. SAE Int J Engines 2009;2:1194-210.
99. Musculus MPB, Lachaux T, Pickett LM, Idicheria CA. End-of-Injection Over-Mixing and Unburned Hydrocarbon Emissions in Low-Temperature-Combustion Diesel Engines. SAE Paper 2007-01-0907; 2007.
100. Liu S, Hewson JC, Chen JH, Pitsch H. Effects of strain rate on high-pressure nonpremixed n-heptane autoignition in counterflow. Combust Flame 2004;137:320-39.
101. Liu S, Hewson JC, Chen JH. Nonpremixed n-heptane autoignition in unsteady counterflow. Combust Flame 2006;145:730-9.
102. Nishida K, Zhang W, and Manabe T. Effects of Micro-Hole and Ultra-High Injection Pressure on Mixture Properties of D.I. Diesel Spray. SAE Technical Paper 2007-01-1890, 2007.

103. Kuti O, Zhang W, Nishida K, Wang X et al. Effect of Injection Pressure on Ignition, Flame Development and Soot Formation Processes of Biodiesel Fuel Spray. *SAE Int J Fuels Lubr* 2010;3:1057-1070.
104. Han S and Bae C. The Influence of Fuel Injection Pressure and Intake Pressure on Conventional and Low Temperature Diesel Combustion. *SAE Technical Paper* 2012-01-1721, 2012
105. Padala S, Woo C, Kook S, Hawkes ER. Ethanol utilisation in a diesel engine using dual-fuelling technology. *Fuel* 2013;109:597-607.
106. Kokjohn SL, Hanson RM, Splitter DA, Reitz RD. Fuel reactivity controlled compression ignition (RCCI): a pathway to controlled high-efficiency clean combustion. *Int J Engine Res* 2011;12:209–226.
107. Olofsson J, Seyfried H, Richter M, Aldén M et al. High-Speed LIF Imaging for Cycle-Resolved Formaldehyde Visualization in HCCI Combustion. *SAE Technical Paper* 2005-01-0641, 2005
108. Kim D, Ekoto I, Colban W, and Miles P. In-cylinder CO and UHC Imaging in a Light-Duty Diesel Engine during PPCI Low-Temperature Combustion. *SAE Int J Fuels Lubr* 2009;1:933-956, 2009
109. Chartier C, Aronsson U, Andersson Ö, Egnell R et al. Analysis of Smokeless Spray Combustion in a Heavy-Duty Diesel Engine by Combined Simultaneous Optical Diagnostics. *SAE Technical Paper* 2009-01-1353, 2009
110. Genzale C, Reitz R, and Musculus M. Optical Diagnostics and Multi-Dimensional Modeling of Spray Targeting Effects in Late-Injection Low-Temperature Diesel Combustion. *SAE Int J Engines* 2010;2:150-172
111. Aizawa T, Kosaka H, Investigation of the early soot formation process in a transient spray flame via spectral measurements of laser-induced emissions. *Int J Engine Res* 2006;7:93
112. Aizawa T, Kosaka H, Matsui Y, 2-D Imaging of Soot Formation Process in a Transient Spray Flame by Laser-induced Fluorescence and Incandescence Techniques. *SAE Technical Paper* 2002-01-2669, 2002
113. Herbinet O, Pitz WJ, Westbrook CK. Detailed chemical kinetic oxidation mechanism for a biodiesel surrogate. *Combust Flame* 2008;154:507-28
114. Glaude PA, Herbinet O, Bax S, Biet J, Warth V, Battin-Leclerc F, Modeling of the oxidation of methyl esters—Validation for methyl hexanoate, methyl heptanoate,

- and methyl decanoate in a jet-stirred reactor. *Combust Flame* 2010;157:2035-50, 2010
115. Sarathy SM, Thomson MJ, Pitz WJ, Lu T. An experimental and kinetic modeling study of methyl decanoate combustion. *P Combust Inst* 2011;33:399-405.
 116. Manin J, Skeen S, Pickett L, Kurtz E et al. Effects of Oxygenated Fuels on Combustion and Soot Formation/Oxidation Processes. *SAE Int. J. Fuels Lubr.* 2014;7:704-717
 117. Knothe G, “ “Designer” Biodiesel: Optimizing Fatty Ester Composition to Improve Fuel Properties”, *Energ Fuel* 2008; 22:1358–1364
 118. Yanowitz J, Ratcliff MA, McCormick RL, Taylor JD, Murphy MJ. Compendium of Experimental Cetane Numbers. NREL/TP-5400-61693, August 2014 , contract DE-AC36-08GO28308.
 119. Szybist JP, Boehman AL, Haworth DC, and Koga H. Premixed ignition behavior of alternative diesel fuel-relevant compounds in a motored engine experiment. *Combust.Flame* 2007;149:112-128.
 120. Zhang Y and Boehman AL. Autoignition of binary fuel blends of nheptane and C 7 esters in a motored engine. *Combust.Flame* 2012;159: 1619-1630
 121. Wang W and Oehlschlaeger MA. A shock tube study of methyl decanoate autoignition at elevated pressures. *Combust.Flame* 2012;159: 476-481
 122. BP Ultimate Diesel – Product Specification [Internet] [Cited 2015 July 21]. Available from: http://www.bp.com/content/dam/bp-country/en_au/products-services/fuels/ultimate-fuels/BP_Ultimate_Diesel.pdf
 123. Musculus MPB, Kattke K. Entrainment Waves in Diesel Jets. *SAE Int J Engines* 2009;2:1170-93.
 124. Kook S, Bae C, Miles P, Choi D et al. The Influence of charge dilution and injection timing on low-temperature diesel combustion and emissions. *SAE Technical Paper* 2005-01-3837, 2005